Nanoheterostructures based on nanosized Prussian blue and its Analogues: Design, properties and applications

Yannick Guari, Maëlle Cahu, Gautier Félix, Saad Sene, Jérôme Long, Joël Chopineau, Jean-Marie Devoisselle, Joulia Larionova

Nanoheterostructures Based on Nanosized Prussian Blue and its Analogues: Design, Properties and Applications

Yannick Guari,* Maëlle Cahu, Gautier Félix, Saad Sene, Jérôme Long, Joël Chopineau, Jean-Marie Devoisselle and Joulia Larionova*

ICGM, Univ. Montpellier, CNRS, ENSCM, Montpellier, France

E-mail: joulia.larionova@umontpellier.fr, yannick.guari@umontpellier.fr

Abstract

Nanoheterostructures combining Prussian blue (PB) or Prussian blue analogues (PBA) coordination polymers with other inorganic materials onto a single nanosystem are a highly challenging and rapidly emerging class of discrete hybrid multifunctional nano-objects, where chemical and physical properties can act separately or in synergy. They present various morphologies and chemical compositions, including diverse combinations of nanosized PB(A)s with metals, metal oxides, luminescent Ln^{3+}-based fluorides or Ln^{3+}-doped nanoparticles, semiconductors, silica, carbon nanotubes, metal-organic frameworks and others. Here, we present an overview focusing on relevant progresses achieved in this family of nanomaterials, giving an emphasis on their topology, physical and chemical properties as well as applications highlighting the role and contribution of the nano-sized PB(A)s.

Table des matières

Introduction

Inorganic nanoheterostructures combining two or more inorganic materials onto a single nanosystem, where different chemical compositions meet at the interface, constitute a sophisticated and highly challenging family of nanosized architectures, which has seen a great expansion during the last decades. This interest is motivated by the opportunity to combine several chemical and physical properties within the same nano-object acting separately or in synergy due to the mutual interaction between the constitutive components, building a powerful strategy towards the design of multifunctional nanomaterials. As a consequence, a large variety of studies addressing the challenge to get control over those phenomena were undertaken, offering a wide range of nanoheterostructures exhibiting different morphologies and associating various functionalities or improving the existent ones. The choice of the nanosized components to get combined into heterostructures generally depends on the targeted properties and the end applications. In this line of thought, we can cite probably the most investigated semiconductor@semiconductor[1-3] and metal@semiconductor nanosystems[4-6] with tuned optical properties, but also metal(oxide)@metal(oxide) nano-objects[7-10] with advanced catalytic, optical, magnetic and magneto-plasmonic functionalities, as well as multifunctional nanoscopic platforms designed by the association of metals, [11] semiconductors[12] or metal oxides[12] with nano-sized silica for a variety of applications in electronics, optics, catalysis and healthcare fields. Moreover, different morphologies ranging from the most common core@shell or core@satellites nano-objects of different geometries to complex multicomponent architectures have widely been designed and investigated.

Among those, nanoheterostructures, in which a nano-sized coordination polymer is combined at least with one other inorganic material, such as metal, metal oxide, semiconductor or silica, belong to a fascinating and recently emerging class of nanomaterials. The coordination polymer nanoparticles are made by transition metal or lanthanide ions connected through inorganic or organic ligands to give two- or three-dimensional networks where their growth is stopped by usual nanoscience tools, including the employment of stabilizing agents, ligands, matrixes and others. During two recent decades, the research has seen considerable advancements in the design of these fascinating nano-objects owing to a wide range of interesting properties promising for various applications. The most investigated families of those belong to metal-organic frameworks (MOFs) or Prussian blue (PB) and its analogues (PBA) nano-objects. The peculiarity of nanoheterostructures involving such materials as one of the components consists, first, in the opportunity to benefit from all the advantages of the coordination polymers, such as well determined and flexible molecule-based structures, adjustable composition, tunable physical and chemical properties, low density, porosity and relatively soft chemical ways for their synthesis through self-assembly reactions of molecular precursors. Secondly, their nanometric size gives access to unique size- and shape-dependent properties arising from the high surface-to-volume ratio, quantum size effects and electrodynamic interactions. Third, these nanoheterostructures present a complex interface, which often leads to the appearance of intricate interfacial phenomena, which highly influence the overall physical and chemical properties. In this overview, we will focus on a relatively recent but very rapidly developed family of nanoheterostructures involving PB(A)s as a nanosized constituent (Figure 1).

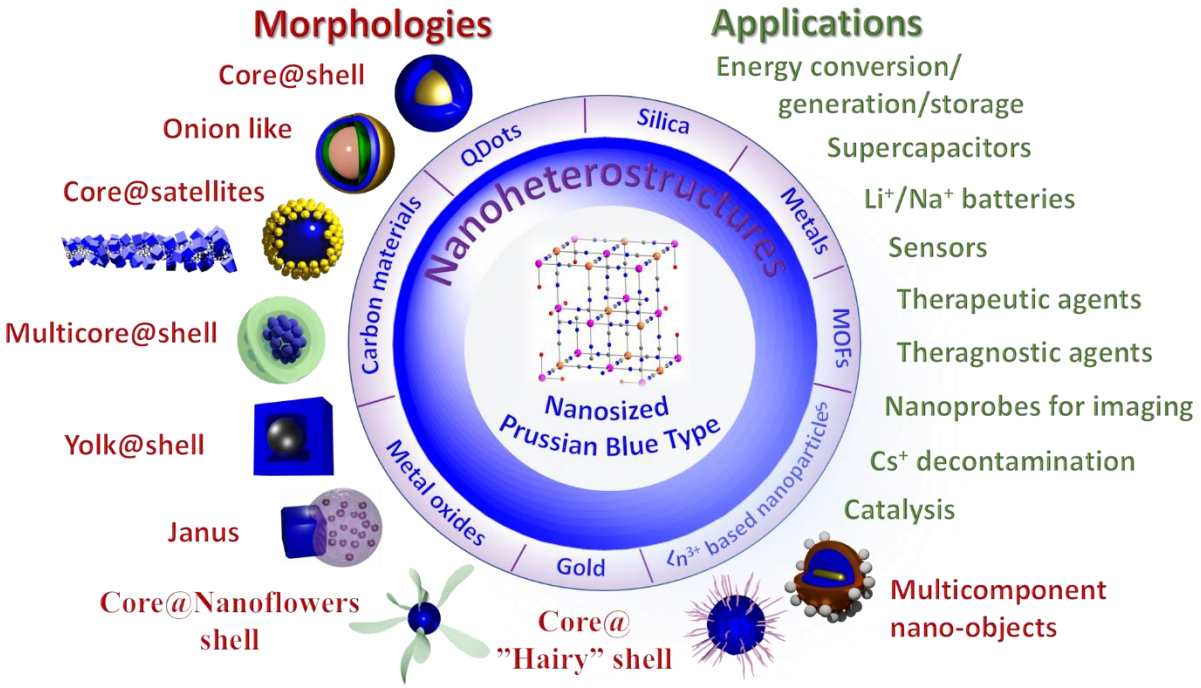

Figure 1. Diversity of morphology of nanoheterostructures presenting nano-sized PB(A)s as a component and their main applications.

Even if in the bulk state, PB was synthesized over three centuries ago and numerous analogues were discovered and investigated through the years, their history at the nanoscale starts only from the pioneering works of S. P. Moulik and coll. [13] and S. Mann and coll. [14] in 1999 and 2000, respectively. During the last two decades, impressive progress has been made to the advancement of these nanomaterials due to their fascinating size and morphology dependent magnetic, photo-magnetic, optic, host-guest, sorption, redox properties useful for a wide range of applications, including sensors, gas capture and storage, electrochromic devices, batteries, decontamination and healthcare. [15] The reason for the use of such materials as a component in nanoheterostructures is linked to motivating structural and morphological benefits consisting in: *(i)* an important chemical stability even at low pH; *(ii)* several types of porosities permitting to capture not only monovalent cations (such as Cs^+, Tl^+) in the tetrahedral sites but also small molecules and complexes; *(iii)* functionalizable surfaces thanks to the presence of non-saturated metal centers; (*iv*) a tunability of their chemical composition permitting the introduction of different transition metal ions or lanthanides by substitution or doping without structural changes. On the other hand, PB(A)s present multiple useful physical or chemical properties presented below, which can be combined with those of inorganic nanomaterials to achieve smart multifunctional nano-objects. Firstly, PB(A)s possess multiple redox properties presenting a great interest for many catalytic processes. Indeed, these materials have been proposed as a mimicking enzyme agent, a Fenton catalyst, oxygen evolution reactions (OER), and hydrogen evolution eeactions (HER) catalysts, and a support for metal catalysts. But also as a part of electrochemical, immune- or aptasensors for the detection of bacteria, species, molecules and biomolecules of interest. Secondly, PB(A)s exhibit an intrinsic porosity useful for insertion-disinsertion of monocations in Li^+ or Na^+ ions batteries or for decontamination of radioactive and/or toxic Cs^+ and Tl^+ ions. Further, they exhibit an important absorption in the

near infrared (NIR) region with a relatively high light-to-heat conversion coefficient and stability against irradiation, which makes these nanoparticles exceptional as a photothermal agent (PTA) for photothermal therapy (PTT) of cancer or bacteria killing. The nano and mesoporosities of PB(A)s permit the encapsulation and delivery of small drugs, which can also be assisted with the PTT action. Finally, PB(A)s with adjusted chemical composition can be employed as nanoprobes for magnetic resonance imaging (MRI), scintigraphy, photoacoustic, or computed tomography (CT) imaging. These multiple properties and advantages explain an important interest to the PB(A)s use as a component of original nanoheterostructures combined with other inorganic materials.

The first work on the design of such discrete nanoheterostructures reported in 2007 was devoted to the association of Au nanoparticles with PB with the aim to build a biosensor. [16] Starting from this date, the number of articles devoted to the elaboration of such intricate nano-objects is in constant expansion with an important acceleration in the last few years. During these fourteen years, metallic, metal oxides, metal sulfides, carbon nanomaterials and more recently silica, MOFs and polyoxometallates (POMs) nanomaterials were extensively combined with PB(A)s at the nanoscale. This review summarizes recent progress in this area of research and discusses the design, morphology, physical and chemical properties of these nanoheterostructures and their promising applications. We focus here only on discrete architectures obtained through a bottom-up approach mainly in colloidal suspensions through chemical ways. The nano-objects inserted into different matrixes[17, 18] or (electro)deposited on various surface[19, 20] are not discussed. The scope of this review is represented in Figure 1, and the organization includes the following sections.

Section I "Why Prussian blue and its analogues as a component in nanoheterostructures?" gives a brief presentation of PB(A) nano-objects, their structures, morphologies and the main properties in order to demonstrate the reasons for their use as a component in heterostructures. In this section, we particularly focus on the design of such nano-objects since similar synthetic methodologies are employed for their synthesis in nanoheterostructures. The advantages of PB(A)s linked with their multiple properties, including red-ox and photothermal activity, relaxivity, porosity, magnetic properties etc., useful in various applications are also described.

Section II is devoted to the main synthetic strategies in the design of the nanoheterostructures, the kaleidoscopic diversity of which is achievable thanks to the variation of the compositions, the morphology and the size of different components. In this section, we categorize the nanoheterostructures by the type of inorganic materials associated with the coordination polymers. Therefore, we outline successively the combination of these coordination polymers with *gold and other metals or metal alloys*, with *metal oxides and sulfides*, with *luminescent Ln^{3+}-based or Ln^{3+}-doped nanoparticles*, with other molecule-based materials, such as *MOF and POM*, and with non-metallic materials, such as *silica* and *carbon-based materials*. Each sub-section highlights the reason and advantages of such combination founding on the peculiarity and properties of each component, as well as on their compatibility. In each sub-section, the heterostructures are classified by their morphology following their increasing complexity, starting from simple core-shell nano-objects and finishing by advanced multicomponent architectures.

Section III describes the targeted association of the main physical and chemical properties of various components leading to an appearance of multifunctionality, which can be manifested

by the observation of properties acting separately or in synergy, and the key applications of these nanoheterostructures in various fields with strong societal demands, such as energy (conversion/storage/generation), health sensors for personal medicine, nanomedicine theragnosis, or sustainability (decontamination/catalysis). In the presented examples, we tried to emphasize the role of each component of heterostructure and the role of interfaces and related interfacial phenomena.

Finally, the *Summary and Outlook* section concludes the overall current status, challenges and proposes future perspectives in this fascinating domain.

I. Why Prussian blue and its analogues as a component in nanoheterostructures?

The famous bulk cyano-bridged coordination polymer, well known under the name Prussian blue, has been discovered in 1706 by J. C. Dippel and J. J. von Diesbach as a deep blue pigment. [21] While its crystal structure and fascinating chemical and physical properties have been investigated during 300 years after its invention, it and its analogues still remain an exciting and important object of modern research. [22] Indeed, several books and numerous reviews have been devoted to the description of structures, physical properties of PB and PBA and their applications. [23-31] PB presents a chemical formula $A_{1-x}Fe^{III}[Fe^{II}(CN)_6]_{1-x/4}\square_{x/4}\cdot nH_2O$ where n is the number of water molecules, A is a monovalent cation and $\square$ is a cyanometallate vacancy needed to assure the electroneutrality. In its crystal structure, the Fe^{2+} and Fe^{3+} ions are linked through cyano-bridges to form a porous three-dimensional face centred crystal structure (*fcc*). A variety of three-dimensional PBAs have been obtained and investigated by replacing both iron ions by transition metal ones where adjustements of the synthetic parameters give two extreme lacunary and not-lacunary structures, $M[M'(CN)_6]_{2/3}\square_{1/3}\cdot nH_2O$ or $AM[M'(CN)_6]\cdot nH_2O$, where M and M' are transition metal ions (Figure 2). Usually, PB and PBAs contain two types of water molecules: the coordinated to M^{n+} ions to complete the octahedral coordination sphere of these latter and the crystallized ones (lattice and zeolitic), which occupy the porosity of the networks. On the other hand, when a lanthanide ion comes to replace M ion, the structure becomes an orthorhombic one (Figure 3). As for the cubic PB(A)s networks, there are both, coordinated to Ln^{3+} and crystallized water molecules.

These coordination polymers present important mechanical robustness and excellent thermal and hydrothermal stabilities. As an example, the bulk PB compound has very high stability due to an extremely low dissociation constant ($K_d = 3\cdot10^{-41}$) in aqueous media and a solid-state thermal stability up to 200 °C in air, [32] while its cobalt analogues, $Cs_{0.74}Co[Co^{III}(CN)_6]_{0.91}\cdot5.2H_2O$, is stable up to 310 °C even in the presence of water vapours. [33] These compounds have widely been investigated for their exciting composition-dependent redox, optical, magnetic and host-guest properties. In this context, it is worse to underline that PB(A)s represent the most famous and the most investigated family of molecule-based magnets exhibiting a ferro- or ferrimagnetic long-range ordering greater than room temperature for some selected members of this family. The *fcc* network presents nano and mesoporosity (the last one comes from the presence of cyanometallate lacunas) whereas empty tetrahedral sites are able to host monovalent inorganic cations, such as, for instance, alkali metal or thallium ions. For these reasons, bulk PB(A)s have deeply been investigated and proposed for various applications

as pigments, materials for Na^+ and Li^+ ions' batteries, molecular sieves, materials for hydrogen storage or as decontaminant materials for radioactive Cs^+ and non-radioactive Tl^+. It is interesting to note that the bulk PB compound has been approved by the US Food and Drug Administration (FDA) agency for its use as an exclusive antidote for human beings in the case of Cs^+ and Tl^+ poisoning and is widely used under its trade name Radiogardase®. [34] As an example, the daily dose for an adult in the case of radioactive Cs^+ contamination constitutes *ca.* 10 g, illustrating the low toxicity of PB and its biocompatibility.

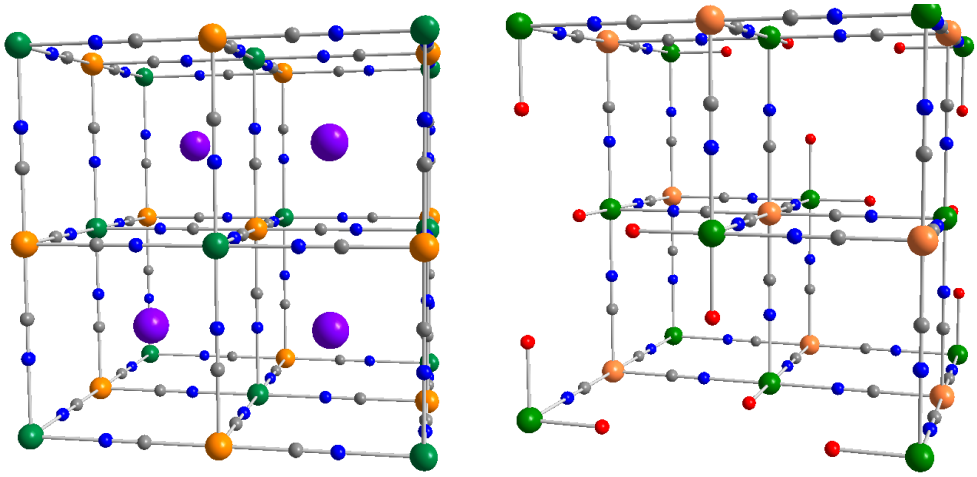

Figure 2. Crystalline structure of PBAs in their : (a) non-lacunary $AM[M'(CN)_6]\cdot nH_2O$ (1:1:1 type), and (b) lacunary $M[M'(CN)_6]_{2/3}\square_{1/3}\cdot nH_2O$ forms. Colour code: orange, M'; green, M; violet, A; blue, N; grey, C. The oxygen of H_2O coordinated to M^{n+} are represented by red spheres.

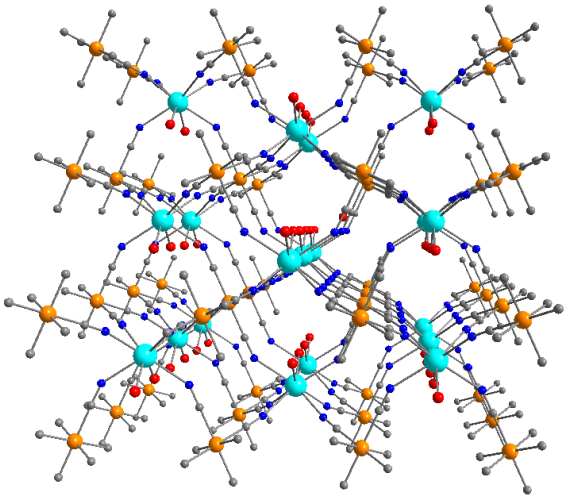

Figure 3. Crystalline structure of $Gd(H_2O)_4[Fe(CN)_6]\cdot 4H_2O$. Color code: orange, Fe; blue cyan, Gd; blue, N; grey, C. The oxygen of H_2O coordinated to Gd^{3+} are represented by red spheres.

Considering that the inorganic nanoparticles have been known and investigated for decades, it is somewhat surprising that the development of nanosized PB(A)s started relatively recently. Two pioneering works on the PB(A)s nano-objects have been reported by S. P. Moulik and coll. in 1999 [13] and S. Mann and coll. in 2000[14], both devoted to the use of reverse micellar

systems for the synthesis and stabilization of cubic nanoparticles of CuFe-PBA and PB itself, respectively. Such protocol was extended to the synthesis of CoFe-, CrCr-PBAs,[35] and NiCr-,[36] FeCr-[37] or CoCo-PBAs [38] demonstrating that [H_2O]/[AOT] ratio (with AOT = bis-(2-ethylhexyl)sulfosuccinate) tensioactive agent), the nature and the concentration of precursors permit controlling the size and shape of the obtained nanoparticles. Starting with these seminal works, the synthesis and investigation of nano-sized PB(A) systems have attracted a great deal of attention from numerous research teams worldwide. Various synthetic approaches consisting in a classical co-precipitation of two precursors or single-source method, hydrothermal reaction, sono-, electro-, photochemical ways, and others have been explored. They give an acess to the multitude of PB(A)s nano-objects with different chemical compositions, available in a wide range of sizes, from a few to several tens of nanometers, having different morphologies and controlled surface state. The synthesis parameters, which make possible to control the elaboration of these nanoarchitectures have been the subject of very comprehensive reviews and book chapters to which readers can refer. [39-47]

However, as many of the used synthetic protocols for the synthesis of nano-sized PB(A)s have been adapted to the elaboration of nanoheterostructures involving PB(A)s as one of the components, we give a brief outline of the frequently used synthetic methodologies. Three main approaches have been employed for this purpose: (*i*) the self-assembly reaction between appropriated precursors in organic solvents or in water leading to the synthesis of small nanoparticles with the size lower than 20 nm, (*ii*) the controlled kinetic growth of the cyano-bridged network in water in very diluted aqeous solutions without stabilizers followed (or not) by the post-synthetic anchoring of the latter on the nanoparticles surface, and (*iii*) hydrothermal synthesis.

First, the self assembly reaction between appropriated hexacyanoferrates/ferrites and metal salts precursors in water without any stabilizing agents has been employed to synthesize PB(A)s nanoparticles with the size lower than 20 nm. [48] In this way, nanoparticles of PB (13 nm), $Ni^{II}Fe^{III}$ (14 nm) and $Co^{II}Fe^{III}$ (18 nm) were obtained, the size of which depends on the type of the metal ion used. These nanoparticles can then be redispersed in toluene with the addition of oleylamine as a stabilizing agent to obtain stable colloidal solutions. Note however that in the most of cases, the synthesis of small well disperced PB(A) nanoparticles has been performed by introducing different stabilizers (small molecules with donor atoms assuring their coordination to the nanoparticles surface, molecules, biomolecules and polymers assuring the electrostatic or steric stabilization) during the self-assembly reaction. In this way, the stabilizing agents not only help to assure the good colloidal stability of the nanoparticles, but can also control the size through the ratio precursors/stabilizer. The self-assembly approach in the presence of various stabilizing agents could be performed either in organic solvents including ionic liquids or water, usually providing tiny nanoparticles with sizes less than 10 nm, while they are somewhat larger in water. Only one example in literature dealt with the synthesis of PB(A)s nanoparticles in a conventional organic solvent. It concerns the synthesis occurring in THF in the presence of oleic acid and trioctylamine as stabilizing agents to afford ultra-small nanoparticles of different composition $Ni^{II}Fe^{III}$-, $Mn^{II}Cr^{III}$-, $Ni^{II}Cr^{III}$- and $Ln^{III}Cr^{III}$- PBAs (with Ln = Eu, Tb or Sm). [47] Several examples concerned the use of ionic liquids, such as 1-R-3-methylimidazolium tetrafluoroborate [RMIM][BF_4], which act as both, a stabilizing agent and a solvent. By varying the length of the N-alkyl chain on the imidazolium cation $[RMIM]^+$ (R=1-

butyl (BMIM), 1-decyl (DMIM)), the growing process can be controlled to produce $Ni^{II}Fe^{III}$-, $Cu^{II}Fe^{III}$- and $Co^{II}Fe^{III}$-PBAs nanoparticles of 2-3 nm.[49] A specific study of the $Cu_3[Fe(CN)_6]_2$/[C_n-MIM][An] (where n = 2, 4 and An = Cl, BF_4) system was performed to evaluate the influence of added small amounts of water, counter anion influence and microwave or temperature effects on the size, shape and aggregation of the as-obtained nanoparticles. [50] Moreover, using a room temperature ionic liquid crystal, [C_{12}-MIM][BF_4], allows obtaining a long-range organization of $Mn_3[Cr(CN)_6]_2$ at the nanoscale level within the liquid crystal phase. [51] An additional stabilizing agent, such as N,N-dimethyl formamide was also added to the synthesis of nano-sized $Co^{II}Fe^{III}$-PBA using the room temperature ionic liquid, tetramethylammonium tetrafluoroborate, as the reaction media for further uses in the catalytic epoxidation of styrene. [52]

However, the most employed media to perform the synthesis of PB(A)s nanoparticles is water, and many studies were devoted to this purpose. The first example to cite concerns the synthesis of PB in the aqueous solution in the presence of polyvinylpyrrolidone (PVP) from $FeCl_2{\cdot}4H_2O$ and $K_3[Fe(CN)_6]$ precursors giving the PB nanoparticles with sizes ranging from 16 to 27 nm, which can be controlled by the ratio PVP/Fe^{2+}. [53] It is noteworthy that the obtained nanoparticles with the ratio PVP/Fe^{2+} = 100 could be completely redispersed in other solvents, such as methanol, ethanol, acetonitrile, DMF, DMSO, or dichloromethane. This strategy was also generalized for several PBAs, such as $Rb_{1.8}Co_4[Fe(CN)_6]_{3.2}{\cdot}nH_2O$, [54] CsNi[$Cr(CN)_6$], [55] $Mn_3[Fe(CN)_6]{\cdot}12H_2O$, [56] $Ag_3[Fe(CN)_6]$, [57] and CuNi[$Mo(CN)_8$]. [58] Further, other polymer-based stabilizing agents, such as poly-(diallyldimethylammonium chloride)[59] or polyethylene glycol (PEG) with different molecular weights and functionalities,[60] were also considered for the synthesis of nano-sized PB(A)s and lanthanide-based (including Gd^{3+}) analogues. An alternative strategy to obtain PEG-stabilized $K_{0.94}Gd_{0.02}Fe[Fe(CN)_6]$ consisted first in the synthesis of these nanoparticles in the presence of PVP followed by its further replacement by PEG (MW = 12000-14000) during a dialysis procedure. [61] Note that the PEG-stabilization of PB(A)s nanoparticles is a strategy of interest when considering various biomedical applications. Moreover, other biocompatible stabilizing agents, such as N-acetyl-D-glucosamine[60] or bovine serum albumin (BSA), were also used. [62] Finally, the employment of citrate as a biocompatible stabilizing agent also permitting further post-functionalization have widely been employed. Indeed, the synthesis of PB and NiFe-, NiCr, NiCo- and CoFe-PBAs with sizes ranging from 13 to 110 nm in the presence of citrate or citric acid were reported. [63] [64], [65], [66], [67], [68]

The second synthetic approach largely used to obtain PB(A)s nanoparticles consists in the controlled self-assembly reaction of appropriate precursors in diluted aqueous solutions without stabilizing agents. The colloidal stability is provided here by repulsive electrostatic interactions of the negatively charged nanoparticles' surfaces. This methodology allows thus to obtain surfactant-free nanoparticles of different PB(A)s with a wide size range (30 – 200 nm), which can easily be post-functionalized in the second step. The size control in these systems may be achieved by modulation of the addition rate, precursors' concentration ad the presence of monovalent ionic salts. NiFe-[69] and CuFe-PBAs[70] nanoparticles with sizes ranging from 12 to 80 nm were elaborated following such procedure. An interesting study was performed by using this protocol for a series of PB(A)s with rubidium as a counter cation in the PBA structures, such as CoCr-, CoFe-, CoCo-, NiCr-, NiCo-, NiCo-PBAs and PB itself with different

sizes (100-500 nm). The study found that the growing mechanisms differ among this closely related family of compounds. On the one hand, *ex situ* transmission electron microscopy (TEM) and *in situ* ionic conductivity and Dynamic Light Scattering (DLS) analyses indicated that the Cu^{2+} and Ni^{2+} analogues grew by a traditional heterogeneous precipitation process, whereby nucleated particles formed by the addition of ions from solution. On the other hand, the Co^{2+} analogues and the parent rubidium PB grew by the aggregation of precursor particles followed by annealing into crystalline mesoscale particles. [71]

The third hydrothermal approach, affords nanoparticles having the size ranging from tens of nanometers to several micrometres. Most of the time, it uses PVP as a stabilizing agent under acidic pH and a single $[Fe(CN)_6]^{3-}$ precursor for the synthesis of PB[72], [73] or two precursors, Zn^{2+} salt and $[Fe(CN)_6]^{3-}$ for $Zn^{II}Fe^{III}$-PBA.[74] Moreover, glucose [75] or PEG-400 [76] have been used as an alternative to PVP. Such hydrothermal synthesis has also been employed to obtain hollow PB nanoparticles by a two-step process: first, the synthesis of PB nanoparticles has been performed by using PVP under hydrothermal conditions and then a second hydrothermal treatment using PVP under harsher acidic conditions inducing the etching of the PB nanoparticles leading to hollow shapes. [77]

The amazing prospects offered by PB(A)s nano-objects in comparison to other inorganic nano-sized systems consists in the fact that they present a variety of useful properties depending not only on the diversity of compositions and structures, but also on the size, morphology and surface state. Indeed, they exhibit unique magnetic, optic, host-guest, redox and sorption properties, making them very interesting for potential technological applications, including biology and medicine, gas capture, gas storage, batteries, catalysis, sensors, electrochromic devices, decontamination (Figure 4). Among those, we briefly present in this section only the properties and related applications of PB(A)s, which have been promoted for designing nanoheterostructures.

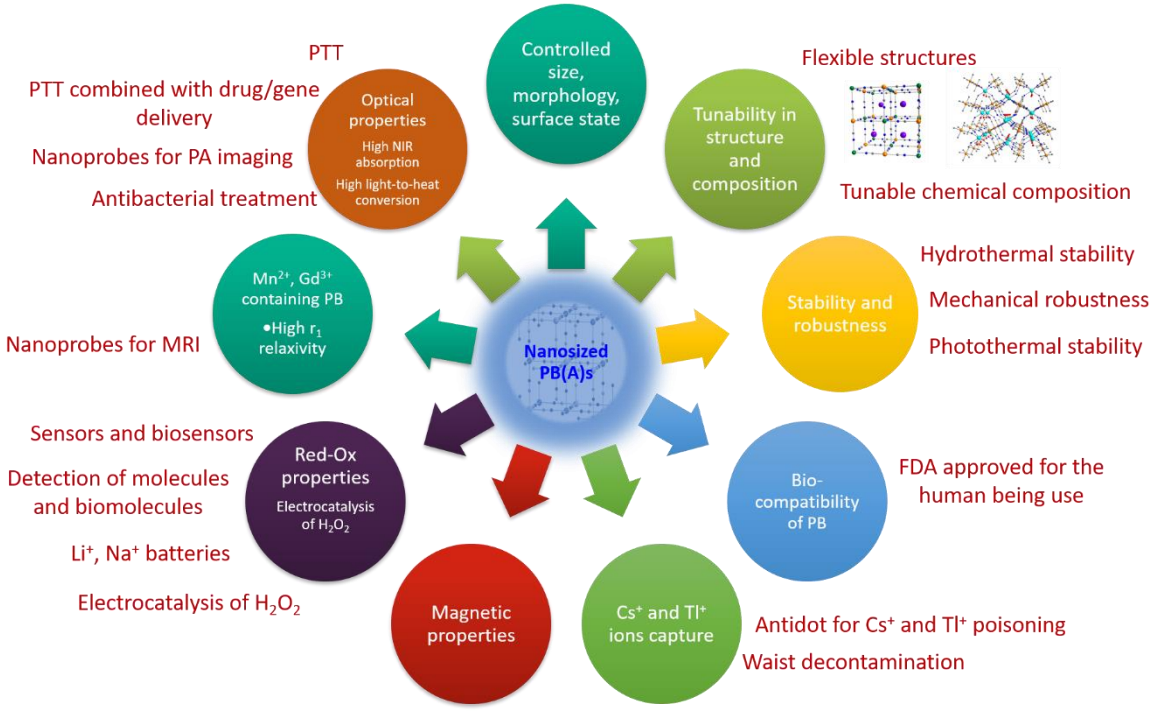

Figure 4. Advantages of PB(A)s as a component in designing nanoheterostructures.

The exceptional stability, low toxicity, optical, magnetic and redox properties of the PB nanoparticles, as well as their tunability permitting the properties' adjustment through the modulation of the nanoparticles' composition explain the growing interest for their design and investigation in relation to biomedical applications. Several reviews have been devoted to the PB type nano-objects as new promising nanoprobes or therapeutic agents for nanomedicine. [78], [79], [80], [81] Probably the first place in the number of published articles on this subject is devoted to investigating and promoting of the optical properties of the nano-sized PB, and more precisely, their photothermal activity, which makes them very promising as PTA. PTT is a newly developed hyperthermia strategy for the therapeutic treatment of tumour cells, which employs NIR photoabsorbers or PTA to generate heat upon NIR laser irradiation. Its principle consists in malignant cells "burning" by laser irradiation at low energy wavelengths in the presence of NIR PTA. Among others, this treatment offers attractive advantages over conventional therapeutic methods, such as high specificity, precise spatial-temporal selectivity, and minimal invasiveness. [82], [83], [84] Up to date, various Au nano-objects, including gold nanorods, nano-shells, nanostars, as well as carbon nanotubes, graphene oxide nanoparticles or upconversion nanocrystals have been found very promising for this purpose. [85] PB nanoparticles appear as a new promising alternative because they exhibit strong absorption in the NIR (I window) with a high molar extinction coefficient due to the Fe^{2+}-to-Fe^{3+} intervalence charge transfer band situated between 650 and 850 nm and high light-to-heat conversion efficiency. [86], [87], [88] It has been demonstrated that PB nano-objects in aqueous solutions present higher photothermal conversion efficiency than Au nanorods and better photothermal stability than Au nano-objects and organic dyes used as conventional PTA. Indeed, numerous PB nanoparticles with different sizes and morphologies have been investigated as PTA *in vitro* and *in vivo*. [40], [86], [89], [90], [91], [92], [93] Moreover, the PTT action may be combined with drug or gene delivery to enhance the therapeutic efficiency through complementary or synergic effects between the PTT and chemotherapy. In this line, several works report on the design of PB nanoparticles loaded by conventional anticancer drugs, such as doxorubicin (DOX), [88], [94], [95], [96] or 10-hydroxycamptothecin, [97] or nano-objects conjugated with pDNA, [98] or with antigen specific cytotoxic lymphocytes. [95]

The high absorption efficiency in the NIR window and the high photothermal stability have also been promoted by making these nanoparticles as a new kind of contrast agents (CAs) for NIR light-mediated photoacoustic tomography. Photoacoustic (PA) imaging is a widely used non-invasive imaging modality with a reasonable penetration depth, which presents a good soft-tissue contrast and an excellent high sensitivity. It can be used to image deeper tissues than other optical imaging modalities (*e.g.* confocal microscopy and optical coherence tomography) with high resolution. In comparison with various nanoscaled NIR absorbers, such as gold nanostructures, carbon nanotubes, copper sulfide nanoparticles, PB nanoparticles have been found biodegradable, less toxic, less expensive and more performant for deep tissue imaging. [99]

Concerning the magnetic properties of PB(A)s, Gd^{3+} and Mn^{2+}-doped PB nano-objects presenting high longitudinal relaxivity have been developed as CAs for MRI. MRI is a powerful non-invasive imaging technique widely used in clinical practices to visualize internal body structures. MRI CAs are currently used in order to improve the image quality by locally increasing the nuclear relaxation rates. [100] Their efficiency is evaluated on the basis of their

ability to influence the longitudinal, r_1, and transverse, r_2, relaxivities. The positive CAs, also called T_1-relaxing, provide a brilliant spot on the MR image in the organ or tissues where they are delivered. Paramagnetic Gd^{3+} (S = 7/2) -based compounds containing chelating or macrocycle ligands are the currently used commercial positive CAs. For instance, commercial positive CA based on gadolinium chelate complexes known under its trade name ProHance® presents r_1 value of about 3.5 $mM^{-1}s^{-1}$ at 1.5 T and at 298 K. [101], [102] In this line of thought, PB nano-objects present only modest longitudinal relaxivity values (for instance 0.079 $mM^{-1}s^{-1}$ at 11.7 T [64] and 0.2 $mM^{-1}s^{-1}$ at 1.5 T [65]), but when high spin paramagnetic Mn^{2+} (S = 5/2) or Gd^{3+} (S = 7/2) ions are introduced in the PB network, the longitudinal relaxivity increases making them, therefore, promising as CAs for MRI and competitive with the actually existing ones. These paramagnetic ions may be either introduced in the tetrahedral sites or may substitute iron ions of the PB framework. In the latter case, the total Fe^{3+} ions substitution conducts to the formation of orthorhombic coordination networks (see Figure 3 for the $Gd(H_2O)_4[Fe(CN)_6]\cdot 4H_2O$ structure). Indeed, several Mn^{2+} and Gd^{3+}-doped PB nano-objects of different structure, composition, size, shape (nanoparticles, nanocubes, hollow cubes) and coating with highly improved longitudinal relaxivity in comparison with the values observed for commercial CAs and with high contrast in T_1-weighted *in-vivo* MRI images have been reported. [103], [104], [105], [106] Such performance have been explained by the presence of: (*i*) coordinated to Gd^{3+} or Mn^{2+} water molecules, (*ii*) a relatively important number of these paramagnetic ions per nanoparticle, (*iii*) efficient exchange between coordinated, crystallized and solvent water molecules, (*v*) an optimal size and surface state of these nanoparticles permitting high water accessibility and an optimal slow molecular rotation.

In the case of radioactive Cs^+ contamination or Tl^+ poisoning, recent developments in pharmacokinetics and nanomedicine have demonstrated that the use of nano-scaled PB(A)s improves the kinetic and efficacy of the decontamination with respect to the corresponding bulk materials. In this connection, several types of nanocomposites involving PB nanoparticles included in silica or carbon sponge matrixes have been proposed as an efficient absorbent for the decontamination of Cs^+ and Tl^+ ions in the gastrointestinal tract of rats. [78], [107], [108], [109] Another system based on the ultra-small PB nanoparticles stabilised by the Aonys® oil acts as an *in vivo* Cs^+ uptake agent and presents an higher efficiency with a significant dose-effect and different elimination ways than commercially available PB (Radiogardase®). [110]

Besides optical, host-guest and relaxivity properties exploited for biomedical applications, nano-sized PB(A)s have also been investigated for their size-dependent magnetic properties. It should be noted that some of these coordination polymers in their bulk state presented exceptional magnetic behaviour showing the presence of a long-range magnetic ordering at particularly high critical temperatures for molecular materials. As an example, some bulk $V^{II}Cr^{III}$ PBAs exhibited ferrimagnetic behaviour with critical temperatures up to 400 K. [111], [112], [113] The exchange interactions between the spin carriers conducting to the appearance of ferro- or ferrimagnetic behaviours have been explained by using the model of J. Goodenough adapted for molecular materials by O. Kahn involving the magnetic orbitals overlap. [114], [115] The sign of magnetic interactions and the value of the critical temperatures depend on the spins and anisotropy of the metal ions. As for other magnetic nanoparticles, the decrease in the dimensionality of PB(A)s to nano-sized level prevents the propagation of the magnetic correlation to infinite, and as a consequence, the appearance of important size effects is

expected, the most important being the appearance of a superparamagnetic behaviour instead of ferro- or ferrimagnetic ones. On the other hand, numerous factors can impact the magnetic regime of these nanoparticles, including the presence of dipolar (magnetostatic) interactions between the nanoparticles combined or not with a surface or volume spin disorder. The magnetic properties of nanosized PB(A)s of different chemical compositions, sizes, state surfaces in colloidal suspensions or embedded into inorganic or organic matrixes have been investigated. Four relaxation regimes have been identified in the nano-sized PB(A)s according to the above-mentioned parameters: [47], [46] (*i*) ferro- or ferrimagnetic behaviours of multidomain nanoparticles presenting size larger than the critical radius, (*ii*) the superparamagnetic regime of isolated monodomain nanoparticles, (*iii*) the spin-glass like regime arising from strong dipolar interparticle interactions, and (*iv*) the spin-glass like regime arising from dominant intraparticle surface spin disorder.

Finally, the exclusive redox properties of PB(A)s have found an important development in several applications. PB(A)s, in many cases, do act as three-dimensional electrocatalysts, chemically stable and electroactive. [116] The reduction and oxidation reactions for the non-lacunary form (also called "soluble" form) of PB are expressed in Scheme 1.

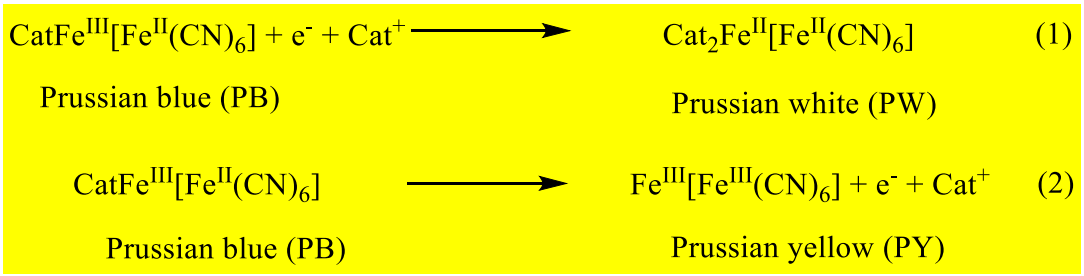

Scheme 1. Redox processes for the non-lacunary form of PB.

Similar redox reactions have also been proposed for the lacunary form of PB (also called "insoluble" form) (Scheme 2)

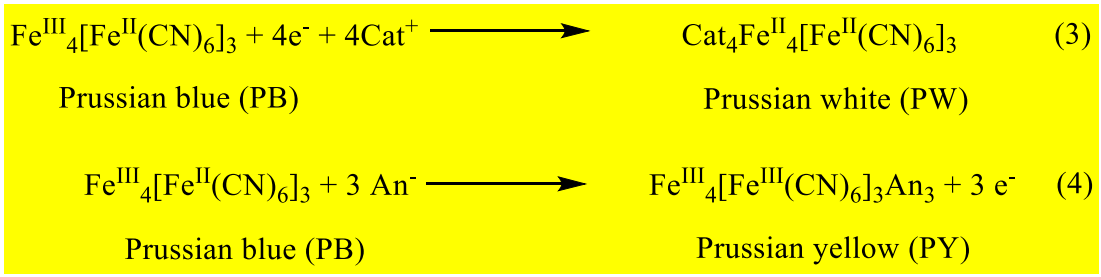

Scheme 2. Redox processes for the lacunary form of PB.

The PB reduction leading to Prussian white (PW) implies the incorporation of cations (Cat^+), whatever the PB forms involved (Equations (1) & (3)), while the oxidation implies the loss of cations for the non-lacunary form (Equation 2) or the incorporation of electrolyte anions (An^-) for the lacunary form (4) leading to Prussian yellow (PY). [24, 117] Thus, oxidation and reduction reactions of the iron ions proceed through a flux of cations/anions to pass through the channels and holes of the network, providing the necessary charge compensation. The electrochemical processes in which PB is involved result in substantial changes of optical properties with four-colour electrochromocity. As previously mentioned, the deep blue colour

of PB itself is explained by an intense intervalence charge-transfer absorption band in the NIR window with a transition from the ground to the excited state on which an electron is transferred from $Fe^{III}Fe^{II}$ to $Fe^{II}Fe^{III}$. The fully oxidized form of PB, PY is visually yellow-brown, and the fully reduced PW form is colourless, while the fourth colour relates to Berlin green (BG), which, in reality, is an intermediate form between PB and PY. This behaviour may also be generalised for other PBAs, where both transition metal ions may be involved in the redox process, as shown in Scheme 3. The dependence between the hydration of the cations (usually alkali ions) and their insertion capacity within the PB(A) networks and then the impact on the electrochemical properties has been demonstrated by F. Scholtz and A. Doménech-Carbo. [118] The electrochemical properties of the PB(A) deposited on the different electrodes as particules or films with different cations has been investigated by cyclic voltammetry. It has been demonstrated that PB(A) can reversibly intercalate Li^+, Na^+, K^+ or NH_4^+ at high rates. [119] For instance, cyclic voltammograms of the electrodeposition of PB on an electrode shows two sets of sharp peaks corresponding to three forms of varied valence state (PW, PB and BG). [120] Note that the redox transformation process of PB(A) is usually accompanied by a color change (electrochromicity), which is currently used in electrochromic devices since a rich palette of colours depending on the transition metal ions and the respective redox form involved.

$$Cat_zMe^{II}y[Fe^{II}(CN)_6]_2 \longrightarrow Cat_{z-y}M^{III}y[Fe^{II}(CN)_6]_2^{+} + ye^{-} + yCat^{+} \quad (5)$$

$$Cat_zMe^{III}y[Fe^{II}(CN)_6]_2 \longrightarrow Me^{III}y[Fe^{III}(CN)_6]_2 + 2e^{-} + zCat^{+} \quad (6)$$

Scheme 3. Red-ox processes for PB(A)s.

Such amazing redox properties opened the door to a wide range of applications in energy, mainly in batteries and supercapacitors, but also in electrocatalysis, in the fields of sensors, biosensors and detection. The reader can refer to various reviews providing an in-depth overview of the state of the art in these attractive areas. [116], [119], [121], [122], [123] As an example, PB(A)s have been found promising as electrode materials, especially for Na^+, but also for other ions (Li^+, K^+, Mg^{2+}, Ca^{2+} and other multivalent ions) batteries because of their open channel network, compositional and electrochemical tunability and low cost. [124], [125], [126], [127] In particular, a large number of PB(A) materials have been developed with considerable success as an appealing cathode material for sodium ion batteries. Remarkably, the structural robustness of the cyano-bridged frameworks upon intercalation/deintercalation constitutes an asset. Thus, an important effort has been done in the understanding of structure/synthesis/performance relationship for these materials in the search of high reversible capacities and long cycle life. In this line of thought, several works demonstrated that the fine control of the synthesis in order to suppress the lattice defects and interstitial water molecules is a key parameter to achieve a high Na^+ insertion performance and important cycling stability. Considering several parameters, including material cost, environmental friendliness and electrochemical performance, it appeared that the most promising candidates for practically viable sodium ion batteries for large-scale stationary applications are Mn- and Fe-based PBAs, such as MnMn-, FeFe-, and MnFe-PBA. Moreover, PB(A)s can also be interesting for aqueous Na^+ ion batteries applications, but for the moment, an important improvement of the

electrochemical Na^+ insertion performance and capacities is highly needed to be competitive with the commercially viable batteries.

Considering another facet of the redox properties, PB(A)s are well known for their capacity to electrocatalyst oxidation (7) and reduction (8) of H_2O_2 following reactions depicted on Scheme 4.

$$H_2O_2\ (aq) \longrightarrow O_2\ (g) + 2e^- + 2H^+\ (aq) \quad (7)$$

$$H_2O_2(aq) + 2e^- + 2H^+(aq) \longrightarrow 2H_2O(l) \quad (8)$$

Scheme 4. Oxidation and reduction of H_2O_2.

Complex chemistry stays behind the transformation of hydrogen peroxide by PB(A)s and the involved mechanisms are not yet clearly identified. These properties are particularly relevant because a large number of enzymes produce H_2O_2 as a by-product, which can be detected by PB(A)s. In particularly, PB can mimic three antioxidant enzymes: peroxidase, catalase, and superoxide dismutase (see Figure 5). [128] An important number of sensors and biosensors based on this PB(A)s activity has been reported, including the detection of glucose, [129] glutathione, [130] dopamine, [131] hydrazine, [132] nitrites, [133] and sulfites. [134]

Finally, the redox properties of PB(A)s were also used for electrocatalysis aiming to detect pollutant compounds dangerous for the environment and human health, such as hydrazine, [135], [136] explosives, [137], [138] nitrites and sulfites, [133], [139], [140] as well as numerous drugs. [141], [142], [143], [144]

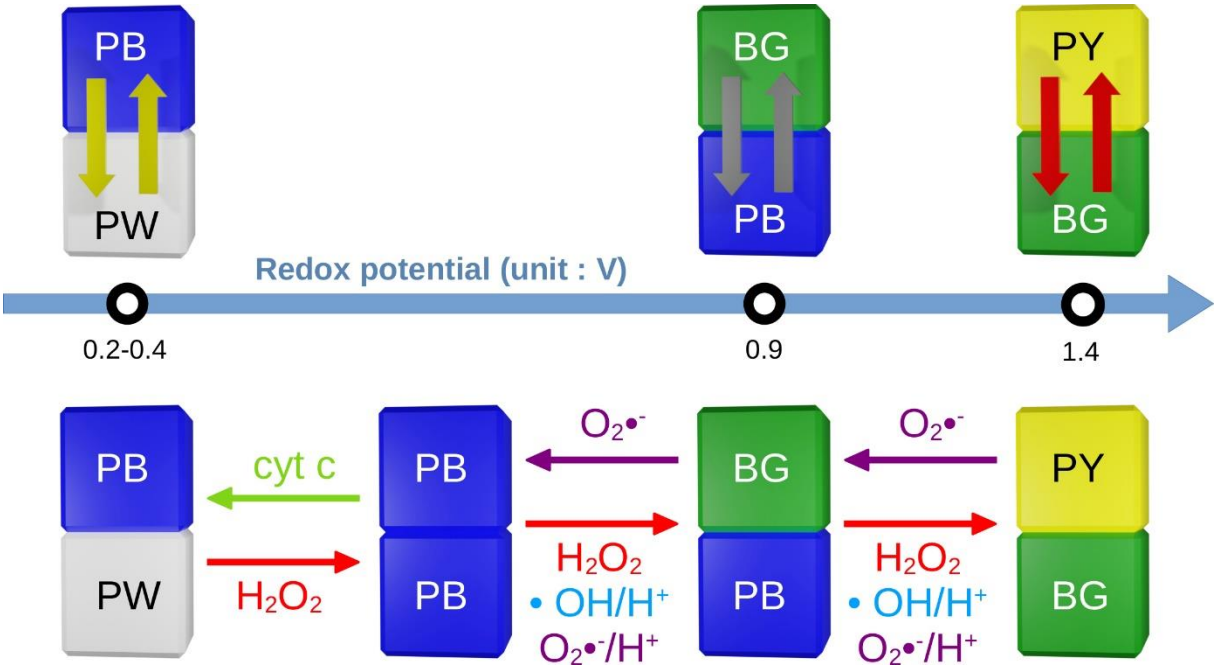

Figure 5. Schematic mechanism of the multienzyme-like activity of PB nanoparticles based on standard redox potentials of different compounds in the reaction systems. Depending on the oxidation states of iron ions, different redox transformations of PB have been identified: reduced form $Fe^{II}Fe^{II}$ called Prussian white (PW), oxidized form $Fe^{III}Fe^{III}$ known as Prussian yellow (PY) and a partially oxidized form identified as Berlin green (BG).

PB(A)s can be further beneficial and interesting in connection to their redox properties at the nanoscale for all above-mentioned applications and a huge amount of work has been performed

in this area. The reader may refer to appropriate reviews covering this field of research. [145-148] Thus, for all the above-mentionned reasons, PB(A)s have widely been considered as a component in association with another material at the nanoscale to afford nanoheterostructures presenting multifunctional properties of interest in various application fields that constitute the aim of this review.

II. Design and typology of nanoheterostructures involving nanosized PB(A)s as a component

Nanoheterostructures involving PB(A)s as a component have been designed in various morphologies. However, the majority of them are directly related to the core@shell shape, which includes nano-objects of several types: simple core@shell, onion-like core@multishells, core@satellites and multicore@shell geometries. In core@shell or multishell systems, an inner core is surrounded by a shell composed of one or more layers of other materials, which interact with the external environment. The components of such systems share large bonding interfaces, where strong electronic communication may be established. This conducts to distinct physico-chemical properties or even synergic effects in comparison to those of the individual components. Note that in classical inorganic core@shell nanoparticles, the shell is usually epitaxially grown on the surface of the core materials, which requires a closeness of their crystal structures with an important matching of their lattice parameters (usually within 1-3%). This permits the minimization of misfit strain and avoids the generation of defects until the shell thickness is kept small enough.[149] In this line of thought, an important effort has been achieved in the design of PB(A)s@PB(A)s core@shell nanoparticles and numerous examples of nano-objects of this type with different sizes and compositions of the core and the shell have been reported. [149], [150], [151], [152], [153], [154], [155], [156], [157], [158], [159], [160], [161], [162], [163] However, in certain conditions, the requirements of the lattice compatibility between the core and the shell can be less strict. For example, pathways for plastic strain relaxation may be available when the secondary material deposition proceeds non-epitaxially, developing a polycrystalline or even partially amorphous shell. Misfit strain constraints could be bypassed under particular conditions leading to fast incorporation of a large density of crystal defects at some reaction stages. [164] In such cases, small-extension coherent heterojunctions can appear on the core/shell interface at which dissimilar crystallographic relationships locally hold between the relevant lattices. This situation may be considered as the most relevant in nanoheterostructures, where core and shell materials present different crystalline parameters or important mismatch lattices differences, such as for instance in well definite gold core@PB(A)s nanoheterostructures. [164], [165], [166], [167], [168], [169] A core@satellites topology can be considered as an extreme situation, which corresponds to a partial coverage of the surface core resulting from an important difference between the crystallographic parameters of different components or arising from the employment of specific synthetic conditions. Such morphology is mainly represented by PB(A)s core @metal (oxide) satellites nano-objects. Among those, several examples of core@satellite, core@“hairy” shell or core@nanoflowers shell or even Janus morphology were also obtained with PB(A)s as one of the components of the nanoheterostructure. Obviously, the type of the shell (continuous shell or satellite

configuration), as well as the type of a connecting interface, may have a profound impact on the ultimate chemical-physical properties of the heterostructures.
Apart from the classical core@shell or core@satellites morphology, a multicore@shell-like system, which can be viewed as several nano-cores embedded in another material, is also represented in these nanoheterostructures. The typical example represents metal oxide core@PB(A)s nanoheterostructures. Moreover, other discrete nanoheterostructures combining PB(A)s with other inorganic nanomaterials were obtained, such as a necklace or yolk-shell shape or event more complex structures, where several inorganic components are associated with PB(A)s. Figure 1 schematically summarizes various discrete nanoheterostructures combining PB(A)s with one or more inorganic nanomaterials. In the following sections, we describe the design and morphologies of different containing nanoheterostructures, categorizing them by the type of inorganic materials combined with PB(A)s.

II.1. Gold and other metals@PB(A)s nanoheterostructures

The association of nano-sized PB or PBAs with noble metals (such as Au, Ag, Pt and Pd) in nanoheterostructures is one of the largest investigated families among other nanosized architectures built with cyano-bridged coordination polymers. The gold@PB system is the most frequently described in literature, and the morphologies, properties and applications are the most diversified. This is certainly due to the exceptional physico-chemical properties of nano-sized gold, which are complementary with those of PB(A)s. In this context, numerous examples of Au@PB(A)s nanoheterostructures were designed, particularly as a theragnostic nanoplatform for biomedical applications, where different types of imaging approaches were associated with multimodal therapy. These nanoheterostructures were also proposed as biosensors for the detection of different peptides, aptamers, biomolecules and tissues. On the other hand, several examples of the association of PB with nanosized Au, Ag, Pt and Pd exhibiting enhanced catalytic activity were also reported.
Gold at the nano-scale has a rich and long history, which began from ancient Roman times with the famous example of the Roman glass Lycurgus cup designed in the 4th century. [170] The investigations on nanosized Au began over 150 years ago with M. Faraday's work, [171] and modern research during several decades has seen the appearance of numerous publications, including various reviews on its synthesis, surface functionalization, investigation of chemical and physical properties for applications in different fields. [172], [173], [174], [175] Nanosized noble metals, and especially gold nano-objects, are well known for their strong localized surface plasmon resonance (SPR) in the visible part of the electromagnetic spectrum, which can be tuned by varying several parameters including their size, shape, concentration and surface state offering them an appearance of unique optical properties. Additionally, they present interesting conductivity, redox properties, fluorescence, high electronic density, efficient conversion of light-to-heat providing motivating photothermal properties, stability and biocompatibility. Moreover, other undoubtable advantage consists in the very developed surface chemistry. Indeed, different functional groups, such as thiols, phosphines, and more rarely amines and carboxylates, can be covalently anchored to the surface of the gold, exhibiting affinities towards it. For these reasons, gold nano-objects have been proposed for a widespread range of applications in biology and health, including their use as efficient therapeutic agents for specific photothermal ablation of diseases (mainly cancer) or infected by bacteria tissues, as

radiotherapy agents, as computed tomography (CT) agents, in photoacoustic and surface-enhanced raman scattering imaging (SERS). Moreover, they are employed as a component in sensors for detection of a wide range of analytes, as efficient catalysts and photocatalysts and others. [176]. Noble metals and especially nano-sized gold were also used as a part of different nanoheterostructures in combination with magnetic materials, silica, carbon nanostructures or quantum dots (QDs).[177] The synthesis of these systems was motivated not only by many multitasking applications in biology and health, in sensing and catalysis, but also for answering fundamental questions on how to improve or weaken different properties. The association of gold or other noble metals with PB(A)s is a relatively recent field of research, which started around fourteen years ago, but its rapid development provides a series of unique and fascinating multifunctional objects with different morphology, size and composition possessing complementary chemical or physical properties offering access to various applications.

This subsection describes the synthesis and features of metal@PB(A)s heterostructures classifying them by their morphologies: *(i) metal@PB(A) core@shell nano-objects, (ii) PB@metal core@satellite nano-objects, (iii) complex nanoheterostructures* (Figure 6). Note that given that this overview tackles only discrete nano-objects, numerous articles reporting the deposition of PB(A) nanoparticles on the Au surface with the aim to design modified electrodes will not be discussed here. [147], [178]

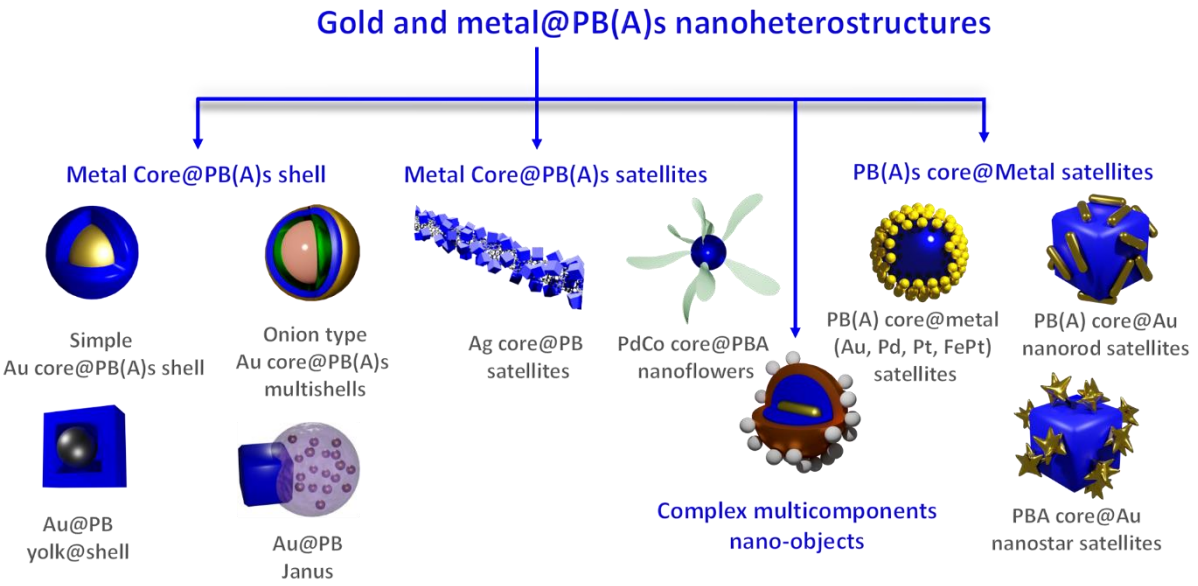

Figure 6. Main morphologies for metal@PB(A)s nanoheterostructures.

II.1.1. Metal@PB(A) core@shell or core@satellites nano-objects

The first and the most often reported type of nanoheterostructures is metal@PB(A) core@shell nano-objects, where several typologies may be evidenced. The first one concerns the well-defined nano-objects where the metal core is completely coated by a continuous shell of PB(A) with a controlled core size and shell thickness. Simple core@shell systems or an onion type core@multishell ones belong to this typology, as well as yolk@shell nano-objects. The second core@satellite morphology can be considered as an extreme case of the core@shell shape, where the shell only partially covers the core surface. It is represented by two examples, where Ag nanowires or PdCo nanoflowers with PB satellites were deposited or grown on the metal

surface. In this case, the satellites may be obtained in the form of spheres, cubes or more sophisticated shapes of flowers.

Concerning the first type of core@shell nanoheterostructures, several unsuccessful attempts with no clearly distinguishable Au@PB(A)s core@shell morphology, and sometimes aggregation of nano-objects were reported first.[16], [179], [180, 181] In this context, the pioneering work to the synthesis of discrete Au@PB nano-objects of 30 – 60 nm was reported in 2007. These objects were deposited as thin films on the indium tin oxide (ITO) surface by a layer-by-layer technique to design an electroactive sensor of hydrogen peroxide.[16] We can also cite the synthesis of some aggregated Au@PB nano-objects of around 18 nm prepared for biomedical applications[179] or for electrochemical detection of hydrogen peroxide[180], as well as the preparation of Pt@PB nano-objects, where several small Pt nanoparticles (around 2 nm) have been enwrapped by PB leading to relatively aggregated objects of 20 nm in size.[182], [183] Generally, these nanoparticles were prepared by the addition of hexacyanoferrate and iron salts precursors on previously prepared spherical Au or Pt nanoparticles stabilized by citrate or by a mixture of citric/tannic acid. In all these attempts, the control of size and morphology was difficult to achieve. Noteworthy, transmission electronic microscopy (TEM) images show not clearly distinguished metallic core and coordination polymer shell and the often-occurred aggregation. Moreover, recently reported Au@PB system based on this synthetic approach indicates that a true core@shell morphology can be obtained only in the case of very small Au nanoparticles of 3 nm, and a gold core aggregation happened when the size of the gold nanoparticles increased. [169]

The first work demonstrating the formation of true core@shell nanoparticles with a clearly distinguished Au core and PB(A) shell and an interface was published by Y. Guari and coll.[165], [166], [168] The employed original two-step strategy consists in: (*i*) the synthesis of cyanide-stabilized gold nanoparticles in water by reduction of the dicyanoaurate precursor $[Au(CN)_2]^-$ by potassium borohydride,[167] and (*ii*) the subsequent time-controlled growth of the cyano-bridged coordination polymer shell on the surface of these gold nanoparticles (Figure 7a). Using this methodology, Au@$KNi^{II}[Fe^{II}(CN)_6]$ core@shell nano-objects of *ca*. 52 nm were designed and characterized (Figure 7b). [165] Note that the size of the Au core remains the same during the shell growth. The decisive role of the cyanides surrounding the Au core nanoparticles to direct the growth of the PBA shell was demonstrated. Moreover, it was shown that the formation of the PBA shell occurs *via* the coordination of the Ni^{2+} and/or ferrocyanide moieties on the gold surface at the beginning of the growth process rather than during a post-synthetic redistribution of the negatively charged PBA nanoparticles on the gold surface. The Au@PBA interface in this system with different PBA shell thicknesses were investigated by the X-ray photoelectron spectroscopy (XPS) technique, and the presence of Au^I/CN^- and/or Au^{III}/CN^- species located on the surface of the gold nanoparticles was clearly demonstrated. [168] These species stabilize the gold nanoparticles in solution and represent anchoring points to growth PBA shells through coordination of divalent metal ions. Figure 7b shows TEM image of these nanoparticles, where the gold core of *ca*. 20 nm and the PBA shell of around 15 nm can be clearly visible. The morphology of the latter may be described as several nested cubes grown around the icosahedral gold core (Figure 7c). The possibility to control and modulate not only the size of the gold core, but also the $KNi[Fe^{II}(CN)_6]$ shell thickness has also been proved.

This strategy was extended to the synthesis of core@shell nano-objects with other shell compositions, such as PB, [167] $KCo[Fe^{II}(CN)_6]$ or $KNi[Cr(CN)_6]$. [168], [166] Moreover, it was possible to design multi-shell systems by the epitaxial growth of a second PBA's shell on the surface of the first one by fine tuning of the reaction conditions. In these onion-type systems, the shell composition and the shell thickness may also be modulated. Figure 7d shows the TEM images of such $Au@KNi[Fe^{II}(CN)_6]@KNi[Cr^{III}(CN)_6]$ core@shell@shell heterostructures with clearly distinguishable core, shells and interfaces. Note that there is no atomic redistribution in these shells, as attested by the STEM-HAADF image showing the localization of the Fe atoms close to the Au core and the Cr ones on the periphery (Figure 7e).

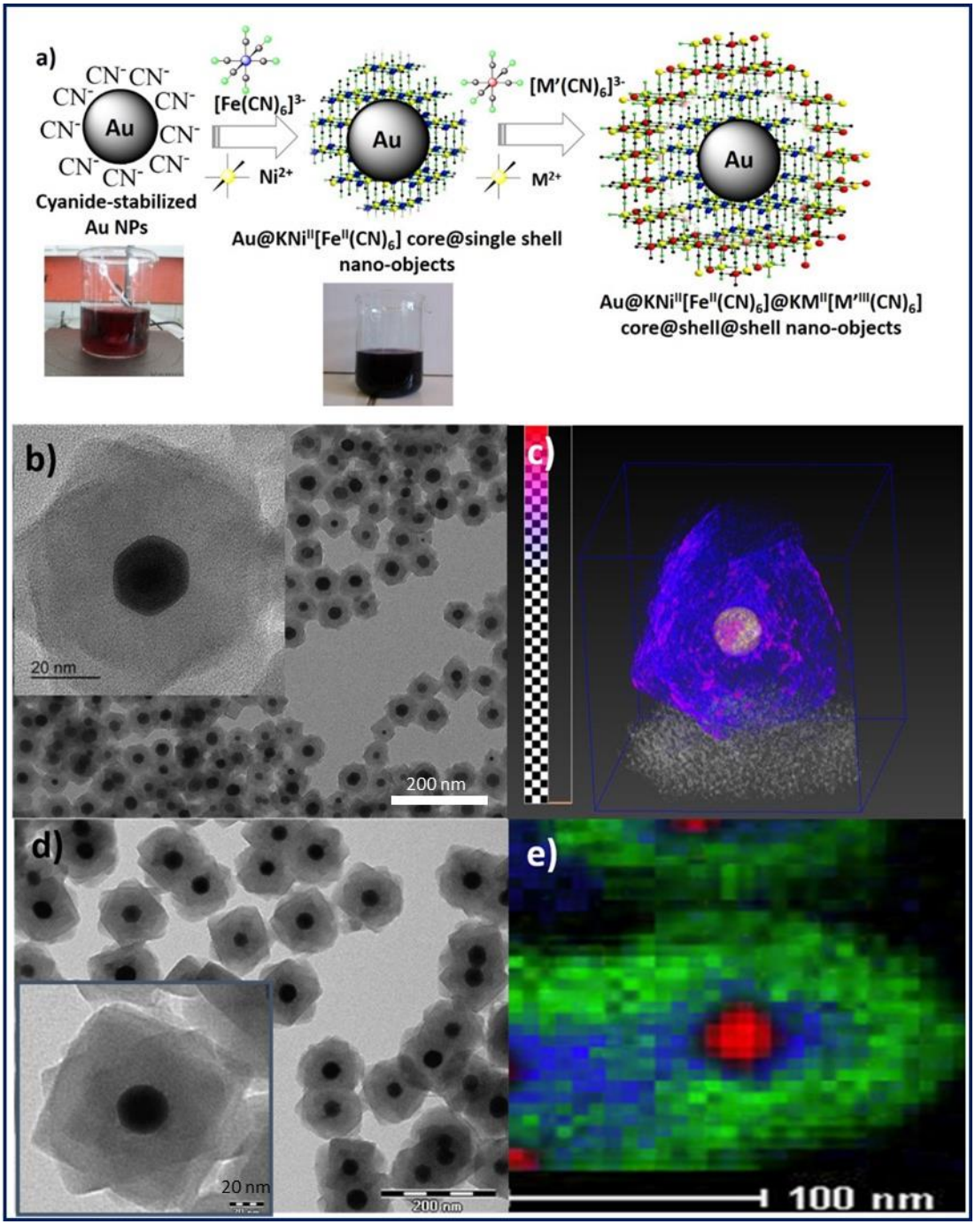

Figure 7. a) Schematic representation of Au@PBA core@shell and Au@PBA@PBA' core@shell@shell nanoparticles design; b) TEM images of Au@KNi^{II}[Fe^{II}(CN)$_6$] nanoparticles. Insert: Magnification of the TEM image showing one nanoparticle; c) One of the perspectives of the 3D reconstruction image for sample Au@KNi^{II}[Fe^{II}(CN)$_6$] obtained using tomography technique; d) TEM images of Au@KNi[Fe^{II}(CN)$_6$]@KNi[Cr^{III}(CN)$_6$] core@shell@shell nanoparticles. Insert: Magnification of the TEM image showing one nanoparticle; e) STEM-HAADF image of Au@KNi[Fe^{II}(CN)$_6$]@KNi[Cr^{III}(CN)$_6$] core@shell@shell with the EDS mapping showing the gold (red), the nickel (light blue), and the iron (dark blue) and the chromium (green) atoms. Adapted from Ref. [165, 166] with permission from John Wiley and Sons.

Therefore, this approach provides a series of core@shell nanoheterostructures with the related optical properties of the gold core (SPR band) and the magnetic properties of the PBA shells. It was demonstrated that: *i*) the optical properties of these systems (the position of the SPR band and its intensity) vary as a function of the shell thickness and its composition, and *ii*) the magnetic properties of the heterostructures may be tuned by modulating the magnetic shell thickness and also the overall morphology. A specific role of the interface in the magnetic properties linked with the spin frustration on the surface and on the interface was demonstrated. As a variation of this strategy, nice Au@PBA heterostructures demonstrating well-formed isolated Au core covered by a well-rounded PB shell were more recently designed through the etching of the Au core by cyanide of ferricyanide moieties providing an anchoring of the cyanide ligands on the surface of the gold and further formation of the PB shell. [164], [184], [185], [186], [187] They have been proposed as new nanoprobes for SERS enhanced imaging [164], [185], [187] as nanomedicines for SERS-guided PTT/PD therapy, [184] or as MRI/SERS bimodal nanoprobes for cell tracking. [186] In these systems, the initially prepared Au nanoparticles stabilized with citrates were treated by CN^- or $[Fe(CN)_6]^{3-}$ moieties in order to exchange the citrates situated on the gold surface by the cyanide ligands. As an example, core@shell nano-objects of *ca.* 70 nm were obtained by growing the PB shell by classical self-assembling reactions between hexacyanoferrate and iron salt (Figure 8a). The authors demonstrated the presence of a spherical gold core of around 30 nm and a spheric-like PB shell by TEM and HAADF-STEM images (Figures 8b, c). [164] Obviously, the presence of cyanides on the surface of the Au core is crucial for the further growth of the well-formed cyano-bridged shell. The optical properties of the obtained nano-objects resemble the previously described ones with a decrease of the SPR signal intensity and the appearance of the Fe^{3+}-to-Fe^{2+} charge transfer band between 600 – 900 nm due to the presence of the PB shell (Figure 8d).

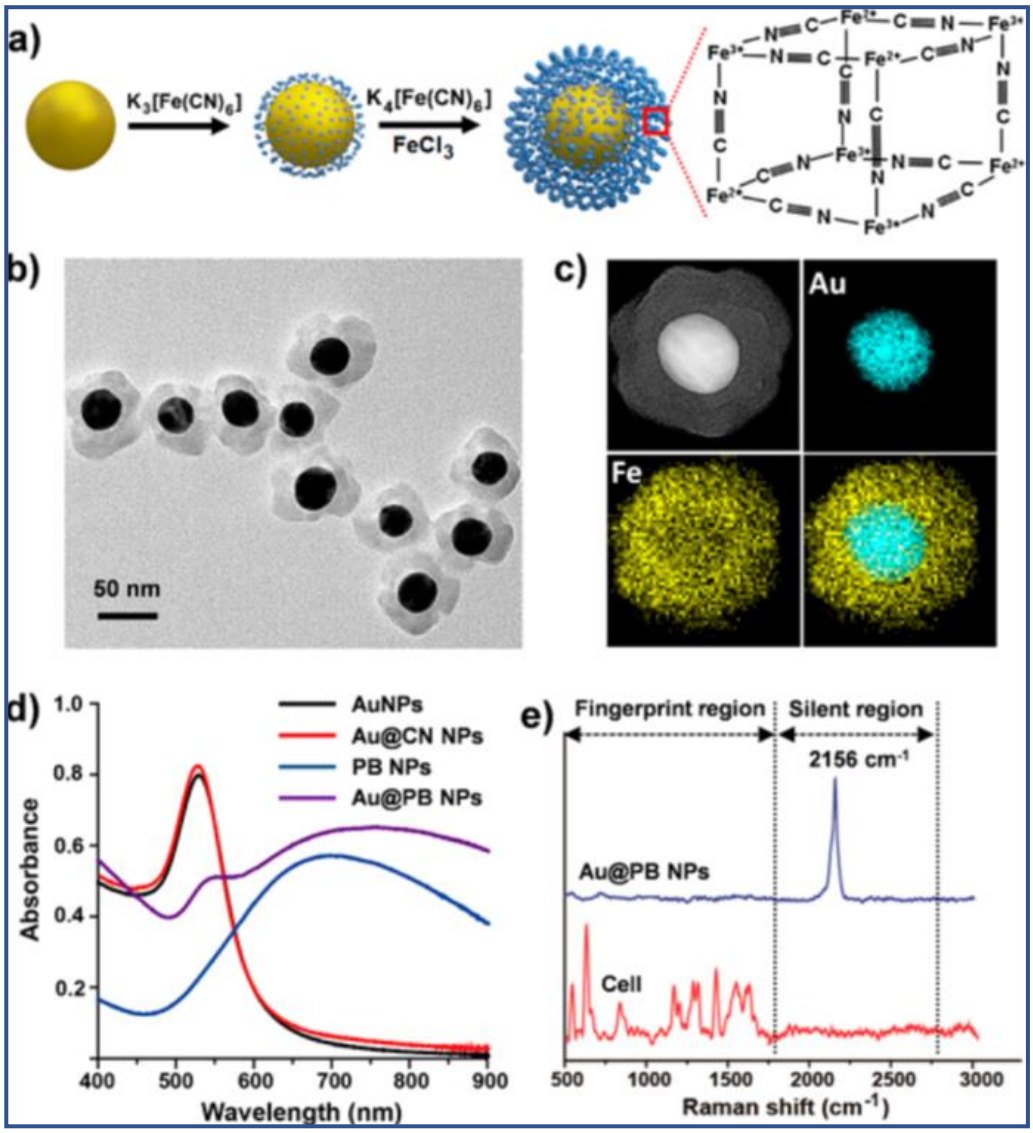

Figure 8. a) Schematic illustration of the Au@PB core@shell nanoparticle synthesis; b) TEM image of the Au@PB core@shell nanoparticles; c) HAADF-STEM images of Au@PB nanoparticles and EDX elemental mapping of Au core (blue), PB shell (yellow), and the merged image; d) UV−vis spectra of Au NPs (black), Au@CN NPs (red), PB NPs (blue), and Au@PB NPs (purple) showing the change in the SPR band with PB coating; e) The Raman spectra of Au@PB nanoparticles and HepG2 cells. Reprinted with permission from Y. Yin, Q. Li, S. Ma, H. Liu, B. Dong, J. Yang, D. Liu, Analytical Chemistry, 89 (2017) 1551-1557. Copyright 2021 American Chemical Society. [164]

Yolk@shell is a particular type of core@shell morphology, which consists in an exterior hollow shell with interstitial void space and an interior core. [188] These nanostructures present many advantages over the simple core@shell shape thanks to the presence of free interior void space, porous hollow shell and free core surface. An elegant strategy to design well defined Au@PB yolk@shell nano-objects was recently reported by Q. Zhang and coll. It consists first in preparation of the template Au@Ag nanocubes of around 150 nm by the seed-mediated growth process and then their mixing with $K_3[Fe(CN)_6]$ and $Fe(NO_3)_3$ precursors in diluted conditions (Figure 9). [189] This reaction leads first to the formation of the $Ag_4Fe(CN)_6$ intermediate on

the surface of the Au, which in its turn reacts with the iron nitrate and dissolves by forming the PB shell of *ca*. 55 nm. Consequently, nice Au@PB yolk@shell nano-objects of around 200 nm possessing a large surface area and a narrow pore size (1-2 nm), which may be visible on TEM and HAADF-STEM images, were formed (Figure 9). They were used for the loading of the antitumoral drug doxorubicin to combine chemodynamic therapy of cancer cells based on Fenton catalysts associated with the CT imaging.

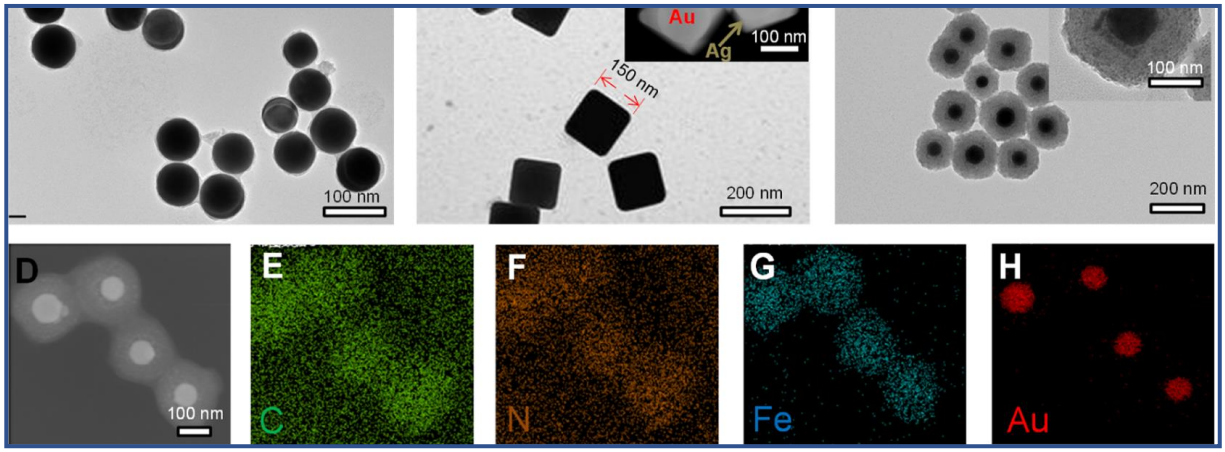

Figure 9. TEM images of Au NSs (A); Au@Ag NCs (B); Au@PB NCs (C); inset of (B): HAADF-STEM image of Au@Ag NCs; inset of (C): high-magnification TEM image of Au@PB NCs. (D−H) Mapping image of Au@PB NCs. Adapted with permission from L. Hang, H. Li, T. Zhang, D. Men, C. Zhang, P. Gao, Q. Zhang, ACS Applied Materials & Interfaces, 11 (2019) 39493-39502. Copyright 2021 American Chemical Society. [189]

The core@satellite typology is presented through two examples (Figure 6). The first one consists in the growth of PB nanocubes on the surface of Ag nanowires performed by the classical time-controlled reaction between $K_4[Fe(CN)_6]$ and $FeCl_3$ precursors in the presence of already formed Ag nanowires with the aim to obtain water-based ink for direct screen-printed flexible biosensor chips. [190] The second example are hybrid nanoflowers that were obtained by an original approach consisting, first, in the formation of the $K_2PdCl_4/K_3[Co(CN)_6]$ gel in polyethylene glycol (PEG), which after thermal treatment at 150 °C, gave $PdCo@PdCo(CN)_6$ nanoflowers through a nucleation – aggregation – dissolution - recrystallization mechanism. Note that these intricate nanostructures exhibit a remarkable catalytic activity and durability towards the reduction of rhodamine B by $NaBH_4$ and may hold a great promise in the water remediation field. [191]

II.1.2. PB core@Metal satellite nano-objects

The second relatively often occurred in the literature morphology of nanoheterostructures belongs to PB(A)@metal satellites typology, where the classic cubic core of the coordination polymer is surrounded by metal nanoparticles of different shapes, such as spherical one, nanorods of nanostars. The satellites may be located in the porosity of the PB(A) core or situated on the surface. In this latter case, both, the direct anchoring of the metallic satellite on the PB(A)'s surface or the attachment through organic ligand (covalent or electrostatic) have been reported. Finally, we cite in this subsection the unique example of Janus PB@Au nanoparticles.

Several unfruitful attempts consisted in the chemical reduction of K_2PtCl_6 precursor by $K_4[Fe(CN)_6]$ in the presence of freshly prepared PB nanoparticles in colloidal suspensions. [192], [193] In these cases, no clearly formed core, shells or satellites nanoparticles were demonstrated.

Firstly, interesting results were recently obtained by the adsorption of molecular precursors on the PB(A) surface, followed by a chemical reduction. Thus, $Co_3[Co(CN)_6]$ cubic nanoparticles with clearly definite tiny Pd nanoparticles on the surface were obtained by the simple adsorption of palladium chloride followed by reduction with ethanol. [194] Similarly, $Co_3[Fe(CN)_6]$ and $Ni_3[Fe(CN)_6]$ nanocubes with small Pt satellites were obtained after H_2PtCl_6 adsorption on their surface followed by the H_2 reduction under heating[195], [196] and proposed as new catalysts or electrocatalysts with improved efficiency, stability, easy separation and excellent reusability in comparison with the related metallic nanoparticles. Figure 10a-d shows TEM and HRTEM images of $Co_3[Fe(CN)_6]$@Pd core@satellites showing the cubic PBA core and Pd nanosatellites most likely situated in the surface porosity of the PBA, as well as the atomic distribution demonstrating that Pd nanoparticles are homogeneously distributed on the whole surface of the cubes. A slightly different procedure has been employed to the design of PB@FePt nanoparticles (Figure 10e, f), where a mixture of Pt(II) pentadione and Fe(III) pentadione precursors were adsorbed on the surface or more likely captured in the porosity of PB nanocubes of 80 nm stabilized by citric acid. These precursors were then reduced by ethylene glycol, providing the formation of small FePt nanosatellites. Figure 10 shows TEM images of the pristine PB nanoparticles and the final PB@FePt nanoheterostructures with clearly visible spherical FePt nanoparticles covering the whole cube surface. These nanoheterostructures exhibit peroxidase-mimicking activity for calorimetric determination of hydrogen peroxide in living cells. Similarly obtained PB@FePt core@satellites nano-systems of 130 nm functionalized with hyaluronic acid and PEG have been promoted as theragnostic agents presenting dual chemodynamic/PT therapies and triple-modal MRI, CT and PA imaging. [197] A similar strategy consisting in the reduction of a bimetallic $[Au^{I}_2Ag^{I}_2(C_6F_5)_4(OEt_2)_2]_n$ molecular complex in the porosity of nano-sized PB(A) has been employed to design of PBA@Au/Ag core@satellites nanoheterostructures, where small Au/Ag alloy satellites of 3 nm have been inserted/deposited on the surface of cubic $K^+/Ni^{2+}/[Cr(CN)_6]^{3-}$ nanoparticles of 62 nm. An interesting light irradiation-assisted catalytic activity for the 4-nitrophenol reduction and modified magnetic properties have been observed due to the presence of the Au/Ag alloy on the PBA surface. [198] This work constitutes one of the rare exemple of core@Au-Ag satellites architectures in which an interplay between the two entities gold and PBA leads to a drastic change of the magnetic properties.

Another method to obtain PB(A) core@metal satellite nanoheterostructures was used through the assembly of separately synthesized core and satellite nano-objects through different ligands attached to the PB(A) surface. A nice example has recently been obtained for $K_{0.07}Ni[Cr(CN)_6]_{0.69}$@Au core@satellites with different shapes of the gold nano-satellites, such as spherical nanoparticles, nanorods and nano-stars. These Au nano-objects were covalently attached to the PBA surface through the thiol-polyethyleneglycol-amine ($HS\text{-}PEG\text{-}NH_2$) ligand (Figure 11). [199] The nanoheterostructures exhibited both, magnetic properties of PBA and the SPR phenomenon, which depends on the shape of the corresponding Au nano-satellites. Two other works have been devoted to the coverage of PB(A) nanoparticles with spherical Au

nanoparticles with the help of electrostatic interactions. Indeed, the electrostatic adsorption of citrate stabilized Au nanoparticles of 13 nm on the surface of PEI modified PB cubes (87 nm) was reported. After PEGylation, the average diameter of the final nanoheterostructures was around 139 nm. These nanoparticles were proposed as multifunctional theragnostic agents for MRI/CT imaging and synergic PTT and radiosensitive therapy of cancer. [200] Another work presented small Au nanoparticles attached to BSA coated PB or Ni(II)-based PBA giving rather aggregated nano-objects of about 200-300 nm, but Au nanoparticles are clearly visible on the surface by TEM imaging. Note, however, that in these latter cases, there is no direct interface between two inorganic components because PB(A)s nanoparticles are enwrapped by an important amount of stabilizing agent. [201], [202], [199]

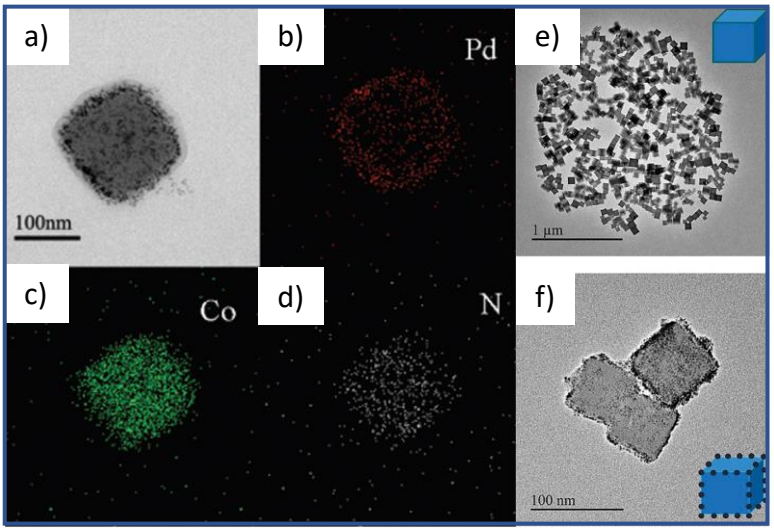

Figure 10. TEM images of $Co_3[Fe(CN)_6]$@Pd nanoheterostructures showing: a) the cubic PBA core and Pd satellites most likely situated in the surface porosity of the PBA, the atomic distribution for b) Pd, c) Co, and d) N; and e), f) TEM images PB@FePt nanoheterostructure showing the PB cubic core and the FePt satellite nanoparticles. Reproduced from Ref. [194] [203] with permission from the Royal Society of Chemistry.

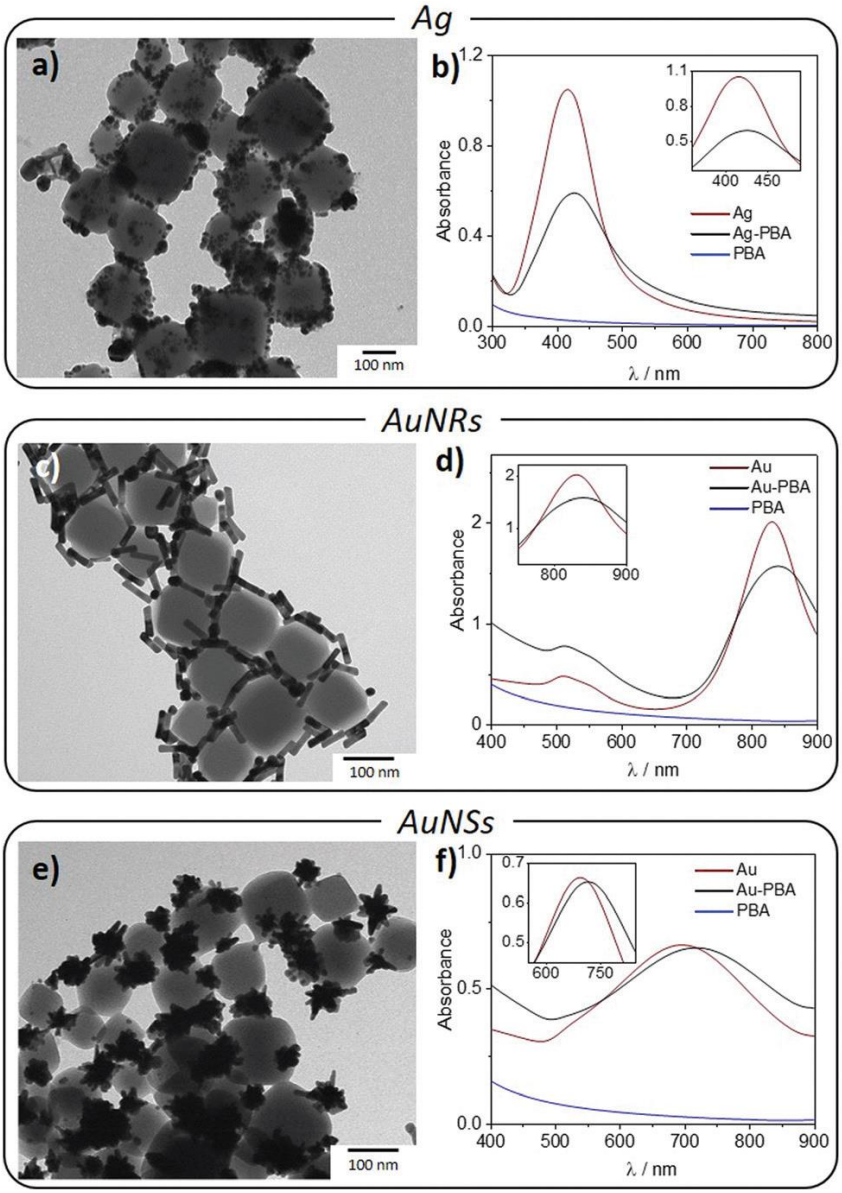

Figure 11. TEM images of $Ni^{II}Cr^{III}$-PBA@Au core@satellites nanoheterostructures with spherical (a), nano-rods (c) and nanostars (e) Au satellites and their corresponding electronic spectra showing the plasmon band. Reproduced from Ref. [199] with permission from the Royal Society of Chemistry.

Finally, we would like to mention in this subsection the first example of a particular Janus type PB/Au morphology with a very well-defined shape, which has been recently reported by D. Li et al. [204] The synthetic strategy consists in the addition of polyacrylic acid (PAA) by adjusting the pH with aqueous NH_3 to the appropriate alkalinity in a water/isopropyl alcohol (1/6) mixture. Under such conditions, PAA was selectively coated on one of the planes of the PB nanoparticles and further growth of Au was performed within the PAA matrix (Figure 12).

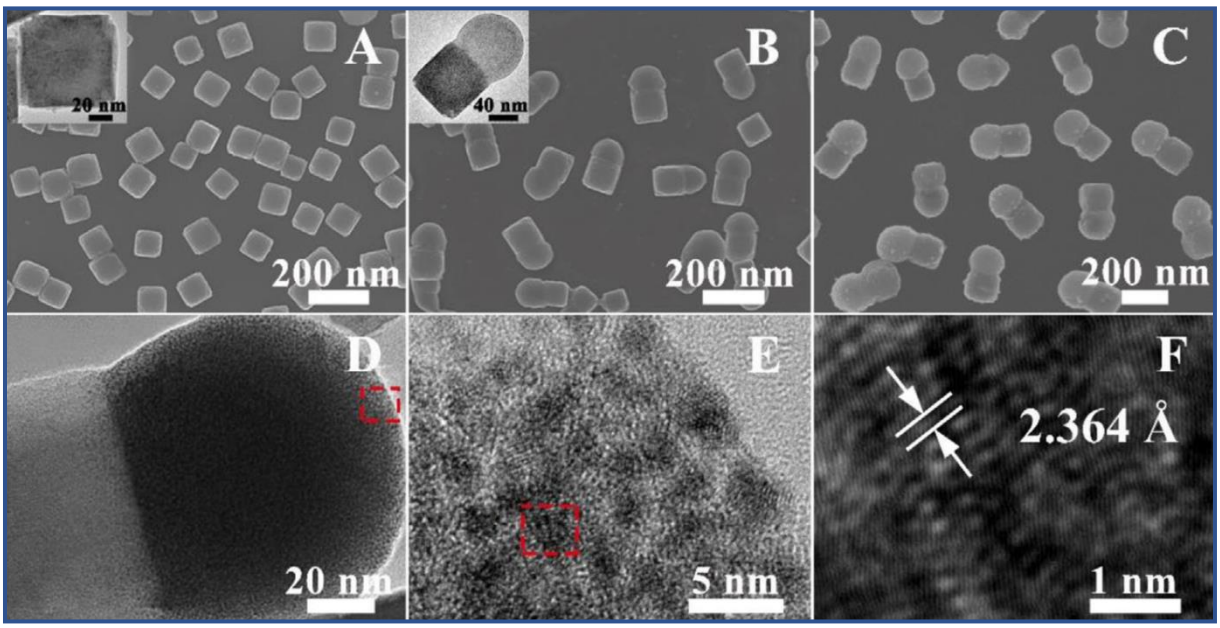

Figure 12. SEM images of: A) PB nanoparticles, inset: the corresponding TEM image of a single PB nanoparticle; B) PB@PAA Janus nanoparticles, inset: the corresponding TEM image of a single PB@PAA Janus nanoparticles; C) PB@PAA/Au Janus nanoparticles. D) TEM image of a single PB@PAA/Au Janus nanoparticles. E) Magnified HR-TEM image of the dashed boxmarked area of PAA/Au. F) Magnified HR-TEM image of the dashed box-marked area of small Au nanoparticles. Adapted from Ref. [204] with permission from John Wiley and Sons.

II.1.3. Complex nanoheterostructures

Multicomponent complex nano-objects including more than two components beyond the nano-sized metals and PBA(s) were observed through three examples. First, two nanostructures with onion-like mesoporous graphene or C_{60} decorated by nanosized Au and PB(A) were elaborated for designing electrochemical sensors with good specificity and high sensitivity for the detection of specific aptamers or antigens. [201], [202] The strategy depicted in Figure 13 [202] consists in the functionalization of the nano-C_{60} surface with thiol groups, and then the anchoring of a prepared assembly of PB/Au nanoparticles, where Au nanoparticles were attached to BSA modified PBA cubes. This approach gave relatively aggregated objects with no clearly distinguishable core, but the metallic Au nanoparticles situated in the organic BSA shell are clearly visible.

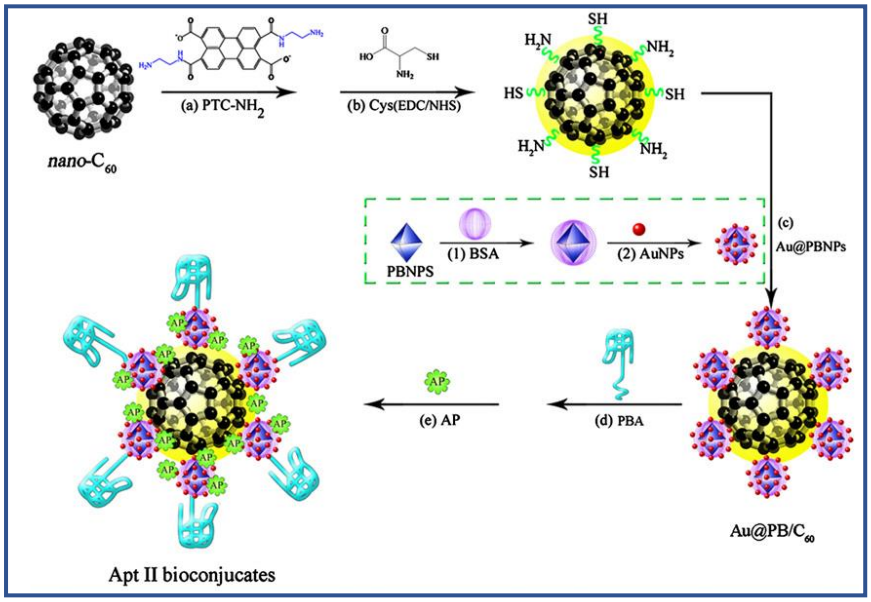

Figure 13. Schematic representation of two-step design of C_{60}@PBA/Au nanoheterostructures and their post-synthetic functionalization with alkaline phosphatase (AP) for further detection of aptamers (APT II). Adapted from Ref. [202] with permission from Elsevier.

Another interesting example of complex heterostructures was developed aiming to design a smart plasmon-induced resonance energy transfer-mediated nanoplatform for multimodal imaging-guided phototherapy. The Au@PB@Cu_2O@QDs nanoheterostructures contain four different inorganic components with their own physical and chemical properties and present a highly multifunctional character. They are based on Au nanorods as a core coated by a PB shell of around 10 nm with a second Cu_2O shell gowned on. The fourth component, phosphorus spherical quantum dots were coupled with the Cu_2O layer *via* electrostatic interactions. Finally, the structure was covered by poly(allylamine), serving as a modified layer to increase water stability and biocompatibility. [205] Their fascinating properties and applications are discussed in Section III.3.

II.2. Metal oxide or sulfide@PB(A)s nanoheterostructures

The combination of PB(A)s with metal oxides at the nanoscale to afford discrete nanoheterostructures has been thoroughly investigated in the last decade. Among metal oxides, magnetic ferrites (magnetite and mainly cobalt ferrite) and maghemite have been the most considered because they bring additional magnetic properties (superparamagnetic or ferrimagnetic behaviour) useful for magnetic guidance, magnetic removal of adsorbents or MRI, as well as peroxidase-like activity. These properties combined with the ones of the PB(A)s are of interest for the design of immunosensors or theragnostic agents for biomedical applications, which represent two main applicative areas of such discrete nanoheterostructures. Also, they allow to exploit the possibility of magnetic separation for the selective removal of mobile radioactive elements, such as caesium. Among non-magnetic metal oxides, in particular, cerium and manganese oxides have been combined with PB(A)s.

Otherwise, the combination of metal sulfides with PB(A)s was relatively scarcely studied, with only three reports published to date. Such combinations were developed to afford materials for applications as modified electrodes for sensing, photoelectrocatalysis or microwave adsorption.

II.2.1. Metal oxide/PB(A)s nanoheterostructures

The nanoheterostructures combining metal oxides with PB(A)s have been designed according to two different morphologies: *(i) metal oxide core@PB shell/satellites nano-objects, (ii) PB(A)s core@metal oxide satellites nano-objects*. Note that the nano-objects of the former typology are by far the most numerous, but in most cases, the core nanoparticles are relatively aggregated, and it is relatively difficult to clearly distinguish the core, the shell or the satellites. However, in several works described below, the authors achieved to design discrete milticore@shell nanoheterostructures clearly visible by TEM. In some cases, these nanoheterostructures were further combined with other inorganic components to achieve complex multicomponent nanostructures, or they were functionalized with organic biomolecules or polymers for specific applications.

Among these nanoheterostructures, mainly magnetic oxide ferrites, such as magnetite (Fe_3O_4), maghemite (γ-Fe_2O_3) and cobalt ferrite (Co_3O_4), were used as components in combination with PB(A)s. In this respect, the Massart method, [206] which consists of the co-addition of two (Fe^{II} and Fe^{III}) iron salts under basic conditions in water, is by far the most used approach to elaborate nanosized Fe_3O_4. [207], [208], [209], [210], [211], [212], [213], [214] A further controlled additional oxidation step was used to produced γ-Fe_2O_3. [215] The latter was also elaborated from $FeCl_3{\cdot}6H_2O$ by using the reduction with $NaBH_4$. [216] Moreover, in few cases, PB(A)s were combined with Co_3O_4 obtained from $CoCl_2{\cdot}6H_2O$ by employing urea assisted synthesis [217] or with Fe_3O_4 obtained by the polyol method, *i.e.* ethylene glycol assisted procedure. [218], [219] Non-magnetic oxides or hydroxides, such as CeO_2, [220] MnO_2 [221], [222] or α-$Co(OH)_2$ [223] were also considered as cores or satellites in association with PB [220], [221] [222] or PBAs [223] for design nanoheterostructures with potential applications as supercapacitors [222], [67, 70], immunosensors[220] or in nanomedicine. [221], [224] In the following sections, we will describe the design of the metal oxide/PB(A)s nanoheterostructures, giving a special emphasis on their morphology, as well as on their properties.

II.2.1.1. Metal oxide core@PB shell or satellites nano-objects.

Attempts to grow the PB shell in the single metal oxide core@PB shell structure were always elaborated in acidic conditions because reversible adsorption of iron ions occurs on the surface of the Fe_3O_4 or γ-Fe_2O_3 cores. [225] Such reactive surfaces with an appropriate surface charge were therefore exploited towards the formation of a PB shell in one step by adding a single cyanoferrate precursor: the iron oxide nanoparticles act both, as a reservoir of electrons and as iron ions source. Otherwise, a classical addition of two precursors, the hexacyanoferrate and iron ions, was also performed.

(i) One-step "single cyanoferrate precursor" strategy

This strategy based on a single cyanoferrate precursor addition for the growth of a PB shell on the surface of iron oxide nanoparticles was used first in 2010 by Y. Zhang and coll., starting from γ-Fe_2O_3 nanoparticles of 9.5 nm as a core and by adding various amounts of $K_4[Fe(CN)_6]$ at pH = 2 to growth the thin PB shells. A relatively small γ-Fe_2O_3@PB nanoheterostructures with the size of *ca.* 10 nm were obtained. [215] Note that the surface charge of γ-Fe_2O_3 nanoparticles was positive in diluted acidic solution (measured zeta potential is about 30 mV), assuring the electrostatic attraction of negatively charged $[Fe(CN)_6]^{4-}$. This latter may also

coordinate Fe^{3+} ions situated on the surface of the iron oxide nanoparticles, which might result in its chemisorption. Both hypotheses, therefore, explain the efficient adsorption of $[Fe(CN)_6]^{4-}$ on the surface of the iron oxide core. The authors postulated that further coordination of Fe^{3+} released from γ-Fe_2O_3 nanoparticles generated the PB coating on the surface of the iron oxide nanoparticles. TEM images, however, did not present the nano-objects with clearly definite shells and cores. Further functionalization of the obtained nano-objects was then considered to perform an enzyme immunoassay for IgG (see section III.3). A very similar protocol was used by P. Sreearunothai and coll. in 2013 with the addition of $[Fe(CN)_6]^{4-}$ at pH = 2 on superparamagnetic Fe_3O_4 core prepared using the Massart's method. [226] The as-obtained core@shell Fe_3O_4@PB nanoheterostructures were used for the Cs^+ removal in radioactive waste decontamination (see section III.4.2) [226]. This protocol was further adapted by Z. Dai and coll. in 2014 [209] (Figure 14a) and by Y. Zhang and coll. in 2015 [210] to afford Fe_3O_4@PB nanoheterostructures having a magnetic core of 10-20 nm and the PB shell thicknesses of 3-6 nm. The as-obtained nanoheterostructures were used as theragnostic agents for MRI and PTT with magnetic targeting [209] or for MRI, PTT and drug delivery with magnetic targeting after further coating with gelatin containing doxorubicin. [210] However, as it can be seen from a representative example of TEM images shown in Figure 14, all these nanoheterostructures are not homogeneous regarding their size and morphology, and it is difficult to conclude about the presence of a distinct PB shell covering the iron oxide core. Most likely, the PB shell surrounds several aggregated iron oxide nanoparticles.

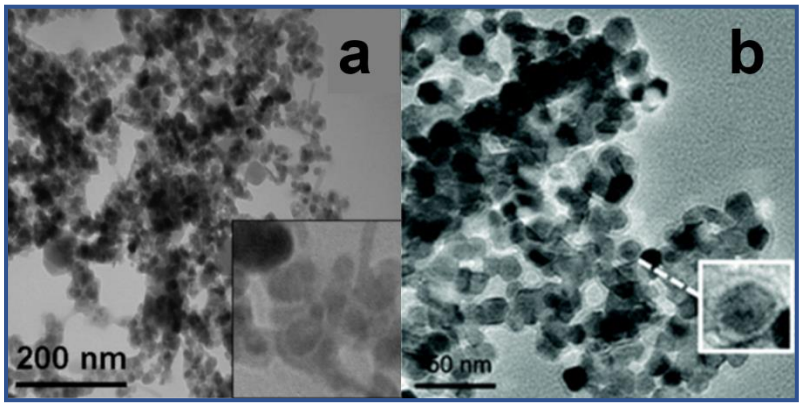

Figure 14. (a) TEM image of the Fe_3O_4@PB nanoheterostructures; b) Fe_3O_4@PB nanoparticles. Adapted with permission from G. Fu, W. Liu, Y. Li, Y. Jin, L. Jiang, X. Liang, S. Feng, Z. Dai, Bioconjugate Chemistry, 25 (2014) 1655-1663. Copyright 2021 American Chemical Society. [209] Reproduced from Ref.[214] with permission from the Royal Society of Chemistry.

In the same line of thought, F. Vianello and coll. in 2014 used the addition of $[Fe(CN)_6]^{4-}$ under acidic pH to form a PB shell on γ-Fe_2O_3 core. [216] These latter were prepared following a previously published procedure by the same authors, which consists in a $NaBH_4$ solution in ammonia assisted synthesis from $FeCl_3 \cdot 6H_2O$ in water for 2 h at 100 °C and followed by thermal treatment at 400 °C of the as-obtained powder for 2h. [227] Such synthesized γ-Fe_2O_3 nanoparticles of *ca.* 11 nm gave very stable colloidal suspensions, explained by the presence of OH^- and undercoordinated Fe^{3+} ions on their surface. [228] The formation of a PB shell was studied at different pH, and the electrocatalytic activity of such nanoheterostructures was then

tested on hydrogen peroxide, the most common electroactive substance for the PB modified electrodes (see section III.2.2).

(*ii*) *Cyanoferrate and metal salt precursors subsequent addition strategy*

An alternative strategy for the PB shell growth on the iron oxide nano-core consists in the use of two precursors, the hexacyanometallate and iron salt. It has been first exploited in 2009 by R. Yuan and coll. to design complex multicomponent heterostructures. [207] The Fe_3O_4 nanoparticles of around 10 nm elaborated using the Massart's method were coated with PB by adding the solutions of $K_3[Fe(CN)_6]$ with HCl and $FeCl_3$ with H_2O_2, subsequently leading to nano-objects of *ca*. 20 nm. They were then coated with BSA, and additional Au nanoparticles of *ca*. 1-3 nm were anchored on the surface to afford multicomponent Fe_3O_4@PB@Au nano-objects with a final size of *ca*. 80 nm. TEM images demonstrated, however, highly aggregated nano-objects. They were further functionalized by the immobilization of horseradish peroxidase (HRP), glucose oxidase (GOD), and antibody molecules to be used for the elaboration of an electrochemical immunosensor (see section III.2.1). X. Yue and coll. used the subsequential addition of aqueous solutions of the $K_4[Fe(CN)_6]$ and $FeCl_3$ precursors in a colloidal solution of Fe_3O_4 nanoparticles prepared by the Massart's method. The hydrodynamic diameter of Fe_3O_4 nanoparticles and Fe_3O_4@PB nanoparticles was evaluated as 40.1±5.1 nm and 54.2±2.9 nm, respectively.[212] Such nanoheterostructures were further functionalized with polyethyleneimine (PEI) followed by the immobilization of quantum dots and grafting of hyaluronic acid (HA) to afford theragnostic agents for MRI, PTT, fluorescence imaging and magnetic targeting (see Section III.3.2.1). In 2018, P. Xue and coll. [213] and Y. Wang and coll. [214] uses the same strategy to obtain Fe_3O_4@PB nanoparticles presented smaller size in comparison with the previously described work: the iron oxide core size was estimated to be 5-8 nm and the PB shell of 3-5 nm (Figure 14b). The surface of these Fe_3O_4@PB nanoparticles was further modified by pegylation followed by their doxorubicin loading [213] or by their capping with polydopamine (PDA) followed by bovine serum albumin (BSA) and aluminium phtalocyanin (AlPc) loading to afford theragnostic agents (see section III.3.1.2). [214] It should be noted that again, in all these nano-objects, the PB shell surrounds aggregated iron oxide cores, and it is difficult to clearly distinguish the iron oxide core and the PB shell in comparison to what has been demonstrated for the previously described well-definite Au core@PB shell nano-objects.

This strategy was extended by R. Fernandez and coll. to nanoheterostructures with the Fe_3O_4 core and Gd^{3+}-containing PB as the shell. [211] The introduction of Gd^{3+} ions into the PB structure was performed to render these nanoparticles visible by MRI as a positive contrast agent (CA). For that purpose, the subsequent addition of $K_4[Fe(CN)_6]$ and the mixture of $FeCl_3$ and $Gd(NO_3)_3$ in acidic aqueous solutions (pH = 3) was performed onto a colloidal suspension of Fe_3O_4 nanoparticles prepared by the Massart's method. The estimated sizes were 8.0 nm and 28.2 nm for Fe_3O_4 and Fe_3O_4@Gd-PB nanoparticles, respectively. A comparison of these Fe_3O_4@Gd-PB nanoheterostructures was made with previously synthesized Fe_3O_4 and Gd-PB nanoparticles obtained by the same authors. [229], [230] The synthesis yielded Fe_3O_4@Gd-PB nanoparticles with a mean hydrodynamic diameter of 164.2 nm, which was greater than the mean hydrodynamic diameters of the constituent Fe_3O_4 (68 nm) and Gd-PB (91 nm) nanoparticles. Zeta potential measurements revealed that the Fe_3O_4@Gd-PB nanoparticles

exhibited charges (–16.5 mV) intermediate to those of the constituent Fe_3O_4 (–13.3 mV) and Gd-PB (–24.8 mV) nanoparticles. These nanoheterostructures have been proposed as multifunctional theragnostic agents for MRI diagnosis (positive CA), PTT therapy and magnetic targeting (Table 1).

Table 1. Single iron oxide core@PB shell nanoheterostructures and their properties. HRP = horseradish peroxidase ; GOD : glucose oxidase; DOX = doxorubicin ; CEA = carcinoembryonic antigen ; AFP = α-fetoprotein; PEI = polyethyleneimine; BSA = bovine serum albumin; HA = hyaluronic acid; DSPE-PEG 2000 = 1,2-distearoyl-sn-glycero-3-phosphoethanolamine-N-[amino(polyethylene glycol)-2000]; PDA = polydopamine; AlPc = aluminium phthalocyanine; PA = photoacoustic; PDT = photodynamic therapy; NIRFI = near infrared fluorescence imaging; PTT = photothermal therapy; MRI = magnetic resonance imaging; Ab2 = rabbit anti-human CD36 polyclonal antibody H-300; CD36 = recombinant human scavenger receptor class B CD36 protein. * Hydrodynamic diameter.

Ref.	Core composition	Shell/ satellites composition	Size of core@shell/satellites nano-objects (nm)	Additional component	Properties/Applications
[215]	γ-Fe_2O_3	PB	9.8-10.5	-	- Peroxidase-like activity Horseradish - Peroxidase (HRP) mimic enzyme - Enzyme immunoassay model
[226]	Fe_3O_4	PB	12-15	-	- Nano-sorbent for Cs^+ remediation
[209]	Fe_3O_4	PB	18-25	-	- T_2-weighted MRI CA - PTT agent - Magnetic targeting
[210]	Fe_3O_4	PB	20-25	DOX loaded gelatin	- PTT agent - Drug release
[216]	γ-Fe_2O_3	PB	n.c.	-	H_2O_2 detection
[207]	Fe_3O_4	PB	20	Au satellites + HRP/GOD/CEA Antibody	- Immunoassay - Detection of CEA and AFP in vitro
[212]	Fe_3O_4	PB	54	CuInS2-ZnS + PEI/BSA/HA	- T_2-weighted MRI CA - PTT agent - Magnetic targeting
[213]	Fe_3O_4	PB	12	DOX loaded DSPE-PEG 2000	- PTT agent - Magnetic targeting - Drug release
[214]	Fe_3O_4	PB	15-20	PDA/AlPc/BSA	- T_2-weighted MRI CA - PA CA - NIRFI agent - Magnetic targeting - PTT agent - PDT agent
[211]	Fe_3O_4	Gd-PB	28		- T_1-weighted MRI CA - PTT agent
[220]	CeO_2	PB	30-60	BSA/GOx/Ab2	- Electrochemical detection of CD36
[219]	Fe_3O_4	PB	294-430*	-	- Nano-sorbent for Cs^+ remediation

[218]	Fe_3O_4	PB	318	-	- Pencil drawn electrode on paper

Two examples of magnetite core@PB shell or satellites nanoheterostructures should be particularly emphasized because, in contrast with the previously cited works, their TEM images demonstrated rather well definite discrete nano-objects of multicore@shell/satellites morphology. Interestingly, the PB deposition on the Fe_3O_4 surface has been performed by using both, a single precursor and two precursors' strategies, allowing their comparison.
H.-M. Yang and coll. published in 2017, the synthesis of such nanoheterostructures from Fe_3O_4 synthesized by the polyol method using the ethylene glycol assisted hydrothermal synthesis from $FeCl_3$ and sodium acetate. [219] B. Ning and coll. described the following year [218] the same kind of nanoheterostructure. [231] Such synthetic protocol leads to magnetic Fe_3O_4 multicores of *ca.* 270 nm. While H.-M. Yang and coll. used a single source cyanoferrate precursor strategy with $K_4[Fe(CN)_6]$ addition at pH = 2, B. Ning and coll. employed a subsequent addition of $K_4[Fe(CN)_6]$ and $FeCl_3{\cdot}6H_2O$ at pH = 2. By varying the initial concentration of $K_4[Fe(CN)_6]$, H.-M. Yang and coll. were able to increase the Fe_3O_4@PB size from 293.8 nm, to 331.7 nm, and 429.5 nm *i.e.* a PB coverage thicknesses of *ca.* 24, 62 and 160 nm, while B. Ning and coll. observed the formation of Fe_3O_4@PB with a size of 317.7 nm, *i.e.* a PB shell thickness of *ca.* 48 nm. Both strategies lead to similar discrete nanoheterostructures made of magnetic multicores of Fe_3O_4 on which an homogeneous coverage of nanosized PB was formed, leading to a flower-like morphology. These nanoheterostructures were further used for the removal of radioactive caesium from water [219] or for the elaboration of a pencil drawn electrode on paper (see section III). [218] Note that in several cases of these nanoheterostructures, well-defined nano-objects with metal oxide multicore in the most cases covered by PB can be visible by TEM. However, it is not possible to clearly identify the typology of the PB coverage between the continuous shell and the satellites.

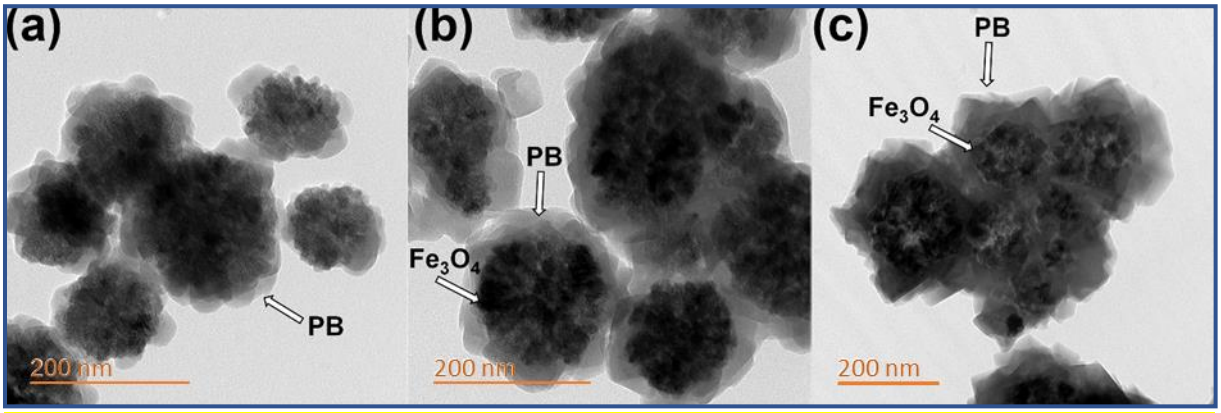

Figure 15. TEM images of multicore Fe_3O_4@PB shell/satellites nanoheterostructures prepared by the polyol method following the single source cyanoferrate precursor strategy from $K_4[Fe(CN)_6]$ with TEM images for sizes of a) 293.8 ± 7.7 nm, b) 331.7 ± 3.9 nm, and c) 429.5 ± 17.1 nmm. Reprinted from Ref.[219] with permission from Elsevier.

Among the nonmagnetic metal oxide core@PB shell or satellites nano-objects, only one example was described in 2015 by X.-F. Wu and coll. with rectangular CeO_2 nanoparticles of 20-50 nm surrounded by PB shell/satellites of *ca.* 10 nm. [220] These latter have been obtained

by a subsequential growth from $FeCl_2 \cdot 4H_2O$ and $K_3[Fe(CN)_6]$ precursors on the surface of poly(dimethyldiallylammonium chloride) coated CeO_2 nanoparticles, and PDDA has been proposed as a positive anchorage to the PB satellites. These nanoheterostructures were further functionalized with the rabbit anti-human CD36 polyclonal antibody H-300 (Ab2) and GOD to be used in an electrochemical immunosensor device (see section III.2.1).

II.2.1.2. PB(A) core@metal oxide shell or satellites nano-objects.

(*i*) *One-step single cyanoferrate precursor strategy*

Several reports deal with the preparation of PB(A) core@metal oxide shell or satellites nano-objects, starting from the first PB core@Co_3O_4 satellites nanoparticles published in 2015 by B. Zhang and coll. Their synthesis contains first the preparation of the PB nanocubes of *ca.* 200 nm from $K_3[Fe(CN)_6]$ as the sole precursor under acidic conditions in the presence of PVP, followed by the growth of Co_3O_4 satellites using the reduction of $CoCl_2 \cdot 6H_2O$ by urea. [217] The catalytic oxidation of peroxidase substrates, such as *o*-phenylenediamine (OPD) and 3,3',5,5'-tetramethylbenzidine in the presence of H_2O_2, *i.e.* the enzyme mimicking the activity of these discrete nanoheterostructures, was then evaluated (see Section III.2.2). Similar protocol based on the unique $K_4[Fe(CN)_6]$ precursor for the synthesis of PB as the core followed by the growth of manganese oxide shell was used by B. Khatua and coll. in 2017 to afford PB@MnO_2 nanoheterostructures. [222] The PVP/$K_4[Fe(CN)_6]$ ratio was decreased by *ca.* 6, leading to the formation of the PB microcubes. Then, a deposition of MnO_2 on their surface was done by reduction of $KMnO_4$. TEM and SEM images show micrometric objects where the typology of the MnO_2 is not clear. The nanostructures were then deposited on stainless steel to be used as a positive electrode in an asymmetric capacitor device (see Section III.1.1). The same year, Z. Qian and coll. reported a similar synthesis of discrete nanoheterostructures combining MnO_2 satellites and PB. [221] The protocol for the synthesis of the PB is the same as the previously described one, [217] followed by reduction of $KMnO_4$ in the acidic conditions leading to the MnO_2 formation on the PB surface. As the amount of $KMnO_4$ increased, the particle size of the obtained nano-objects decreased from ~240 to ~50 nm. For the latter, PB@MnO_2 discrete nanoheterostructures were confirmed with a size estimated to be 44.7±3.2 nm by TEM with a PB core of 39±4.2 nm and a MnO_2 shell thickness of 5.0±1.3 nm (Figure 16d).

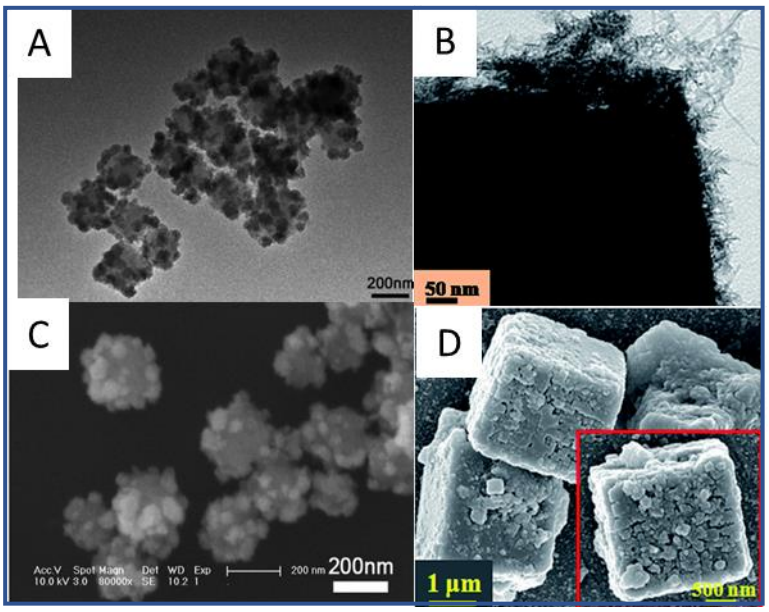

Figure 16. TEM images of nanoheterostructures: a) PB@Co_3O_4, (b) PB@MnO_2; SEM images of c) PB@Co_3O_4, d) PB@MnO_2. Reproduced from Ref. [217] [222] with permission from the Royal Society of Chemistry.

(ii) Two precursors strategy

While the one-step single cyanoferrate precursor strategy is limited towards the synthesis of PB, the co-addition strategy of hexacyanometallates and metal salts allows to elaborate different PBAs cores. This approach was used in 2018 by O. N. Oliveira Jr., W. Cantanhêde and coll. to elaborate $Co_3[Co(CN)_6]_2$@Fe_3O_4 nanoheterostructures. [208] The protocol consists in the use of $K_3[Co(CN)_6]$ and $Co(CH_3COO)_2{\cdot}4H_2O$ in the presence of Fe_3O_4 nanoparticles that were earlier prepared using the Massart's method. [232], [233] The $Co_3[Co(CN)_6]_2$ nanocubes demonstrate an average edge length of 21-140 nm, exhibiting some contacts between them with non-uniformly distributed polydisperse aggregates of Fe_3O_4 with size less than 10 nm nanoparticles on their surface. Finally, R. Liu and coll. published in 2020 the synthesis of $Zn_3[Co(CN)_6]_2$@α-$M(OH)_2$ (M = Co^{2+}, Ni^{2+}) "hairy" discrete nanoheterostructures based on the synthesis of the PBA nanospheres with a size of *ca.* 100 nm from $K_3[Co(CN)_6]$ and $ZnSO_4$ in the presence of PVP followed by the formation of the α-$M(OH)_2$ lamellar double hydroxide (LDH) using the urea assisted reduction method from $CoCl_2{\cdot}6H_2O$ and $NiCl_2{\cdot}6H_2O$. [223] This nanomaterial was then used as the working electrode in a three-electrode system and as the positive electrode in a two-electrode system to assemble an aqueous hybrid supercapacitor (see section III.1.1). Table 2 summarize some characteristics of PB(A) core@metal oxide shell/satellites nanoheterostructures and their properties/applications.

Table 2. PB(A) core@metal oxide shell/satellites nanoheterostructures and their properties. MRI = magnetic resonance imaging; Hb = Hemoglobin; PTT = photothermal therapy; PA = photoacoustic; PVP = polyvinylpyrrolidone.

Ref.	Core composition	Shell/satellite composition	Core@shell/satellite size (nm)	Additional component	Properties/Applications
[217]	PB (200 nm)	Co_3O_4	n.d.	-	- Oxidase- and peroxidase-like activities

[222]	PB	MnO_2	Several μm	-	- Positive electrode for asymmetric capacitor
[221]	PB	MnO_2	45	-	- T_1-weighted MRI CA - Oxygenated Hb T_2-weighted MRI CA - PTT agent - PA agent
[208]	$Co_3[Co(CN)_6]_2$	Fe_3O_4	n.d.	-	n.d.
[223]	$Zn_3[Co(CN)_6]_2$	α-$M(OH)_2$ (M = Co, Ni)	100 (M = Co)	PVP	- Hybrid button type capacitor

II.2.2. Metal sulfide-PB(A)s nanoheterostructures

The combination of metal sulfides with PB(A)s was relatively scarcely investigated with only three reports published to date giving three different morphologies (Table 3): *(i) CuS multicore@PB shell*,[234] *(ii) PB core@MoS_2 shell*,[235] *and (iii) CoS_2 core@PBAs* ($Co_3[Fe(CN)_6]_2$ or $Co[Fe(CN)_6]$) *shells* (Figure 17).[236] In this connection, *CuS multicore@PB shell* nanostructures of *ca.* 60 nm [237] were synthesized using first a reaction of $CuCl_2$ with Na_2S under hydrothermal conditions providing CuS nanoparticles of *ca.* 11 nm followed by the growth of the PB shell by adding $FeCl_3$, citric acid and then $K_4[Fe(CN)_6]$. Such a combination was pursued in order to confer both the high surface area, low energy gap and good ionic conductivity of PB and the suitable bandgap and high specific surface area of the CuS semiconductor in order to use these nano-objects on a modified electrode for ascorbic acid detection. [234] Secondly, PB core@Mo_2S "hairy" shell heterostructures were elaborated by synthesizing micrometric PB microcubes stabilized by PVP under acidic conditions from $K_4[Fe(CN)_6]$ followed by hydrothermal synthesis using $Na_2MoO_4{\cdot}2H_2O$, thiocarbamide and the symmetric triblock copolymer Pluronic P123; the PB microcubes serving as a template and framework for MoS_2. [235] PB@MoS_2 nanostructures were then evaluated for their microwave adsorption properties (see section III.4.3). Thirdly, the elaboration of the CoS_2 core@PBAs shell nanoheterostructures was also succeeded in a two-step procedure considering ZIF-67@PBA as an intermediate nanoparticles. [236] As a first step, the zeolitic imidazolate framework-67 (ZIF-67) nanocubes were synthesized from $Co(NO_3)_3{\cdot}6H_2O$, methylimidazole and cetyltrimethylammonium bromide (CTAB) [238] followed by the growth of $Co_3[Fe(CN)_6]_2$ or $Co[Fe(CN)_6]$ shells. In this synthesis, the ZIF-67 core releases Co^{2+} ions, which react with the hexacyanoferrates affording ZIF-67@PBAs core@shell discrete nanoheterostructures. The second step consists of the sulfidation of the ZIF-67 core using thioacetamide leading to CoS_2@PBAs core@shell nanoheterostructures, the sulfurization time being varied to afford different Co/Fe/S ratio. Those nanoheterostructures were then evaluated as a photoelectrocatalyst for oxygen evolution reaction (OER) (see section III.1.2).

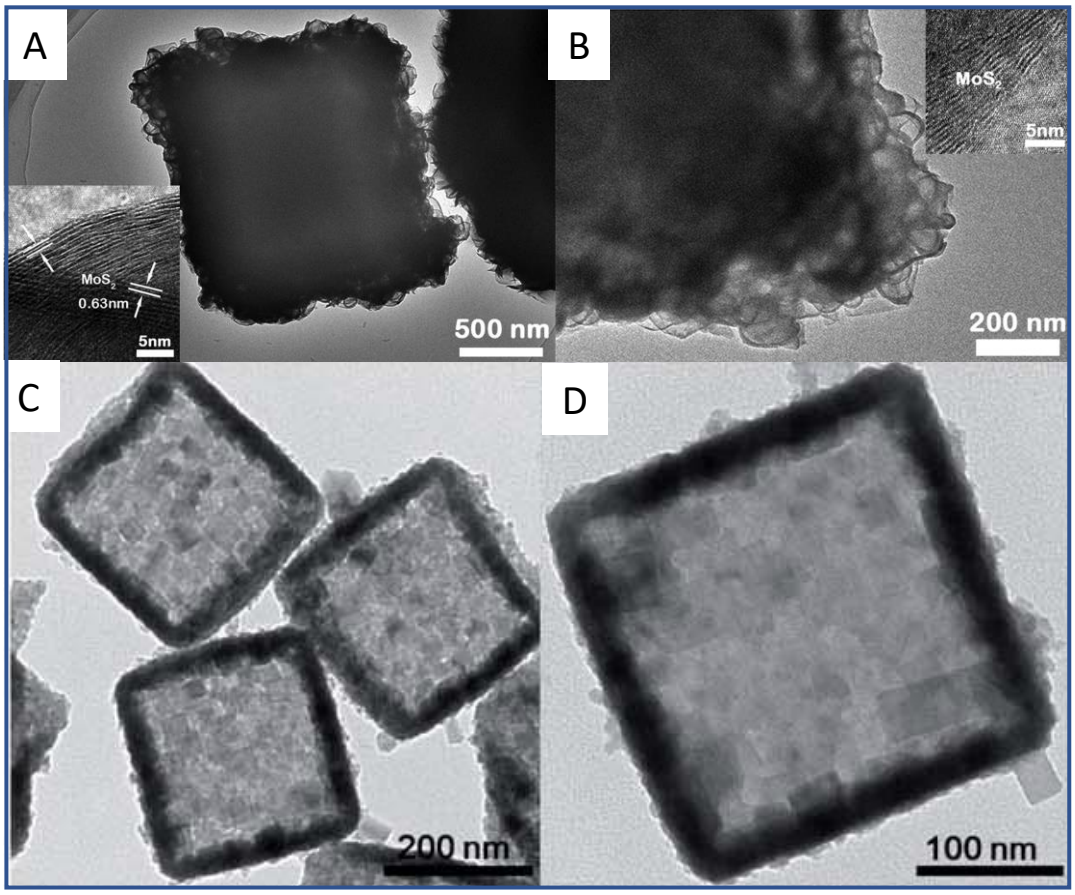

Figure 17. TEM images of (a), (b) PB@MoS_2 and (c), (d) CoS_2@PB. The insets are the HR-TEM images. Adapted with permission from L. Li, P. Zhang, Z. Li, D. Li, B. Han, L. Tu, B. Li, Y. Wang, L. Ren, P. Yang, S. Ke, S. Ye, W. Shi, Nanotechnology, 30 (2019) 325501. [235] Copyright 2021 American Chemical Society. Reproduced from Ref. [236] with permission from the Royal Society of Chemistry.

Table 3. Metal sulfide-PB(A)s nanoheterostructures and their properties.

Ref.	Core composition	Shell composition	Core@Shell size	Properties/Applications
[234]	CuS	PB	60 nm	- Ascorbic acid sensor
[235]	PB	Mo_2S	~ 1 μm	- Microwave absorption
[236]	CoFe-PBA	CoS_2	Several hundreds of nm	- Photoelectrocatalyst for Oxygen Evolution Reaction (OER)

II.3. Ln^{3+}-doped nanoparticles@PB nanoheterostructures

This section is devoted to the association of Ln^{3+}-doped nanoparticles with PB in core@shell architectures, which were developed relatively recently as the first article was published only six years ago. All these examples concern the design of smart nanoparticles for biomedical applications and particularly theragnostic agents for imaging-guided PTT therapy of cancer with *in vitro* and *in vivo* studies.

There are two nice examples of Ln^{3+} doped up-conversion nanoparticles coated with PB to enhance the PTT effect by synergetic action. The first one consists of the growth of a thin PB shell around $NaNdF_4$ nanoparticles to obtain new cross-relaxation pathways with shorter energy

relaxation distance and higher non-irradiation energy losses, which lead to an important enhancement of the PTT activity. [239] Secondly, the formation of $NaErF_4$@$NaYF_4$@$NaNdF_4$@PB nanoparticles was reported to design NIR (Er^{3+}-based) imaging-guided PTT agents. The synthetic methodology was the same in both cases. It consists of the synthesis of Ln^{3+}-doped nanoparticles stabilized by oleic acid using the flash thermolysis method followed by their treatments first with nitrosyl fluoroborate aiming to replace the oleic acid situated on the surface of the nanoparticles by BF_4^- and then further exchange of the latter with citric acid providing stabilization of the nanoparticles in water. [239] The last step is the growth of the PB shell on the surface of these citrate-stabilized nanoparticles by the addition of two precursors, hexacyanoferrate and iron salt. In both cases, a thin PB shell of 2 – 3 nm was formed on the nanoparticles' surface. Figure 18 shows the TEM images of the pristine $NaNdF_4$ nanoparticles of 17.7 nm and the $NaNdF_4$@PB core@shell nanostructures, as well as their HRTEM image. The authors also noted the aggregation tendency of the final nanoparticles with a nacked surface, which needed the presence of an additional PEGylation procedure to avoid such aggregation. [240] These nanoheterostructures represent a nice example of enhanced synergic PTT properties of both components, which are further discussed in Section III.3.1.1.

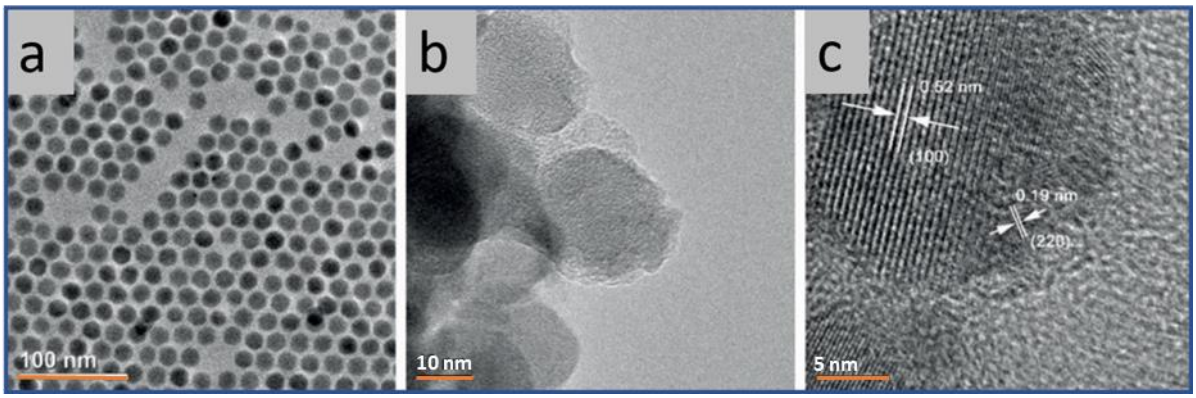

Figure 18. TEM images of a) the $NaNdF_4$ nanoparticles, b) $NaNdF_4$@PB core@shell nanostructures and c) HRTEM image of $NaNdF_4$@PB core@shell nanostructures. Adapted from Ref. [239] with permission from John Wiley and Sons.

Another example concerns the synthesis of $NaDyF_4$:*x*%Lu nanoparticles coated with a PB shell to design MRI and CT imaging-guided PTT nanomedicine. Indeed, the pristine $NaDyF_4$ nanoparticles may be used as a T_2-weighted MRI contrast agent due to the presence of Dy^{3+} ions, and its doping with Lu^{3+} provides their good visibility by CT technique. The formation of the PB shell endowed them with the PTT activity, making them efficient as theragnostic agents. The design strategy employed in this case is very similar to what was described above and consists in the replacement of oleic acid situated on the surface of the pristine nanoparticles by successive treatments with $NOBF_4$ and citric acid followed by the formation of the thin PB shell. [241] The last example of this subsection consists of a relatively complex nano-architecture containing four different components with the aim to design a multimodal nanoprobe for different types of optical imaging associated with a PTT therapy. [242] In this work, the luminescent $CaMoO_4$:Eu@SiO_2 core@shell nanoparticles of 206 nm were functionalized with free thiol groups and decorated by gold nanorods and PB nanoparticles.

These complex architectures were also conjugated with a monoclonal antibody (mAb), anti-HER2, to selectively recognize HER2/neu glycoproteins that are usually overexpressed on the cell membrane of breast cancer cells. The final nano-objects present Eu^{3+}-based luminescence, SERS signal and PTT activity under irradiation at 808 nm coming from the presence of Au nanorods and PB nanoparticles able to provide an increase of temperature up to 43 °C. [242] Since TEM images have not been provided, it is difficult to discuss morphology, shape and the aggregation state of these nanoheterostructures.

II.4. MOF or POM@PB(A)s nanoheterostructures

The association of PB(A)s with two other families of nanosized molecule-based materials, well known as metal-organic frameworks (MOF) or polyoxometallates (POM), surprisingly conducts to a very small number of nanoheterostructures despite promising properties of these latter. Note that core@shell nanoparticles of PB(A)s, where one PB(A) is epitaxially grown on the surface of another one, will not be described in this overview. The reader may find this information in previously published reviews. [46]

MOFs nanoparticles and POMs, made by transition metal or lanthanide ions connected by organic ligands, belong to two huge families of nanosized molecule-based materials with a kaleidoscopic variety of structures and functionalities. They present modulable, well-defined crystal structures, tunable physical and chemical properties, which permit them to find applications in various fields, including sensors, biology, health, separation, catalysis and others. [243], [244] [245], [246], [247], [248] The combination of these nanosystems with PB(A)s is motivated by the complementarity of their related properties. Surprisingly, only three well-investigated PB(A)@MOF or POM nanoheterostructures comprising the classical core@shell morphology and hollow cubes were reported up to now.

We can cite, first, two examples of very nice *PB@MOF core@shell nano-objects* designed for biomedical applications.[249], [250] In both of them, MOFs shell contains a porphyrin derivative, TCPP = tetrakis (4-carboxy-phenyl) porphyrin, either incorporated in the MOF network defects or acting as a ligand to build the MOF shell, which acts as a photosensitizer for photodynamic therapy (PDT). In the first case, the porphyrin-doped shell of Zr-based UIO66-TCPP MOF of around 20 nm was grown directly on the surface of PB cubes of 260 nm giving cubic nano-objects of around 300 nm following a synthetic strategy shown in Figure 19a. [249] The PB core and the MOF shell are clearly visible on the TEM picture (Figure 19b) and the atomic distribution performed by EDS mapping evidences the homogeneous distribution of the Zr atoms on the surface of the PB cubes. Similarly, a Zr-TCPP MOF shell was grown on the surface of the PB cubes of 110 nm. Depending on the synthetic conditions, the shell thickness was controlled to give objects with the whole size up to 140 nm. In this case, TEM and EDS coupled TEM analyses permit to conclude about the presence of the MOF shell on the PB cube surface. [250] In both cases, the association of PB with porphyrin containing MOF shell has permitted not only to enhance the PDT effect, but also to combine it with the PB's PTT action, giving rise to a synergistic PDT/PTT phenomenon highly useful for an antibacterial treatment against *Staphylococcus aureus* or *Escherichia coli* bacteria in wound infection treatment[249] or in multimodal image-guided therapy of cancer. [250]

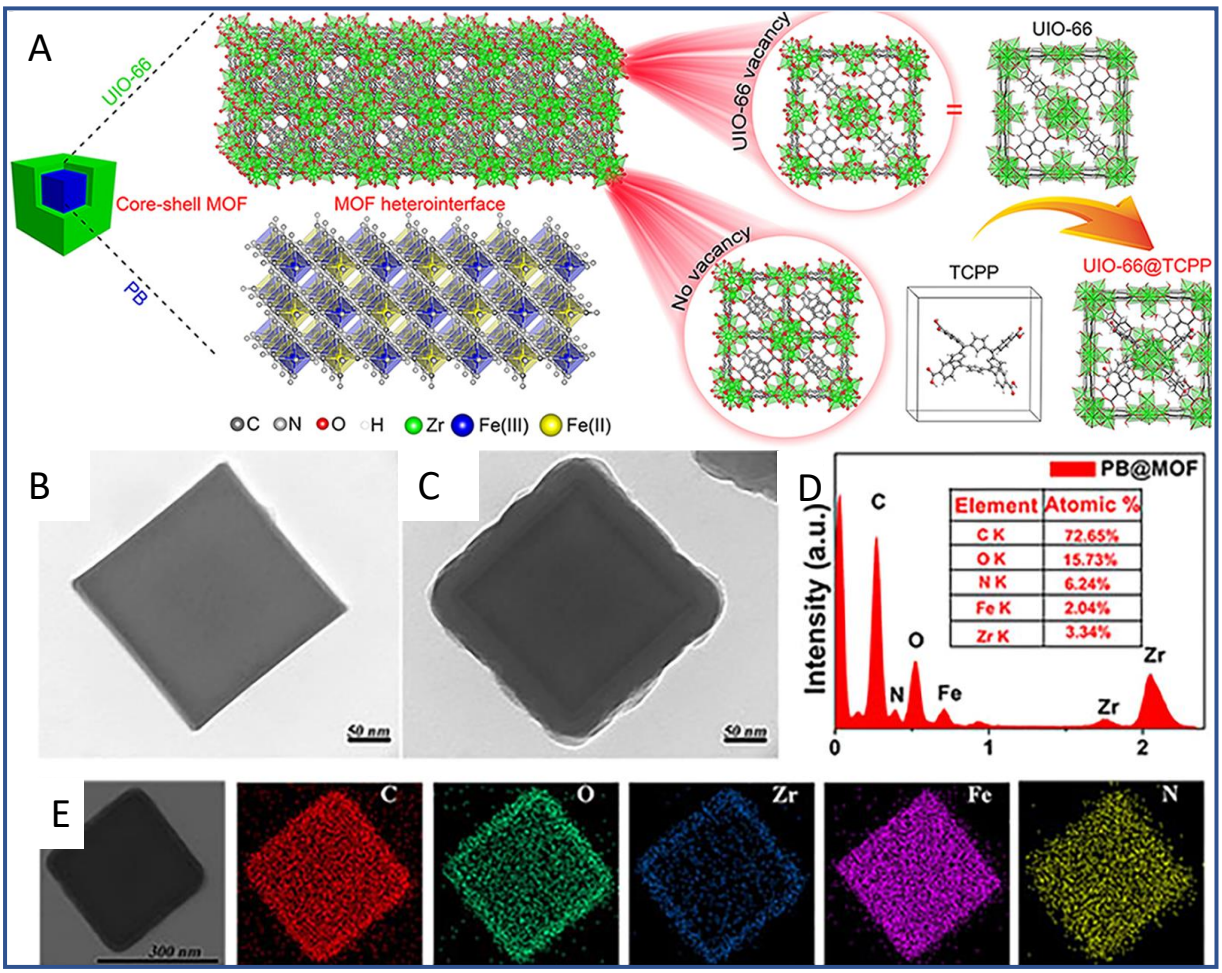

Figure 19. Schematic illustration of the PB@UIO66-TCPP MOF core@shell nano-objects (a); TEM pictures of the pristine PB nanoparticles (b) and PB@UIO66-TCPP MOF core@shell nano-objects (c), scale bar = 50 nm; TEM-EDX of PB@UIO66-TCPP MOF core@shell nano-objects (d); EDX elemental mapping images of PB@UIO66-TCPP MOF core@shell nano-objects (e). Reprinted with permission from Y. Luo, J. Li, X. Liu, L. Tan, Z. Cui, X. Feng, X. Yang, Y. Liang, Z. Li, S. Zhu, Y. Zheng, K.W.K. Yeung, C. Yang, X. Wang, S. Wu, ACS Central Science, 5 (2019) 1591-1601. Copyright 2021 American Chemical Society. [249]

The third example concerns Mn-PBA@POM hollow cubes obtained by an original approach consisting first in the synthesis of cubic $Mn_3[Fe(CN)_6]_2$ nanoparticles followed by their hydrothermal reaction with a strong Bronsted acid $H_3PMo_{12}O_{40}$ under heating at 100 °C, providing the etching of the PBA cubes with simultaneous formation of open heterostructures with a hollow interior (Figure 20). [251] Even if the SEM and TEM images show relatively homogeneous cubic cage-like structures with holes in the centres and the EDS mapping indicates a homogeneous distribution of the constituted Mn, Fe, P and Mo atoms in the cubes, it is, however, difficult to determine the mutual position and the relative shapes of the PBA and POM components. This unusual hollow morphology opens promising perspectives in the field of electrocatalysis for the oxygen evolution reaction (OER). Indeed, these heterostructures present more activities, stronger charge transfer, stronger catalytic stability and excellent catalytic performance in comparison with the single related materials.

Finally, we can also mention ZIF67@Co-PBA structures used as an intermediate in the synthesis of Co-PBA@CoS_2 nanoboxes (See section III.1.2). [236]

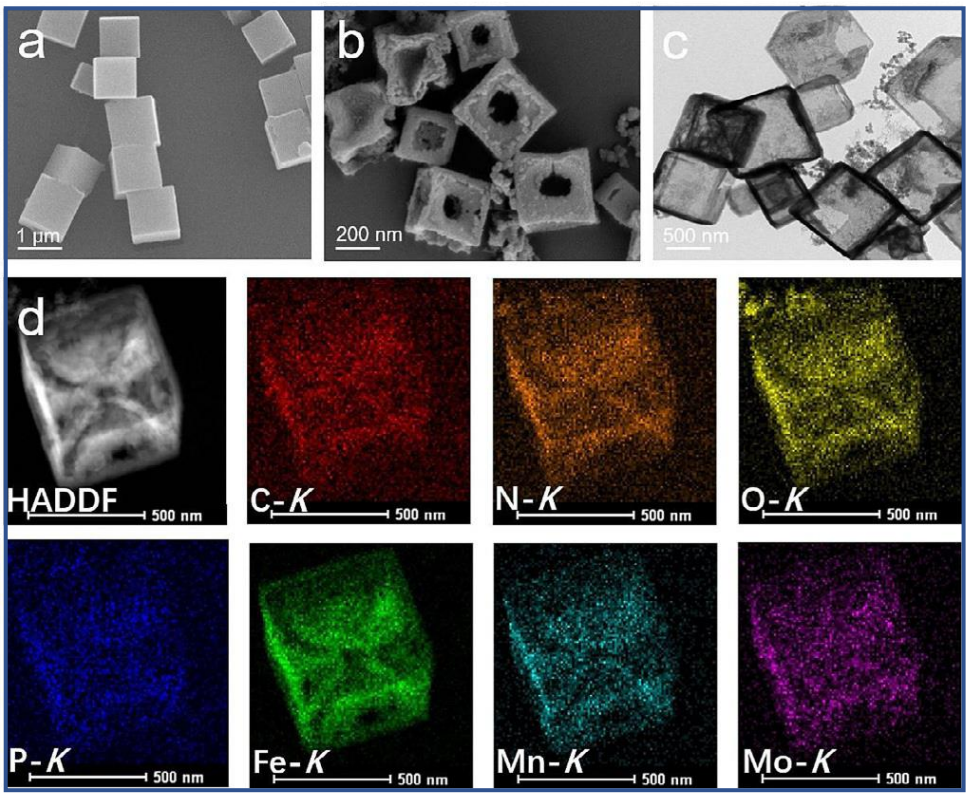

Figure 20. SEM images of pristine $Mn_3[Fe(CN)_6]_2$ PBA (a) and related $Mn_3[Fe(CN)_6]_2$@POM hollow cubes (b); (c) TEM image and (d) elemental mappings of $Mn_3[Fe(CN)_6]_2$@POM prooving the homogeneous distribution of the different elements in the nanoparticles. Reproduced from Ref. [236] with permission from the Royal Society of Chemistry.

II.5. Silica@PB or PB@Silica(A)s nanoheterostructures

The attractiveness of silica nanoparticles as a component of inorganic nanoheterostructures is linked first with their tailorable porous structure, high specific surface area and large pore volume. For this reason, they present unique advantages to encapsulate a variety of functional molecules, nanoparticles, complexes, and deliver them to the desired location. Secondly, the chemistry of porous nanosized silica is very well developed, and its fabrication is simple, scalable, and well manageable. Thus, the size and shape of porous nanoparticles, the thickness of porous shells, the size and volume of the pore may be precisely controlled through the modification of the sol-gel methodology. Moreover, the well-known surface chemistry of porous silica provides a variety of methods allowing the anchoring of different coating agents, ligands, molecules, antibodies, and others to the silica surface. Thirdly, nano-sized silica presents a relatively low toxicity and biocompatibility. For these reasons, porous silica nano-objects were widely developed as efficient nano-carriers for drug delivery with a promising expectation to overcome some of the problems of current nanoformulations. On the other hand, they have largely been investigated in association with other inorganic nanoparticles with the aim to design multifunctional nanomedicine for theragnostic. Hence, besides the drug delivery

feature, they can encapsulate and/or anchor inside the pores and on the surface different molecules, complexes or nanoparticles acting as imaging probes or therapeutic agents. Several reviews report on nano-heterostructures of quantum dots,[12] gold and silver nanoparticles,[252] magnetic nanoparticles[253] combined with silica in nano-objects of different topologies.

A relatively small number of articles were devoted to the combination of silica with PB(A)s. The reported nanoheterostructures examples in the literature, may be classified following two main morphologies: *PB(A) core@silica shell* and *silica core@PB(A) satellites nano-objects* (Figure 21). On one hand, these structures benefit from physical properties of PB-type nano-objects, such as longitudinal relaxivity, magnetic properties, photothermal activity, photoacoustic signal. On the other hand, the presence of porous silica endows them a controllable porosity necessary for efficient drug loading and drug delivery, easy functionalizable surface and biocompatibility. Therefore, the effect of the properties' combination leads to an appearance of multifunctionality required for designing multimodal therapeutic agents guided by different types of imaging or improved properties through synergic effects. Indeed, in several nanoheterostructures an improved longitudinal relaxivity, stability, biocompatibility or possibility to control/trigger the drug delivery by PTT were reported.

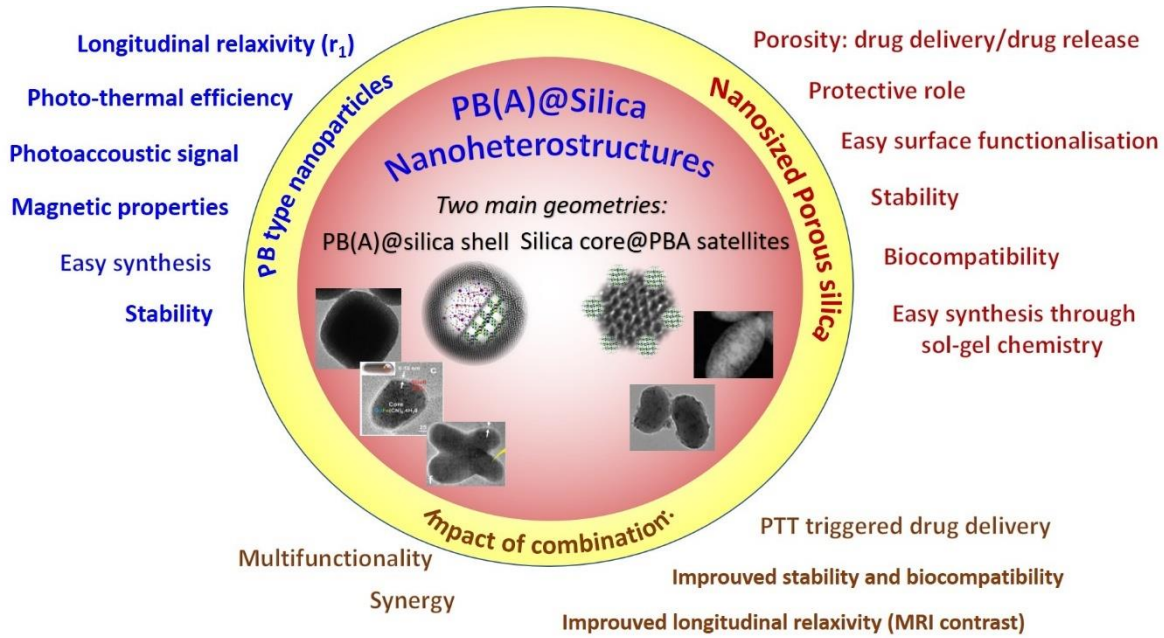

Figure 21. Main morphologies of PB(A)s@Silica nanoheterostructures and their advantages.

The design of *PB(A)s core@silica shell nano-objects* are usually made by using a two-step procedure consisting first in the synthesis of pristine coordination polymer nanoparticles by the usual self-assembly of cyanometallate and metal salts precursors' reaction and then by using a classical sol-gel process to form a homogenous porous silica shell on the surface. To this purpose, five examples of PB(A) core@silica shell nanoparticles with different core composition, including $Mn_3[Co(CN)_6]_2$, [254] PB, [255], [256], [257] [258] and Gd $[Fe(CN)_6].4H_2O$ [259] with different core geometries were reported. The employed sol-gel methods and conditions are summarized in Figure 22. First, a sol-gel procedure including the addition to a suspension of PB(A) nanoparticles of cetyltrimethylammonium bromide (CTAB)

as the surfactant, then tetraethyl orthosilicate (TEOS) in ammoniacal media to form MCM41-type mesoporous silica shells. In the case of PB@SiO_2, the nanocubes of 82 nm have been coated by the 34 nm mesoporous silica shell with a narrow pore size of 3 - 4 nm. [255] Similarly, a dendrimer-like silica shell with functional NH_2 groups around the PB nanocubes has been formed by the addition of TEOS and APTES in an ammoniacal media in the presence of CTAB. [258] A modification of this procedure consisting in the addition of a supplementary precursor, bis(triethoxysily)propane tetrasulfide (TESPTS), leads to the formation of a periodic mesoporous organosilica (PMO) shell of 17 nm having uniform mesopores of about 3.2 nm, surrounding the PB core of 125 nm (Figure 23). Note that the covalent anchoring of a fluorescent dye Cy5.5-maleimide was possible thanks to the thioethers groups situated in the pores.[256] These examples reported the formation of the silica or PMO shells under ammoniacal media (pH>7), which is not ideal for the PB(A)s stability and sometimes the surface of the PB(A)s nanoparticles may be etched. In this respect, a very simple method to form the silica shell around the PB nanoparticles in acidic conditions and encapsulate inside the fluorescent species has been reported by B. Zhao and coll. [257] In this case, a silica shell of around 18 nm comprising EuW_{10} has been formed around the cubic PB nanoparticles of 152 nm by the simple addition of TEOS in the presence of isopropanol, water and EuW_{10}. On the other hand, in the case of $Gd[Fe(CN)_6]\cdot 4H_2O$@SiO_2 nanoparticles, due to the very high sensibility of the latter to basic pH, inducing the formation of $Gd(OH)_3$, the nanoparticles were coated with a thin silica layer at neutral pH by adding (3-cyanopropyl)trimethoxysilane (CPTMS), tetramethyl orthosilicate (TMOS) and in the presence of a functional mimics of the protein silicatein α, triethylamine (TEA) as the catalyst. [259] In that case, the formation of an amorphous, non-porous shell of around 10 – 12 nm was noted. In all cases, a well-formed silica shell was formed on the surface of PB(A) nanoparticles, as attested by the TEM images shown in Figure 23.

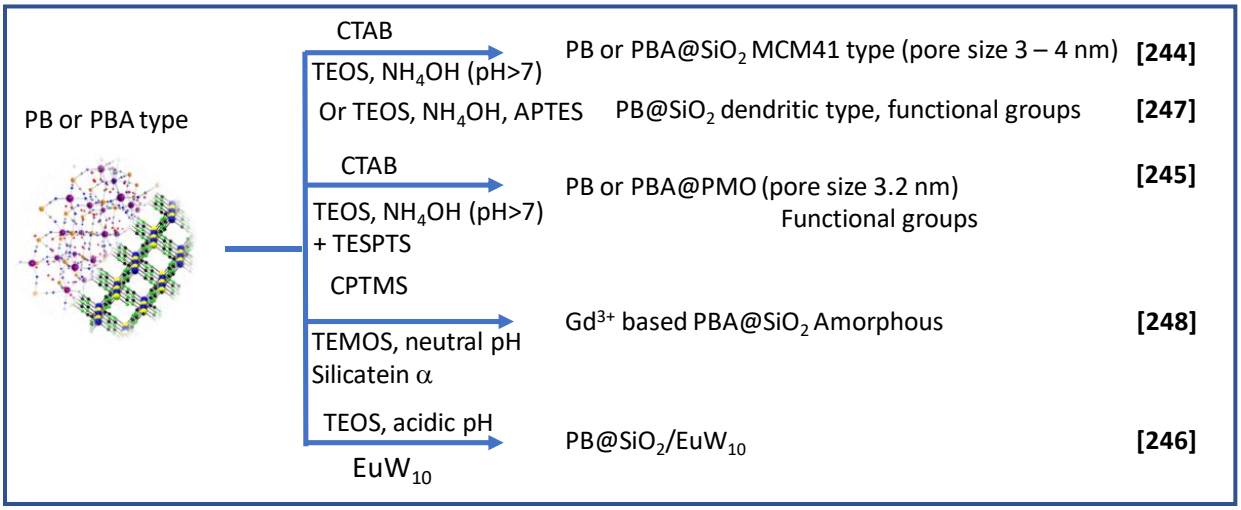

Figure 22. Four synthetic approaches used for the synthesis of PB(A)s core@silica shell nano-objects.

Two works were devoted to the design of silica nanoparticles decorated with PB(A) satellites by first, the synthesis of the functionalized mesoporous silica nanoparticles and then their decoration with small PB(A) nanoparticles. [260], [261] In the first work, ovoid-type mesoporous silica nano-objects of 50x100 nm functionalized with free NH_2 groups on the

surface with a pore size of 1.7 nm and having bi-photonic fluorescent dye molecules in the silica walls were decorated by $Ni^{2+}/[Fe(CN)_6]^{3-}$ nanoparticles of a few nanometers by a step-by-step coordination strategy of the precursors to the silica surface. [260] The TEM and HRTEM images of these nano-objects may be found in Figure 23d. This leads to the nanoparticles presenting transverse relaxivity linked to the presence of PBA and biphotonic fluorescence due to the organic dye. The second example reports on the design of kidney-like shaped silica nano-objects of 150 - 200 nm with a pore size of 2 – 3 nm containing the anticancer drug doxorubicin decorated with PB flakes of 10 – 15 nm situated on the outer surface of the silica. [261] This strategy permitted to achieve nanomedicine for the photoacoustic imaging-guided chemo-photothermal therapy of cancer cells.

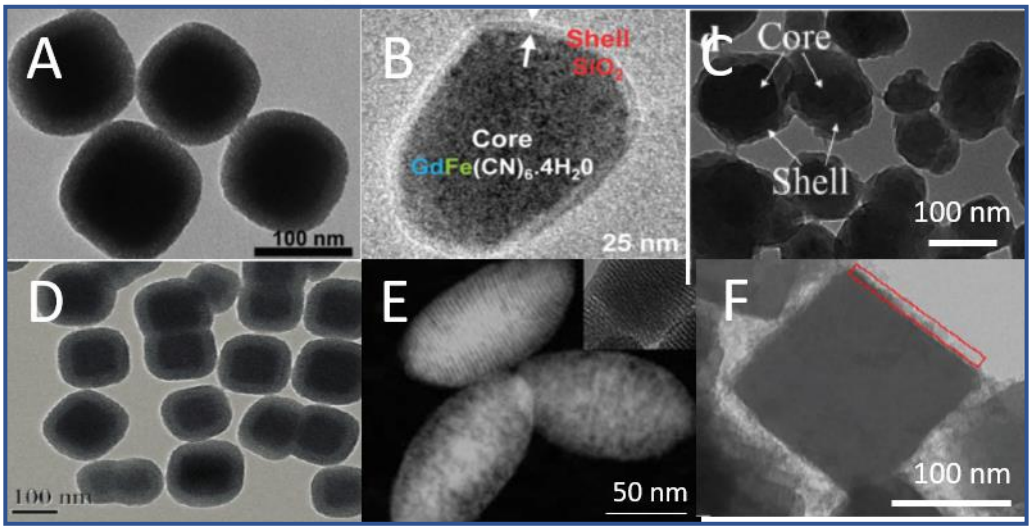

Figure 23. TEM images for: PB core@PMO silica shell nanocubes (A); $Gd[Fe(CN)_6].4H_2O@SiO_2$ shell nanorods (B); PB core@SiO_2/EuW_{10} shell (C) PB core@SiO_2 shell (D); SiO_2 core@$Ni_3[Fe(CN)_6]_2$ satellite nano-rices (E), porous PB core@ dendritic SiO_2 shell (F). Reproduced from Ref. [258] [259] [260] [261] with permission from the Royal Society of Chemistry. Reprinted with permission from W. Li, Z. Liu, B. Zhao, J. Liu, Langmuir, 36 (2020) 4194-4200. Copyright 2021 American Chemical Society. [257]

II.6 Carbon nanomaterials@PB(A)s nanoheterostructures

Carbon nanomaterials (CNM) were combined with PB(A)s mainly by using electrodeposition techniques, which are not the subject of this overview. [262] Nevertheless, a chemical way towards the design of discrete nanoheterostructures combining PB(A)s with multi-walled carbon nanotubes (MWCNTs), [263], [264], [265], [266], [267], [268] carbon spheres (Csp), [269] carbon quantum dots (CQD) [265] or graphene quantum dots (GQD) [270] has also been explored. It leads to the synthesis of nanoheterostructures with three types of morphologies: *(i) CNM core@PB(A) core or PB(A)satellites*, [263], [264], [269], [265], [267], [268], [270] *(ii) PB core@CNM satellites*, [271] *and (iii) CNM@PB necklace*. [266] The interest for such materials is linked not only with promising physical properties of carbon materials, such as the electronic conductivity of MWCNTs [263], [264], [265], [267], [268], [266] and GCDs, [270] or the photoluminescence properties of CQDs, [271] but also with their high surface-to-volume ratio, strong adsorptive ability and chemical properties. Thus the combination of carbon

materials with PB(A)s allows to consider various applications, such as positive electrodes for supercapacitors, [265], [268] batteries, [266] sensors, [263], [264], [270] electrochemically-assisted adsorbents [267] or biomedical area (see section III.3.2). [271], [269]
In the design of CNM@PB(A)s nanoheterostructures, in order to improve the stability of colloidal suspensions, commercial MWCNTs purified by HNO_3 treatment,[263], [264] or functionalized with polyvinylpyrrolidone (PVP), [267], [268], [266] were used. Csp, [269] CQD[271] and GQD[270] were obtained by carbonization from different sources, such as sucrose, [272] α-D-glucose or citric acid. In one specific case of CNM@PB necklace nanoheterostructures design, the single precursor approach employing $Na_4[Fe(CN)_6]$ under acidic pH for the elaboration of PB cubes of several hundreds of nanometers in the presence of MWCNTs was employed. [266] In all other cases, whatever the discrete nanoheterostructure morphology obtained, the two precursors approach was used to synthesize PB from $FeCl_3$ and $K_4[Fe(CN)_6]$, [271] or $K_3[Fe(CN)_6]$[[263], [264], [269], [270] or design PBAs by assembling $NiCl_2$[269] or $CuCl_2$ [267], [268] with $K_3[Fe(CN)_6]$ [267], [268] or $K_3[Cr(CN)_6]$ [269] and $RuCl_3$ with $K_4[Ru(CN)_6]$. [265]

II.6.1. Carbon nanomaterials core@PB(A) shell or satellites nano-objects.

Most of the nanoheterostructures presenting CNM@PB(A) core@shell or satellites morphologies were elaborated using MWCNTs as a core. Three works report on the formation of a dense and almost uniform PB(A) coverage grown on the MWCNTs core leading to bicycle chain-like appearance. [263], [264], [267] The synthesis consists in the use of stable colloidal solutions of commercial MWCNTs obtained after purification with HNO_3[263], [264] or functionalization with PVP, [267] reacted with conventional precursors, $FeCl_3$[263], [264] or $CuCl_2$ [267] and $K_3[Fe(CN)_6]$ to afford PB or Cu-PBA shell or satellites. [264] Note that in these cases, MWCNTs are also considered as a reducing agent to generate Fe^{2+} ions from $FeCl_3$. [263]

Depending on the conditions and PBA nature, the PBA coverage on MWCT may be less uniform. This is the case of MWCNT@RuRu-PBA core@satellites, where the satellites were elaborated from $RuCl_3$ and $K_4[Ru(CN)_6]$ at pH = 2. [265] It should be remembered that the mild oxidation of ruthenium(III) to ruthenium-oxo species [273], [274] leads to the formation of Ru-O/Ru-CN ones. It is likely that rather inert graphitic structures of MWCNTs do not favour excessive precipitation of Ru-O/Ru-CN species on their surfaces, which could explain the relatively poor surface coverage. On the contrary, the growth of the Cu-PBA from $CuCl_2$ and $K_3[Fe(CN)_6]$ precursors (at pH = 4 with acetate buffer in an autoclave at 180 °C for 8 h) in the presence of pre-treated with PVP, MWCNTs leads to a very well-defined MWCNT core@PB shell morphology.[268] Further, the Cu-PBA shell thickness can be varied depending on the loading mass of Cu-PBA on MWCNTs to 10, 20 and 30 nm with a mass fraction of 25, 46 and 58 % Cu-PBA respectively.

Other carbon nanomaterials than MWCNTs, such as GQDs[270] and Csp [269] were also used as cores. Indeed, Csp core@PB or NiCr-PBA satellites were obtained in two-step approach consisting first in the preparation of Csp from the carbonization of α-D-glucose followed by addition of $FeCl_3$ and $K_3[Fe(CN)_6]$ or $NiCl_2$ and $K_3[Cr(CN)_6]$ precursors. These discrete

nanoheterostructures present a relatively poor core coverage with the PB(A) satellites. Note that these structures were further functionalized with benzene tricarboxylic acid allowing further lanthanide tagging using $Tb(NO_3)_3$ or $Sm(NO_3)_3$ to be used as multimodal imaging agents (see section III.3.2.2).

II.6.2. PB core@Carbon nanomaterials satellite shell nanoparticles.

Only one report deals with the formation of such discrete nanoheterostructures exhibiting a PB core@CQD satellites morphology. PB nanocubes of *ca*. 50 nm were classically obtained from mixing $FeCl_3$ and $K_4[Fe(CN)_6]$ in the presence of citric acid. [271] Then, the direct microwave-assisted carbonization of the capped citric acid on PB nanoparticles provides the formation of such nanoheterostructure. The CQDs were shown to possess a crystalline core and an amorphous carbonaceous surface making the nanoheterostructures photoluminescent in order to use them as theragnostic agents (see section III.3.2.1).

II.6.3. Carbon nanomaterials@PB necklace.

The last example to cite concerns an original necklace morphology of MWCNT@PB. [266] For this, commercial MWCNTs treated with HNO_3 and PVP were used for the growth of the PB in an autoclave from $Na_4[Fe(CN)_6]$ at pH = 1. The morphology may be described as the PB nanocubes linked through carbon nanotube chains conducting to a complex interpenetrate network (Figure 24). This latter exhibited 3D conductivity that was exploited to test such nanomaterial for subzero-temperature cathode for a sodium-ion battery (see section III.1.3).

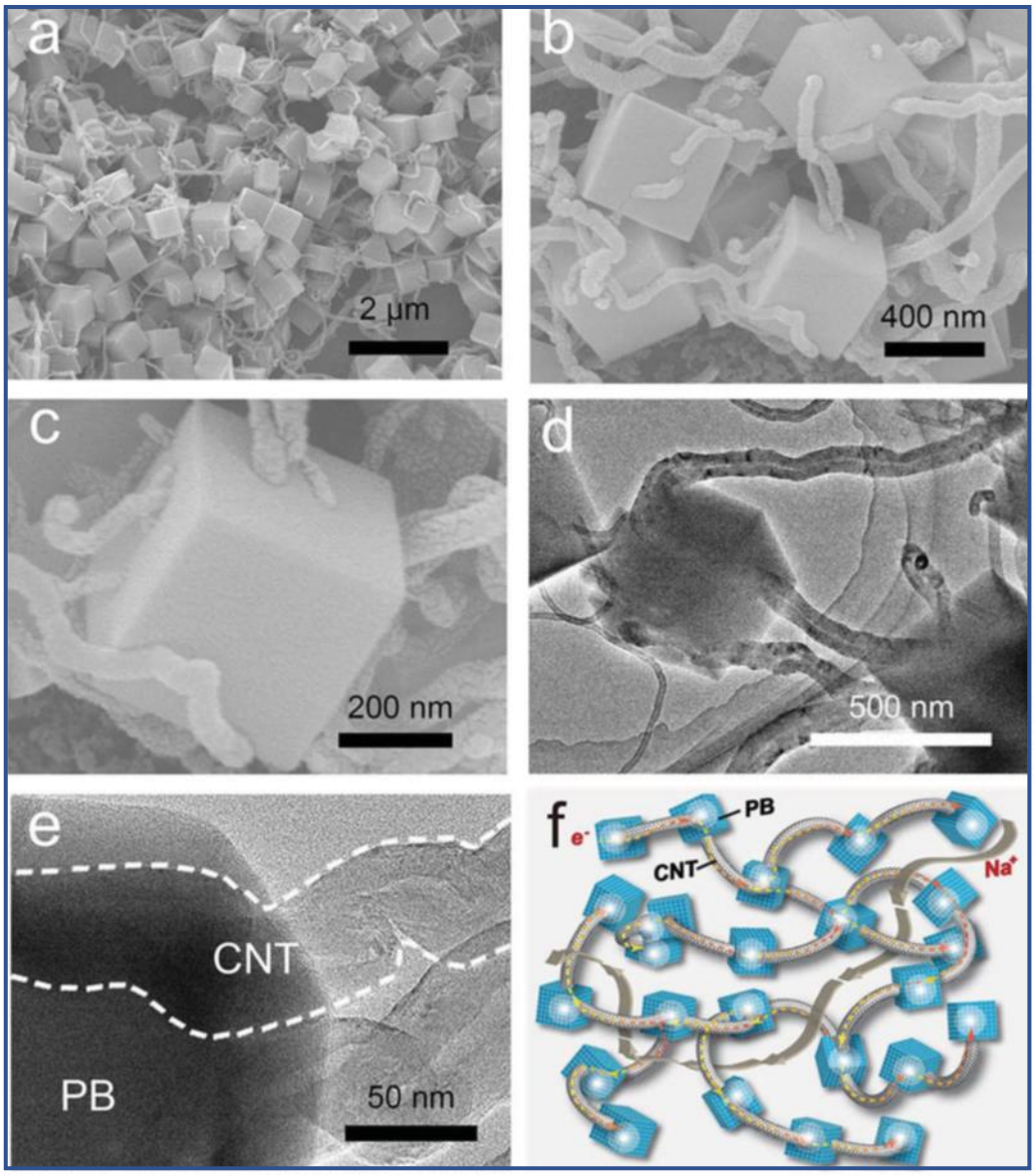

Figure 24. a–c) SEM, d–e) TEM images of the MWCNT@PB nanoheterostructures. f) Schematic illustration showing the mixed conducting necklace like network. Reprinted from Ref. [266] with permission from John Wiley and Sons.

III. Main properties & applications

The design of nanoheterostructures containing different inorganic materials at the nanoscale is mainly driven by the idea to combine their physico-chemical properties affording multifunctional materials. The properties of components may act separately or present synergistic effects. This last aspect is particularly important when considering the as-obtained nanoheterostructures for given applications. This section describes the main physical and chemical properties and related applications of the multifunctional PB(A)s based nanoheterostructures, making a particular emphasis on complementarity of properties or synergistic effect in different applicative domains, such as electrochemical devices for energy/generation/storage, electrochemical biosensors, and therapy and/or diagnostic agents to

which such nanomaterials are particularly relevant. Other applications related to catalysis, sorption, or microwave absorption are also mentioned at the end of this section.

III.1. Electrochemical devices for energy conversion/generation/storage

The exhaustion of fossil fuels and climate are two major problems facing our contemporary society to which renewable energy conversion and storage technologies can provide a clean and sustainable alternative. The design and development of advanced and affordable materials working on the principle of electrochemical energy conversion is the key to facilitate diverse energy conversion/generation/storage processes, such as electrocatalysis, water splitting, supercapacitor and battery. Different reports summarized in this subsection concerns the uses of hybrid nanoheterostructures with PB(A)s for their employment as nanomaterials for modified electrodes to build supercapacitor, electrocatalytic water splitting and battery devices.

III.1.1. Supercapacitors

Supercapacitors should present high specific capacitance (C_s), long life cycle, high power density (P_d), being almost maintenance-free, experiencing no memory effect, being safe and function as a bridge for a power-energy difference that exists between capacitor (high P_d) and fuel cells/batteries (large energy storage). Discrete nanoheterostructures combining PB[222] or ZnCo-PBA [223] and lamellar materials, such as MnO_2[222] or α-$Co(OH)_2$[223] affording "hairy" core@shell morphologies with PB(A)s as the core, or combining RuRu-PBA [265] or CuFe-PBA [268] with MWCNTs affording core@satellite [265] or core@shell morphologies [268] with MWCNTs as the core, were used as nanomaterials to build supercapacitor devices. Their capacitive behavior was characterized using cyclic voltammetry (CV) [268], [223], [222], [265] galvanostatic charge/discharge (GCD) tests [268], [223], [222], [265] and electrochemical impedance spectroscopy (EIS). [268], [222], [265] Further, two electrodes asymmetric [268], [223], [222] or symmetric capacitors [268] configuration were assembled to determine the energy density and power density. The supercapacitor performances and energy storage performances for those hybrid nanomaterials are given in Tables 4 and 5, respectively.

Table 4. Comparison of supercapacitor's performance for different nanoheterostructures involving PB(A)s.

Ref.	**Nanoheterostructure**	**Electrolyte solution**	**Current density/A g^{-1}**	**Specific capacitance/F g^{-1}**
[265]	MWCNT@RuRu-PBA	H_2SO_4	0.1	86
[268]	MWCNT@CuFe-PBA	KCl	1	989
[222]	PB@MnO_2	KNO_3	1	608
[223]	ZnCo-PBA@α-$Co(OH)_2$	KOH	1	424

Table 5. Comparison of the energy storage performance for the different nanoheterostructures involving PB(A)s.

Ref.	Nanoheterostructure	Electrolyte solution	Energy density/Wh kg^{-1}	Power density/kW kg^{-1}
[265]	MWCNT@RuRu-PBA	H_2SO_4	2.9	1.14
[268]	MWCNT@CuFe-PBA	KCl	60.4	0.5
[222]	PB@MnO_2	KNO_3	13.6	2.72
[223]	ZnCo-PBA@α-$Co(OH)_2$	KOH	49.1	1.734

The capacitance retention of 74 % after 5000 cycles at 5 A g^{-1}, [223] 93 % after 4000 cycles at 5 A g^{-1}, [222] 93 % after 1000 cycles [265] and 90 % after 10000 cycles at 1 A g^{-1} [268] illustrates the good stability of the used nanomaterials (Tables 4 and 5). In most of these studies, the performances of the discrete hybrid nanoheterostructures were compared with the individual components of the latter, emphasizing the synergistic outcome of the combination leading to a great improvement of the capacitance performance of the hybrid nanoheterostructures. [222], [223] For example, compared to the calculated specific capacitance that should be expected resulting from the association of ZnCo-PBA and α-$Co(OH)_2$, the obtained experimental specific capacitance is 25% higher. [223] Such a synergistic effect can arise from different factors depending on the material coupled to PB(A)s. Supercapacitors can be divided into electrical double-layer capacitors (EDLCs) and pseudo-capacitors on the basis of the energy storage mechanism. Pseudo-capacitors can provide a huge specific capacitance, which far exceeds that of EDLC. Bare MWCNTs exhibit only pure double-layer capacitive behaviour, as expected for porous carbon materials, but when they are coupled with PBAs, the capacitance is mainly contributed by the faradic current of PBA layers. Thus, the PBA can supply huge specific capacitance as a pseudo-capacitor. However, PBAs exhibit very weak conductivity. This can be compensated by MWCNTs favouring the electron transfer at the metallic centers of PBAs. The observed synergistic effect is therefore the result of the combination of the electronic transfer from MWCNTs to PBAs and the contribution by the faradic current of PBAs. When lamellar metal oxide or hydroxide structures are combined with PBAs, the specific capacitance of the composite electrode is much larger than the sum of each part, and a synergy effect of the dual-layer structure named "interlayer concentration enhancement effect" was proposed to account for this excellent electrochemical performance. This effect can be explained as an additional ion concentration "reservoir" between the metal oxide or hydroxide and the PBA, as it was shown for the combination of NiFe-PBA and MnO_2. [275]

III.1.2. Oxygen evolution and hydrogen evolution reactions

Water splitting consists in breaking water chemical bonds to generate O_2 or H_2 (Figure 25), the latter being an energy carrier providing high energy densities relative to other storage technologies, such as Li^+-ion batteries. Splitting water electrochemically involves two half-cell reactions: water reduction to evolve hydrogen at the negative electrode and water oxidation to evolve oxygen at the positive electrode. The standard potential of the hydrogen electrode is 0 V *vs* reversible hydrogen electrode (RHE), and that of oxygen electrocatalysis is 1.23 V *vs* RHE at standard conditions (25 °C, 1 bar H_2 or O_2 pressure) and, *e.g.*, 1.168 V *vs* RHE at 80 °C, where devices are often operated. Above these equilibrium potentials, half-cell oxidation,

oxygen evolution reaction (OER) is favoured thermodynamically, and below which, half-cell reduction, hydrogen evolution reaction (HER) is preferred thermodynamically. [276]

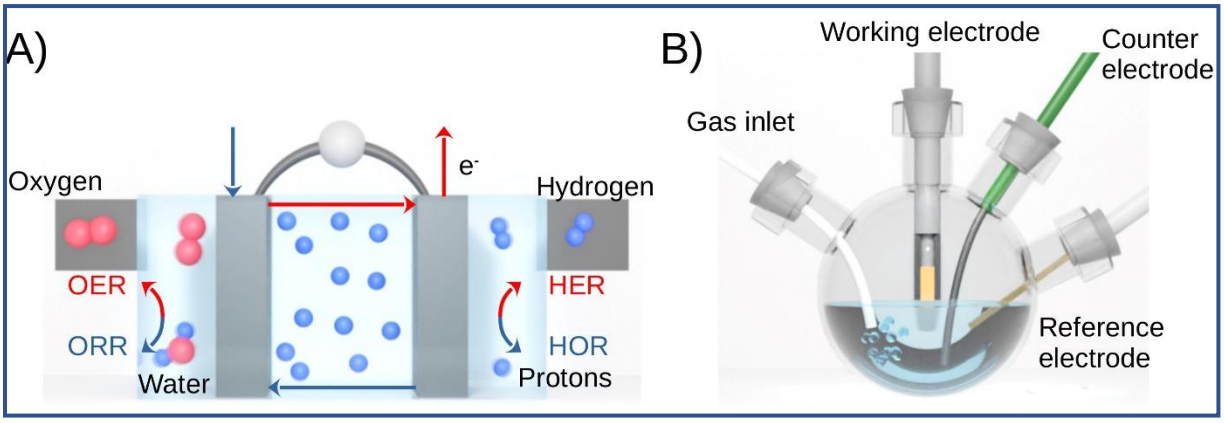

Figure 25. a) Schematic of a two-electrode fuel cell or water electrolyser. b) Schematic representation of a three-electrode electrochemical cell with working electrode, reference electrode, counter electrode, and gas inlet.

Catalysts are needed to increase the kinetics of these reactions to meet practical demand for higher system efficiency and lower energy loss in the whole cycle.The attention on PBAs for such purpose was concentrated on their open-framework structure, as well as their varied composition. [277] More specifically, their critical advantage over conventional OER catalyst such as for instance IrO_2 or RuO_2 is the tunable sizes of the interstitial sites to accommodate charges of different sizes. And more importantly, some of them present excellent OER inertness and high upper potential limits. [278] It can also be mentionned that they can be converted into many other interesting compounds relevant for such application. [279] However, despite much progress has been made, there are very few PBAs and their derived materials that combine the advantages of all performance indicators such as facile preparation, low-cost, excellent electrochemical performance including tow overpotential, hich catalytic current density, and high stability. [280] In connection with the search for alternative solutions to these limitations, several discrete nanoheterostructures combining PBAs, such as MnFe-PBA, [251] CoFe-PBA, [195], [236], [281] or NiFe-PBA [195], [196], [281] with other inorganic materials for instance gold, [281] platinum, [195], [196] CoS_2 [236] or POM [251] were developed to afford such active electrocatalysts for OER [236] [195] [251] or HER. [196] Table 6 summarizes the OER activities reported for those hybrid nanoheterostructures as electrocatalysts.

Table 6. Comparison of OER activities for the reported hybrid nanoheterostructures involving PB(A)s.* under visible light

Ref.	**Nanoheterostructure**	**Electrolyte**	**Overpotential@10 mA.cm^{-2}/mV**	**Tafel slope/mV dec^{-1}**
[195]	CoFe-PBA@Pt	1.0 M KOH	300	68
[196]	NiFe-PBA@Pt	1.0 M KOH	320	37
[251]	MnFe-PBA@POM	1.0 M KOH	440	23.45

[236]	CoFe-PBA/CoS_2	1.0 M KOH	301	79.6
[236]	CoFe-PBA/CoS_2	1.0 M KOH	265*	59.2*
[281]	Au@NiFe-PBA	1.0 M KOH	327	89
[281]	Au@CoFe-PBA	1.0 M KOH	306	63

In all these publications, the OER activities were systematically found improved compared to the ones of the individual components. In particular, in CoFe-PBA@Pt nanoheterostructures, Co(II) ions serves as active sites for catalytic reactions, indicating that the Co(III)/Co(II) couple in CoFe-PBA is crucial for the OER performance. The reasons for the boosting effects of Pt in these nanoheterostructures have been summarized as: (*i*) tunning of the active centres of Co to a higher oxidation state, which is favourable for OER activity, (*ii*) ensuring the constant oxidation reaction of Co(II)-to-Co(III) maintaining the catalytic stability, (*iii*) introducing more active sites for improved OER performance, and (*iv*) accelerating charge transfer to enhance reaction kinetics. [195] Endowed with the combined benefits, the designed CoFe-PBA@Pt catalyst exhibits significantly improved OER activity and stability than the pristine CoFe-PBA. The OER performances of NiFe-PBA@Pt were also carried out and a similar effect of loaded Pt on the OER activity was observed. [195]

Studies performed on MnFe-PBA@POM also demonstrate advantages of such combination in the OER in comparison with the OER activity of only MnFe-PBA, which include more active sites, stronger charge transfer and stronger catalytic stability. [251] CoFe-PBA/CoS_2 on its own combine the intrinsic electrocatalytic activity of the transition metal dichalcogenide CoS_2 for the OER and the sunlight response of the transition metal dichalcogenide CoS_2 and the CoFe-PBA. Consequently, the porous framework, engineered surface defects and abundant oxygen vacancies endow them with enhanced electrocatalytic performance toward OER due to the enlarged electrolyte-accessible surface, high structural integrity and abundant electron and mass transfer routes. Moreover, they could also enable photo-assisted oxidation reactions with a significantly high current density and a low overpotential. Mechanistic investigations reveal that the OER improvement can mainly be ascribed to the combination of photo-driven and electricity-driven water oxidation reaction, where the photogenerated electron transfer from CoFe-PBA to CoS_2 results in photogenerated holes in CoFe-PBA that are more beneficial for the oxidation of H_2O, as well as affording decreased activation energy of CoS_2 for the OER.[236]

It was found that the introduction of small amounts of Au (5–10% in weight) in the Au@PBA structure gives rise to a reduction of the overpotentials at 10 mA cm−2 up to 100 mV and an increase up to 420% of the current density recorded at an overpotential of 350 mV. [281] These voltage decreases are higher than the ones using reduced graphene oxide. Additionally, the Tafel slope remains unaffected, indicating that Au reduces the limiting potential of the catalyst with no variation in the kinetics of the reaction. An important increase in the electroactive mass capable of being reduced or oxidized was detected by means of coulovoltammetry, thus providing a higher concentration of electroactive sites to participate in the OER. This feature in

combination with the enhanced intrinsic activity of PBA and the higher conductivity of the hybrid was proposed to be responsible for the improvements in both the electrocatalytic activity and the electrochemical stability.

NiFe-PBA@Pt discrete nanoheterostructures were also used as electrocatalysts for the HER. [196] In that case too, the enhanced HER activity of Pt due to the NiFe-PBA and Pt interface was demonstrated (Figure 26). The Ni species of $Ni_3[Fe(CN)_6]_2$ were shown to play key roles in contributing to the water dissociation and improving the HER kinetics, as well as helping to maintain the catalytic activity of Pt during a long-term durability test in both, acidic and alkaline media. As a result, the new NiFe-PBA@Pt hybrid catalyst exhibits a superior catalytic property for HERs in both sulfuric acid (H_2SO_4) and potassium hydroxide with a Pt loading of 4.0 %. A low overpotential of 59 mV was achieved at a current density of 10 mA cm^{-2} in H_2SO_4 and a high mass current density of 3.75 mA μg Pt^{-1} was obtained at an overpotential of 70 mV, which outperforms reported Pt-based catalysts in acid electrolytes.

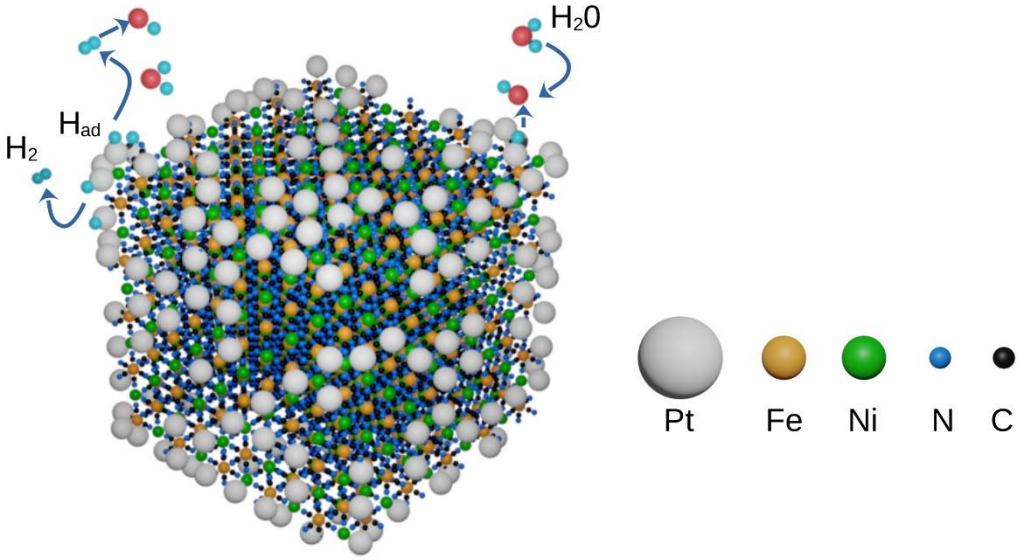

Figure 26. Schematic diagram of HER at the active interface of ultrafine Pt and a $Ni_3[Fe(CN)_6]_2$ nanocube, including the Volmer step of water dissociation on the Ni^{2+} species and the formation of Pt–H_{ad} intermediates at the boundary between the Ni and Pt domains, the Heyrovsky reaction of Pt–H_{ad} with another water molecule, as well as the Tafel recombination reaction of two H_{ad} atoms.

III.1.3. Batteries

Sodium-ion batteries are considered as a low-cost complement or competitor to Li^+-ion batteries for large-scale electric energy storage applications; however, their development has been less successful due to the lack of suitable host materials to enable reversible Na^+ insertion reactions. PB(A)s appear as attractive candidates for Na^+-ion batteries cathodes because of their open channel structure, compositional and electrochemical tunability (see Section I). Even though numerous examples of PB(A)s were considered for this purpose, [124], [282], [283] only one example was reported regarding the use of a discrete nanoheterostructure combining PB and MWCNTs in a necklace configuration (see section II.6.3). [266] Due to the fast ionic/electronic transport kinetics even at an extremely low temperature of −25 °C, the MWCNTs/PB nanohybrids show outstanding low-temperature performance in terms of specific energy

density, high-rate capability, and long cycle life. After 1000 cycles at 2.4 °C, the retention capacity at 0 and −25 °C could reach as high as 81 % and 86 % of the initial values, respectively, which represent the best performance reported at such low temperatures. Indeed, the MWCNT network facilitates the low-temperature electrochemical reaction by providing anchored PB nanoparticles access to the liquid electrolyte and excellent electric contact with the current collector. A density functional theory (DFT) modelisation of the Na^+ diffusion within the PB particles suggests that cooperative Na^+ conduction lowers the activation energy for Na^+ transport within the PB particles emphasizing the interest of the as-prepared nanoheterostructure. Another interesting example related to sodium ion batteries was reported with discrete PB nanoparticles coated with PDA displaying a cubic morphology with a coarse surface and a particle size ranging from 60 to 80 nm. [284] The as-obtained cathode electrode made of PB@PDA delivers a reversible capacity of 93.8 mA h g^{-1} after 500 cycles at 0.2 A.g^{-1}, and a discharge capacity of 72.6 mA h g^{-1} at 5.0 A g^{-1}. Both experiments and computational simulations demonstrated that the Fe^{II} sites in PB prefer to couple with the robuts PDA layer to stabilize the PB structure. Moreover, the Na migration in the PB structure is enhanced after PDA coating, thus improving the sodium storage capacity.

III.2 Electrochemical Biosensors

As a working principle, an electrochemical biosensor should effectively sense and convert the chemical signal into an electrochemical one. According to the IUPAC, it can be defined as "a self-contained integrated device, which is capable of providing specific quantitative or semiquantitative analytic information" using a biological recognition element coupled to a signal transduction section. [285] The goal of a biosensor is to provide real-time responses with high sensitivity and selectivity with only minimal perturbation of its surrounding matrix. [286] Briefly, in general, and whatever their chemical composition, biosensors can be classified as: (*i*) immunosensors based on antibodies having high affinity to antigens, (*ii*) enzyme-sensors used to achieve low limits of detection due to the high catalytic activity and specific binding capabilities of enzymes, (*iii*) gene- or DNA-biosensors based on hybridization of nucleic acids (DNA or RNA), (*iv*) aptasensors employing aptamers (single-stranded DNA or RNA molecules) able to bind target molecules with high affinity and specificity as recognition element, and (*v*) microbial sensors using microorganism (*e.g.*, fungi and bacteria) immobilized onto the transducers, the operational principle of the latter being analogous to that of enzyme biosensors.

One of the most difficult issues in an electrochemical biosensor, which usually limits the overall performance of bioelectrodes, is the efficient wiring between the active centre of the bioreceptor and the electrode surface. One way to overcome this difficulty is to incorporate electron-transfer mediators on the surface of the bioelectrodes. Electron-transfer mediators are usually redox compounds of natural or artificial origin able to interact with the biological recognition component with a rapid electron communication between the biomolecule and the surface of the electrode. In this field, PB(A)s are undisputedly regarded as one of the most representative electron-transfer mediators for enzymatic biosensors due to their excellent properties as a transducer platform for H_2O_2 quantification. Additionally, the research community has also focused on exploring the nanostructures derived from PB(A)s because of significant changes in

their physicochemical properties and improved electrochemical performance. [119] In the following subsections, we will consider various biosensors based on hybrid nanostructures involving PB in immuno- and aptasensors and as artificial enzymes for low limits detection molecules, including H_2O_2.

III.2.1. Immuno- and aptasensors

Several electrochemical immunosensors or aptasensors based on discrete nanomaterials including PB as one of the components combined with gold, [201], [202], [287], [288], [289] platinum, [193] cerium [220] or iron oxides [207] were developed since 2008. These nanoheterostructures have been designed, either as a part of modified gold [207], [193] or glassy carbon [201], [202], [289], [220] working electrodes in classical three-electrode devices, or as a part of a graphite working electrode in a screen-printed carbon electrode, [287] or as a modified electrode for conductometric measurements. [288] Several of these studies use a sandwich immunoassay method employing two antibodies [201], [287], [207] binding to different sites on antigens or ligands. The working principle consists in: (*i*) an anchoring of a highly specific for the antigen "capture antibody" to a solid surface; (*ii*) an addition of an antigen followed by the addition of a second "detection antibody", which will bind the antigen at a different epitope than the capture antibody. As a result, the antigen is 'sandwiched' between the two antibodies.

A similar approach using aptamers instead of antibodies has been settled in the case of aptasensors. [202] PB-containing discrete nanoheterostructure-based immuno- or aptasensors were then developed for the detection of α-fetoprotein (AFP), [193], [207] tissue polypeptide antigen (TPA), [287], [288] prostate-specific antigen (PSA) and free prostate-specific antigen (fPSA), [201] carcinoembryonic antigen (CEA), [207] human scavenger receptor B type CD36 or T4 polynucleotide kinase (PNK) [289] and platelet-derived growth factor B-chain (PDGF-BB), [202] respectively.

Among these, we would like to emphasise a novel signal-amplification strategy for the development of an advanced electrochemical immunoassay by using the redox-activity of PB@Au hybrid nanostructures as the labels and horse radish peroxidase (HRP) -mediated formation of tyramine-HRP repeats for signal amplification, which represents a nice example for detection of tissue polypeptide antigen (TPA) (Figure 27). [287] The as-synthesized PB@Au were used to label HRP and pAb2 antibody detection through a covalent conjugation between the doped gold nanoparticles and thiols or alkylamines functionalities of the proteins. The electrochemical immunosensor was fabricated on a screen-printed carbon electrode (SPCE), which included a 2 mm graphite working electrode, an Ag/AgCl reference electrode and a graphite auxiliary electrode. Initially, bovin serum albumin (BSA) aqueous solution was thrown on a cleaned graphite working electrode. Afterwards, the mixture of EDC/NHS was dropped on the BSA-modified surface and incubated. Then, mAb1 antibody capture was deposited on the surface and incubated (Figure 27, up). Compared with the previously published works with the sandwich-type immunoassay format, [290], [291] highlights of this study lie in: *(i)* decreasing the background signal and enhancing the current response of the electrochemical immunoassay, and *(ii)* combining the advantages of nano and enzyme labels with electroactive indicator together, thus avoiding the participation of additional electron mediators.

Interestingly, the same PB@Au hybrid nanostructures were used for the same purpose but based on conductometric measurements. [288]

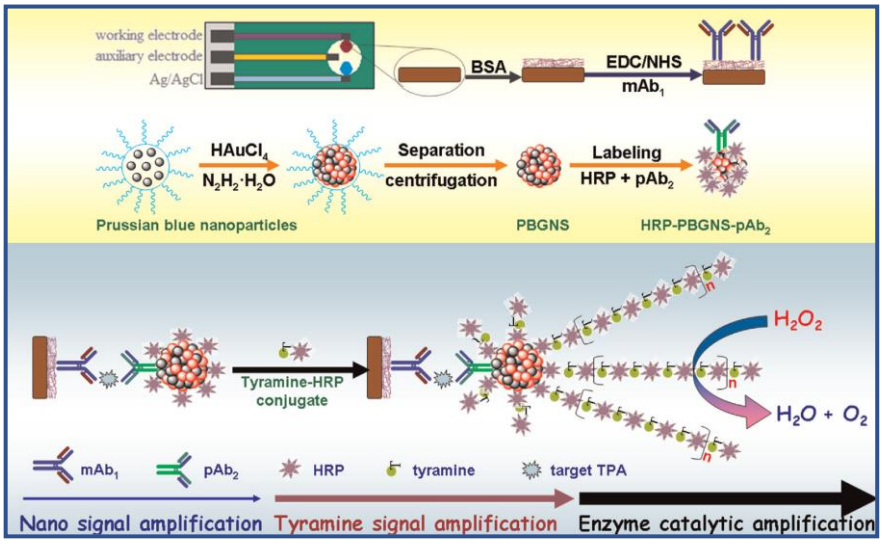

Figure 27. Schematic illustration of enzyme-triggered tyramine-HRP repeats on PB@Au nanostructures for highly sensitive electrochemical immunoassay of tissue polypeptide antigen (TPA) on mAb1-functionalized screen-printed carbon electrode with a sandwich-type detection mode. Reproduced from Ref.[287] with permission from Elsevier.

Another example to illustrate this application concerns PB@Au and NiFe-PBA@Au nanoheterostructures for the simultaneous electrochemical immunoassay of fPSA and PSA. [201] This test includes gold nanoparticles(AuNPs)/polyethyleneimine(PEI)-3,4,9,10-perylenetetetracarboxylicdianhydride (PTCA) as a sensing interface for noise reduction and PB@Au and NiFe-PBA@Au on onion-like mesoporous graphene sheet (O-GS) nanohybrids as signal tags to label the different detection antibodies (Ab_2) for signal amplification. The prepared PB@Au/O-GS and NiFe-PBA@Au /O-GS possessed favorable catalysis activity and bioactivity to accelerate the electron transfer rate and enhanced the immobilization amount of detection antibodies (Ab_2) and biotinylated alkaline phosphatase (bio-AP), thus amplifying the detection responses. Experimental results showed that the proposed immunosensor enabled simultaneous monitoring of fPSA and PSA in a single run thanks to the different electrochemical responses of PB and NiFe-PBA. The convenient operation and sensitivity of this method provide a promising potential in clinical diagnosis and represent a nice example of how to play with PB(A)s discrete nanoheterostructures when the accurate quantitative analysis of multiple tumour markers is desired.

Similar procedure for sandwich-type immunoreactions was performed for the detection of carcinoembryonic antigen (CEA) and α-fetoprotein (AFP) as model systems with Fe_3O_4@PB nanoheterostructures decorated with gold nano-satellites as labelled tags. [207] The authors demonstrate an amplification strategy based on the feasibility of bioenzyme, HRP and glucose oxidase (GOD), functionalized Fe_3O_4@PB/Au nanoparticles, which exhibit attractive redox electrochemical and enzyme catalysis activities, when the modified electrode was detected in the working buffer containing proper amounts of glucose for an ultrasensitive and reproducible electrochemical immunosensing fabrication (Figure 28). In that case, the magnetic iron oxide

component allows separation of the immunocomplex using an external magnetic field, permitting the immunosensor regeneration.

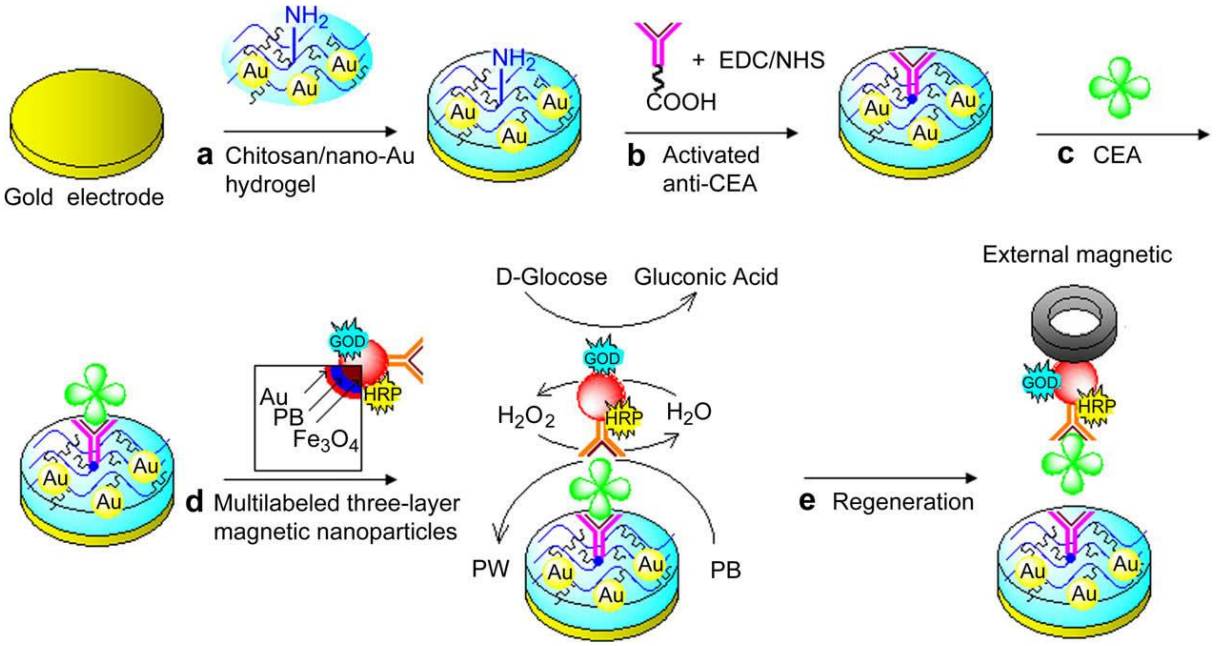

Figure 28. Schematic drawing of the immunosensor fabrication process. (a) Dropping of chitosan–nanoAu hydrogel membrane; (b) immobilizing of anti-CEA; (c) the immunoreaction of CEA and anti-CEA; (d) incubation of the solution containing multi-labelled Fe_3O_4@PB@Au composite magnetic conjugate resulting in an amplified signal-generating detection; (e) separation of the immunocomplex using an external magnetic field permits the regeneration of the immunosensor. Reproduced from Ref. [207] with permission from Elsevier.

III.2.2. H_2O_2 and small molecules detection

As previously mentioned in Section I, PB(A)s are well known for their capacity to electrocatalyze both, oxidation and reduction of H_2O_2.This is relevant because a large number of enzymes produce hydrogen peroxide as a by-product, which may be detected at the electrode using PB(A)s.[119] We will endevour to summarize in this section various published to date contributions related to the detection of H_2O_2 with nanoheterostructures combining PB and another inorganic component as sensitive species for the electrodes. These contributions could be divided in two categories: (*i*) *electrochemical* and (*ii*) *colourimetric* biosensing of H_2O_2.

The electrochemical biosensing has been developed starting from 2007 based on a conventional three-electrode electrochemical cell comprising a modified working electrode. The latter was constituted by a working electrode made of inorganic materials specific for each case modified with nanoheterostructures comprising PB combined with gold, [16], [180] silver, [190] platinum, [183] iron oxides, [216], [218] or MWCNTs. [263], [264] The choice of these specific combinations comes from the fact that PB, as already mentioned, has an excellent electrocatalytic activity but low conductivity. Therefore, its close association at the nanometric scale with a conductive material led to both, a highly electroactive and conductive nanomaterial on the surface of the working electrode. In some cases, these nanoheterostructures are assembled *via* layer-by-layer (LbL) assembly techniques with graphene oxide, [180] poly(allylamine hydrochloride) (PAH), [16] poly(diallyldimethylammonium chloride)

(PDDA), [263] mixed with MWCNTs and PDDA, [183] or gold nanochains and chitosan [264] prior to deposition on the electrode surface. The performances of such devices for the H_2O_2 detection in terms of linearity range, detection limit, sensitivity (S), and response time (RT) in given pH and working potential conditions are summarized in Table 7.

Table 7. Performances of three-electrode electrochemical cells based on working electrodes based on nanoheterostructures involving PB in terms of linearity range, detection limit, sensitivity and response time.

Ref.	Nanoheterostructure	Linearity Range/μM	Detection Limit/μM	Sensitivity/ $AM^{-1}cm^{-2}$	Response time/s	Working potential	pH
[16]	Au@PB	10-40	0.57	0.15	-	0.0	6.8
[180]	Au@PB	1-30	0.1	5.0	10<	-0.1	-
[190]	Ag@PB	10-130	5	0.48	3<	-0.05	6.5
[183]	Pt@PB	0.25-1500	0.15	0.85	2<	0.1	2.0
[216]	γ-Fe_2O_3@PB	100-1200	0.67	$0.2x10^{-3}$	100	0.0	2.0
[218]	Fe_3O_4@PB	1-430	1	-	3-4	-0.1	7.4
[263]	MWCNTs@PB	10-400	0.57	0.15	-	0	6.8
[264]	MWCNTs@PB	1.75-1140	0.5	300	30	0	6.0

Secondly, discrete nanoheterostructures were also considered for the elaboration of *colourimetric sensing devices* for the H_2O_2 detection because PB can be used as an alternative artificial enzyme to catalyze H_2O_2 decomposition following the Fenton reaction leading to hydroxyradicals (Equation (7)), which, in turn, can oxidize the chromogenic substrate 3,3',5,5'-tetramethylbenzidine (TMB) (Equation (8)) (Scheme 5).

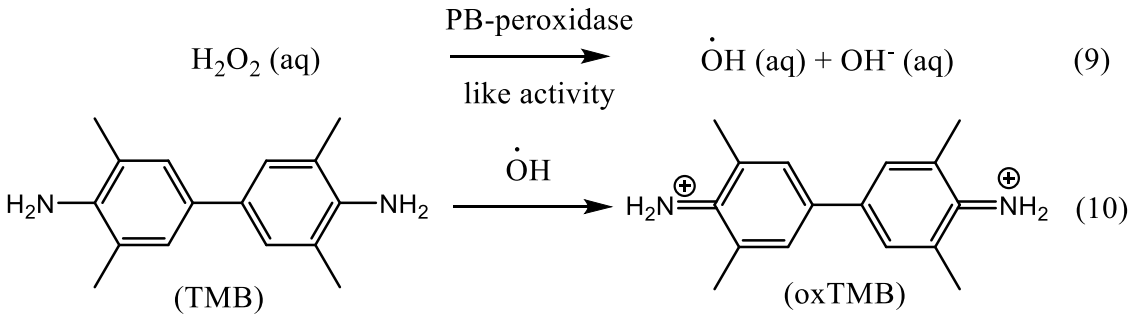

Scheme 5. Peroxidase-like activity of PB leading to H_2O_2 catalyzed decomposition to generate hydroxyradicals species that in turn oxidize TMB to oxTMB (strong blue colour for the latter).

Discrete nanoheterostructures combining PB with either FePt, [203] γ-Fe_2O_3, [215], Au [292] or Co_3O_4 [217] were used as an oxidase-mimic to detect intracellular H_2O_2 in human breast adenocarcinoma (MCF-7) cells, [203] for the detection of glutathione, which acts as an inhibitor of TMB oxidation, [217] for the detection of L-lactic acid [292] and for the detection of immobilized immunoglobulin G (IgG). [215] For that latter purpose, the γ-Fe_2O_3@PB nanoheterostructures were functionalized with staphylococcal protein A (SPA) and BSA to develop an artificial enzyme immunoassay for IgG (Figure 29).

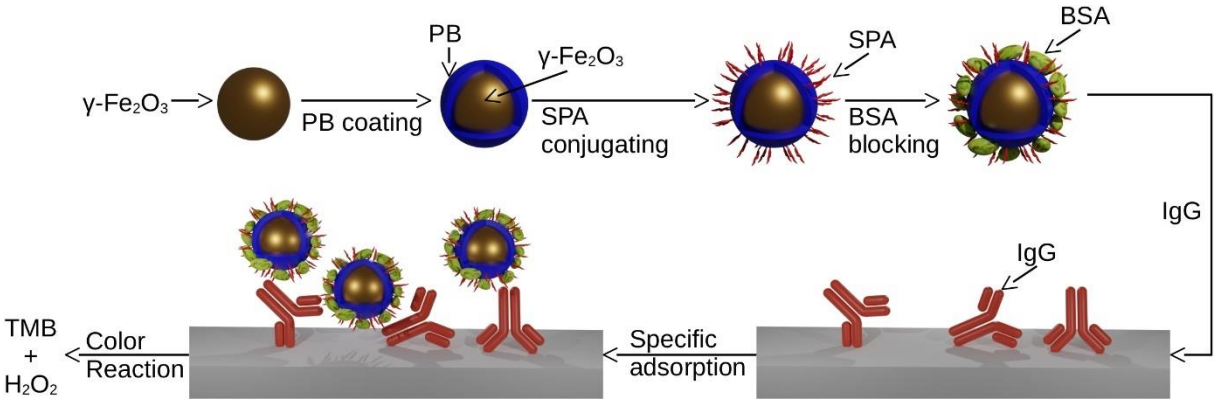

Figure 29. Schematic illustration of the preparation of γ-Fe_2O_3@PB and immunoassays based on γ-Fe_2O_3@PB conjugated with SPA. Reproduced from Ref.[215] with permission from the Royal Society of Chemistry.

Finally, apart from building immunosensors, aptasensors and H_2O_2 detection devices either by electrochemical or colourimetric means, discrete nanoheterostructures involving PB with graphene quantum dots (GQD), [270] or CuS [234] were also used to modify glassy carbon [234] or free-standing graphene fibre [270] working electrodes in a conventional three-electrode electrochemical cell to perform direct oxidation of small molecules such as L-cysteine[270] or ascorbic acid. [234]

III.3. Biomedical applications: design of new multifunctional therapeutic agents and multimodal imaging nanoprobes

Various inorganic nanoheterostructures have attracted immense interest in biomedical applications for several decades because they present a stimulating opportunity permitting to combine several types of imaging and/or therapy in the same multifunctional nano-object. They have been developed as efficient dual and even multi-imaging nanoprobes for improved disease diagnosis, as new multi-therapeutic agents with improved therapeutic action or as new theragnostic agents integrating therapeutics with diagnostic tools to develop new personalized treatments with enhanced efficacy and safety. Numerous combinations of inorganic nanoparticles, such as magnetic iron oxides and ferrites, gold and silver nanoparticles, up converting nanocrystals, quantum dots, and others, have widely been developed for this purpose. There are a number of review papers devoted to this topic. [293], [294], [295] Nanosized PB(A)s have relatively recently been developed as a component of nanoheterostructures devoted to their use for biomedical applications, but they rapidly gained ground as alternatives to conventional inorganic components mainly thanks to their optical and magnetic properties making them highly interesting as PTA for PTT and antimicrobial treatment, as nanoprobes for photoacoustic and MR imaging, but also due to their excellent thermal, photothermal stability and biocompatibility (see Figure 4). PB(A)s type nanoparticles possess also nanoporosity permitting the capture of small drugs and biomolecules, ensuring then the possibility of their deliver under triggered and controlled PTT action. The combination of these versatile PB(A)s nanoparticles with other inorganic components in nanoheterostructures opens a new way towards original associations bringing complementary properties or even providing synergic effects. In this section, we describe first different types

of synergic actions, such as an enhancement of PTT effect brought by a combination of PB with lanthanide-doped nanoparticles, an improved cancer cell killing ability of PTT assisted drug delivery, as well as synergetic therapeutic effects of PTT/PDT and PTT/radiotherapy revealed in several nanoheterostructures including the combination of iron oxides, gold, silica and PMO, MOFs and POM components with PB or doped PB. Secondly, we address the interest in designing multifunctional nanoheterostructures presenting complementary functionalities carried by several components. We describe highly promising theragnostic nano-objects obtained through a combination of PTT with different imaging techniques, such as MRI, optical imaging, SPECT etc., and then multimodal imaging nanoprobes. The theragnostic nano-objects represent the most developed part among the nanoheterostructures designed for biomedical applications with numerous inorganic components associated with nano-sized PB.

III.3.1. Synergic effects

The term synergy comes from the Greek *"synergos"* meaning "working together" and signifies that the interaction of two or more components of nanoheterostructures results in an overall effect that is greater than the sum of individual effects of any of them. Synergic actions in inorganic nanoparticles have often been associated with the design of multicomponent nanoheterostructures, while the clear demonstration of them is not obvious. [296] In this section, we will emphasize the synergic effects that were clearly evidenced in multifunctional nanoheterostructures containing PB as a component describing different studies regarding PTT cross-relaxation enhancement, associated PTT with drug delivery, PTT/PDT multitherapy, PTT/radiotherapy or PTT/chemodynamic therapy.

III.3.1.1. PTT enhancement through a synergic effect

It has been shown in Section I that one of the most extensive development of the nanosized PB for therapeutic features is linked with their exceptional potential for laser-assisted photothermal ablation, making them efficient and stable PTT agents for cancer therapy. Their excellent photothermal stability, which competes with some gold nano-objects or organic dyes, has been outlined in several works. However, PB nano-heater does not work at its maximum efficiency as the usual NIR irradiation happens with a laser at 808 nm whereas the maximum absorption of PB is located at 690–740 nm. [86], [297] One of the original and efficient ways to circumvent this problem consists in the design of nanoheterostructures, where a PB shell possessing a continuous energy band with a strong and broad absorption is combined with Nd^{3+} doped nanoparticles having ladder-like energy levels with great PTT conversion capability. Indeed, both $NaNdF_4$ and PB nanoparticles separately are relatively efficient PTA, but their combination in core@shell nanoheterostructures permits increasing sharply the photothermal efficiency due to a cross-relaxation mechanism. This strategy has successively been employed in two nanoheterostructures, the $NaNdF_4$@PB core@shell [239] and in more complex $NaErF_4$@$NaYF_4$@$NaNdF_4$@PB core@shell@shell@shell [240] nano-objects, where a clear synergic PTT effect has been demonstrated. Its explanation involves an appearance of new cross-relaxation pathways (cross-relaxation (CR2) in Figure 30) operating in the presence of the PB shell. Indeed, in simple $NaNdF_4$ nanoparticles exposed to irradiation at 808 nm, photons can be excited to the Nd^{3+} $^4F_{5/2}$ state and then non-radiatively drop to the $^4F_{3/2}$ level, at which photons can decay to lower energy states through radiative processes to generate the usual Nd^{3+} emissions at 900, 1058 and 1332 nm (transitions from $^4F_{3/2}$

to $^4I_{9/2}$, $^4I_{11/2}$, and $^4I_{13/2}$, respectively). Cross relaxation (CR1) between the $^4F_{3/2}$ to $^4I_{15/2}$ and $^4I_{9/2}$ to $^4I_{15/2}$ states of different Nd^{3+} ions, as well as between other nonradiative transitions to the ground state, generates the photothermal effect in $NaNdF_4$ (Figure 30). The presence of the PB shell brought the continuous energy band of PB in close contact with the ladder-like energy levels of the $NaNdF_4$ core. When photons in $NaNdF_4$ drop from the $^4F_{5/2}$ level to the $^4F_{3/2}$ one, photons in the PB layer may jump from lower to higher energy states with the same energy difference as between $^4F_{5/2}$ and $^4F_{3/2}$, thereby forming new cross relaxation (CR2) pathways with shorter energy relaxation distances and higher non-irradiative energy losses. This will generate more heat in the $NaNdF_4$ and bring the absorbed photons closer to the maximum absorption of the PB at the same time.

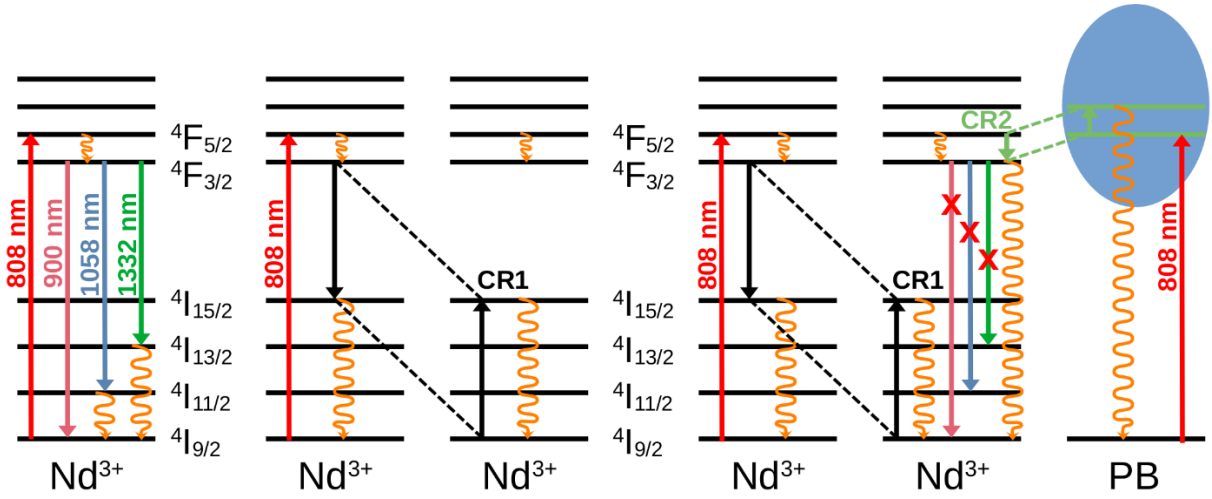

Figure 30. Simplified diagrams of: a) the radiative and nonradiative processes in a single Nd^{3+} ion; b) the cross-relaxation between Nd^{3+} ions in the $NaNdF_4$ core; c) the generation of new cross-relaxation pathways (CR2) between Nd^{3+} ions in the $NaNdF_4$ core and the PB shell.

The onion-like $NaErF_4$@$NaYF_4$@$NaNdF_4$@PB core@shell@shell@shell nano-objects encapsulated in phospholipid PEG micelles were used for the demonstration of an efficient PTT treatment *in vivo* using intratumour (*i.t.*) injection on U14 tumour-bearing nude mice. The size of the tumour in control groups (pure saline injection and $NaErF_4$@$NaYF_4$@$NaNdF_4$@PB injection without 808 nm laser irradiation) increased about 6-fold, while the size of the tumour decreased to half its size after the PTT treatment with nano-objects (see Figure 31). These nanoheterostructures constitute a nice example demonstrating a synergy of the PTT properties providing an important enhancement of treatment efficiency. Moreover, the nanoheterostructures not only demonstrated the enhanced PTT action but also can be followed by optical imaging (NIR emission thanks to the presence of the $NaErF_4$ core). This therefore consitutes a nice example of theragnostic nano-objects (see after).

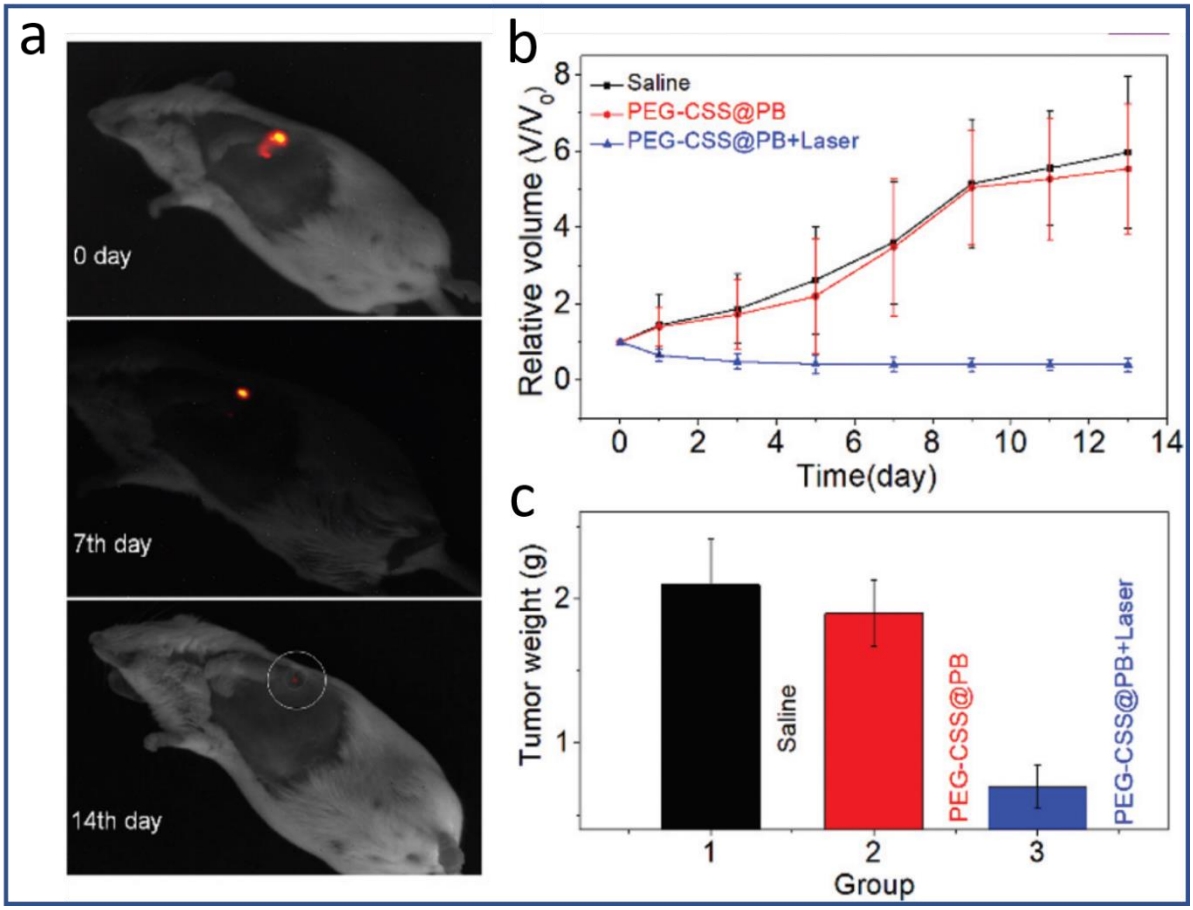

Figure 31. (a) Monitoring the tumour treatment outcome through NIR (window II) imaging, which was recorded at 0, 7, and 14 days post photothermal treatment. (b and d) The average tumour volume and weight in three groups of BALB/c mice, including two control groups (intratumorally injected with saline or a $NaErF_4$@$NaYF_4$@$NaNdF_4$@PB encapsulated in a phospholipid PEG micelle (PEG-CSS) and the PTT-treated group (both with the $NaErF_4$@$NaYF_4$@$NaNdF_4$@PB nano-objects and 808 nm laser irradiation). All of the PTT treatment groups utilized an 808 nm light dose of 1 Wcm^{-2} for 10 min. Reproduced from Ref.[240] with permission from the Royal Society of Chemistry.

III.3.1.2. PTT assisted drug delivery: towards a synergy

Many preclinical researches have demonstrated that complete eradication of tumour cells with only the PTT treatment is rather difficult due notably to the suboptimal laser energy in deep tissues related to the light scattering and absorption effects, limited light penetration and the insufficient tumour target specificity of PTT agents. [298] One of the promising strategies to increase their killing ability and improve the tumour growth inhibition (TGI) efficiency consists in the combination of PTT with another therapeutic tool, such as, for instance, a drug delivery. In that way, the latter is usually assisted and controlled by the PTT action improving indeed the malignant cells killing. Several examples of nanoheterostructures combining PB with Fe_3O_4, [210], [213] Au[189], [204] porous silica or PMO[255], [256], [261] or CaP [299] loaded with classical anticancer drug doxorubicin (DOX) have been developed and the combined efficiency of the PTT/drug delivery has been evaluated. In these nano-

objects, the PB component responsible for the PTT may appear as a core or as a shell and DOX was inserted either in the pores of the PB network (porous or hollow) or into the porosity of the silica, PMO or into organic shells surrounded the nano-objects. Some of these works noted that the killing ability of the combined PTT/drug release is higher in comparison with the sum of two separate actions and demonstrated indeed the synergy. In others, the PTT improves and controls the release of DOX, but the clear demonstration of the synergy has not been proven. Table 8 summarizes the main characteristics of these multifunctional nanoheterostructures.

Table 8. *in vitro* CT, PTT and DOX release performances reported. [a]808 nm. SiO_2-EDA = mesoporous SiO_2 with N-[3-(trimethoxysilyl)propyl]ethylenediamine within the walls, DSPE-mPEG(2000) = 1,2-distearoyl-*sn-glycero*-3-phosphoethanolamine-N-[methoxy(polyethylene glycol)-2000], PAA = polyacrylic acid ; IBU = ibuprofen.

Ref.	Nanoheterostructure	Type of the DOX loading	DOX loading/g per g^{-1} of nanomaterials	Action
[189]	Au@PB yolk@shell	DOX in the PB pores and/or in empty space between the core and the shell	0.11	- Combination of chemodynamic therapy with drug release - DOX release: 75 % after 6 h at pH = 6.0 in the presence of H_2O_2, while only 17.3 % without H_2O_2 - Cell mortality *in vitro*: 81.59 % at 2.5 $\mu g.mL^{-1}$ of DOX/irradiation, 17.49 % only DOX - Synergic effect demonstrated *in vivo* on TGI - Additional: CT imaging due to the presence of the Au core
[204]	PB@PAA-Au Janus	DOX loading through interactions with PAA	0.24	- PTT assisted DOX release at pH = 5.3 - Cell mortality *in vitro*: 92 % for PTT/DOX, while only 57.2 % without PTT - Synergic effect demonstrated *in vivo* on TGI - Additional: CT imaging due to the presence of the Au core
[210]	Fe_3O_4@PB	DOX in the gelatin shell	n.d.	- PTT and gelatinase assisted DOX release: 72.2 % of DOX was released during 48 h with enzyme triggered hydrolysation of gelatin-DOX, only 21.2 % of cumulative DOX was released without gelatinase - Cell mortality *in vitro*: 84 % PTT/DOX (31 % only DOX) (concentration 80 $\mu g.mL^{-1}$) - Additional: magnetic targeting improved PTT action (cell mortality *in vitro*: 18 % with the PTT without magnetic targeting and 29 % combined PTT and magnetic targeting)

[213]	Fe_3O_4@PB	DOX into the DSPE-mPEG 2000 shell	n.d.	- PTT assisted and pH dependent DOX release Dox release : 86.9 % within 72 h at pH = 5.0 (24.7 % at pH = 7.4). - Cell mortality *in vitro* : 74.4 % PTT/DOX, 56.5 % for PTT only and 53 % for DOX only (concentration 10 $\mu g.mL^{-1}$). - Synergetic effect demonstrated for PTT-drug delivery - Additional: magnetic targeting improved PTT-drug delivery action (cell mortality *in vitro*: 91.5 % with magnetic targeting)
[255]	PB@SiO_2	DOX into the silica pores, PEG on the surface	1.31	- PTT assisted and pH dependent DOX release DOX release: 46.6 % at pH = 5.0, while 3.1 % at pH 7.4 in 48 h - Cell mortality *in vivo* : 56.5 % PTT/DOX (18.1 % only DOX, 4.8 % PTT only) with concentration 250 $\mu g.mL^{-1}$ - Synergy demonstrated *in vitro* - Additional: MRI and PA imaging
[256]	PB@PMO	DOX into the PMO porosity, Cy5.5 (fluorophore) Maleimide	0.23	- PTT assisted and pH dependent DOX release: 50.3 % with PTT (40.0 % without) at pH 5.5; 27.6 % with PTT (16.3 % without) at pH 7.4 - Cell mortality *in vitro*: 78.6 % DOX/PTT (*ca*. 40 % only DOX) (concentration 1 $mg.mL^{-1}$) - Additional: MRI, PA imaging
[261]	SiO_2-EDA@PB	DOX in the PB or silica pores	0.275	- PTT assisted and pH dependent DOX release: 92 % PTT (73 % without) at pH = 5 after 24h - Cell mortality *in vitro*: 100 % PTT/DOX, 80 % without PTT (concentration 250 $mg.mL^{-1}$) - Efficiency demonstrated *in vivo* - Additional: PA imaging
[258]	PB porous@SiO_2	DOX in the silica shell IBU in the PB pores	0.23 IBU (0.72)	- Dual key and lock drug (IBU and DOX) carrier - Chemo/PTT effect showing synergy in the cancer cells eradication (in vitro 97 % of the cancer cells killed with the concentration of 500 $\mu g\ mL^{-1}$ and in vivo demonstration) - Additional: T_2 weighted MRI imaging
[299]	Hollow PB@CaP core@shell	DOX in hollow PB	1	- pH responsive PTT assisted drug delivery

	Size: 110 nm core, 160 nm whole size			- Cell mortality *in vitro* : 95 % for the concentration 100 μg.ml^{-1}

Fe_3O_4@PB nanoheterostructures enwrapped by gelatin or PEG were studied *in vitro* only on HeLa cells showing in both cases a combined effect of PTT/DOX release associated also with magnetic targeting thanks to the presence of the magnetic Fe_3O_4 component. For example, the observed cell mortality achieved *ca*. 84 % after PTT assisted DOX delivery treatment with Fe_3O_4@PB nano-objects coated with DOX loaded gelatin, while without laser irradiation, the cell mortality was only *ca*. 31 % at the same concentration. [210] Similar conclusions were drawn when using Fe_3O_4@PB coated with DSPE-mPEG(2000)-DOX (Table 8). [213] Moreover, the effect of a local magnetic field in the enhancement of therapeutic effect through magnetic targeting has been demonstrated. [209], [212] These results show an interesting potential of these nano-objects for combinatorial PTT/chemotherapy based on substantial synergic effects. [210], [213]

Nice PB@SiO_2 nanoheterostructures covered with PEG (see section III.5) [255] present DOX in the silica pores with a very high loading of 1.31 g of DOX per gram of nanoheterostructures with a liberation of 42 % after 8 h (at pH = 5) thanks to the mesoporosity of the silica shell. Such nanoheterostructures were used for the investigation of a synergic therapeutic effect of the PTT assisted drug delivery *in vitro* and *in vivo*, as well as for the demonstration of the theragnostic potential of these nanoparticles, since the nanoparticles can be visualized by using MRI and PA imaging techniques on MCF7 tumor-bearing nude mice. Thus, a cell mortality of 56.5 % has been obtained under NIR irradiation assisted drug delivery in the presence of nanoheterostructures with the concentration of 250 μg.mL^{-1}, while only 18 % of cancer cells has been killed without PTT treatment (Table 8). It has been demonstrated that the cell-killing ability of the PB@SiO_2 nanoheterostructures with PTT assisted drug release was higher than the sum of the PTT treatment and the chemotherapy separately, which proves the synergic effect in the malignant cell killing. A significant increase in tumour growth inhibition (TGI) in the case of PTT/DOX delivery compared with the PTT treatment alone has also been shown. Similarly, PB@POM nanoheterostructures functionalized with fluorophore Cy5.5-maleimide were loaded with DOX. An important liberation of the loaded drug (50 %) has been obtained under NIR irradiation at 808 nm, which is much higher in comparison with the DOX release at pH 5.5 after 48h without irradiation (40 %). This combined effect conducts to an important cell mortality of 78.6 % (over only 40 % without NIR irradiation) with a concentration of 1 mgmL^{-1}. Moreover, T_1-weighted MR and PA imagings demonstrate the accumulation of such nanoheterostructures in MDA-MB-231-Luc tumor-bearing nude mice showing the possibility to employ these nano-objects as theragnostic agents and the added value of the PTT assisted drug release was also demonstrated *in vivo*. [256] Similar results demonstrated the possibility of the PA imaging-guided PTT assisted drug delivery has been reported by using SiO_2-EDA@PB nanoheterostructures. They showed an enhanced DOX release in the presence of NIR irradiation (92 % after 24h with NIR irradiation, while only 73 % without at pH = 5) and an almost total eradication of the cancer cells (only 80 % without PTT) *in vitro* with the treatment of 250 μgmL^{-1} of nanoheterostructures (Table 8).[261] These results have also been confirmed *in vivo*. The ability of these nanoheterostructures to be visible by PA imaging permits therefore, the development of new theragnostic agents. Following a similar idea, porous PB

core@SiO_2 shell nanoheterostructures encapsulated two types of drugs, ibuprofen in the PB pores and DOX in the silica shell and demonstrated the PTT assisted dual drug release with synergic therapeutic effect *in vitro* and *in vivo*. [258] In that case, the porous structure of the PB network obtained in the hydrothermal conditions provides an additional possibility of drug loading/release and the possibility of T_2-weighted MR imaging.

Finally, Au@PB yolk@shell nanoheterostructures have also been developed as new theragnostic tools for the association of the CT imaging with chemodynamic therapy and drug release, acting in synergy. [189] These nano-objects efficiently converted H_2O_2 to $^{\cdot}OH$, which in turn lead to the degradation of the PB framework and induced in this way the enhancement of the DOX release. The latter was 75 % after 6 h at pH = 6.0 in 500 μM H_2O_2, while it was only 17.3 % without H_2O_2. *In vivo* experiments performed on SMMC-7721 or MDA-MB-231 tumour-bearing nude mice with combined $^{\cdot}OH$ generation/DOX release[189] demonstrated an almost total TGI (day 20). The combination of CT imaging with the synergetic PTT/DOX action was also demonstrated *in vivo* for PB@PAA-Au Janus nanoheterostructures with a TGI of 92.9 %, while it is 67.1 % without DOX and 31.4 % without NIR irradiation. [204]

III.3.1.3. Synergistic effects between PTT/PDT and PTT/radiotherapy

Several studies showed the occurrence of a synergic effect between PTT and PDT linked with different phenomena, such as plasmon induced resonance energy transfer (PIRET) in the multicomponent Au@PB@Cu_2O@BPQDs nanoheterostructures due to the presence of Au nanorods and PB shell, [205] porphyrins assisted enhancement of the photocatalytic properties of PB promoting the yield of singlet oxygen ($^1O_2$) in the PB@porphyrine doped MOFs, [249] or tandem catalysis able to convert H_2O_2 to O_2 and then to produce highly reactive $^1O_2$ in the PB@zirconium porphyrin core@shell nanoparticles. [236]

In the first example, multicomponent complex Au@PB@Cu_2O@BPQDs nanoheterostructures have been developed as a smart PIRET-mediated nanoplatform for enhanced, multimodal imaging-guided dual PTT/PDT (Figure 32). They present an important NIR absorption and the ability to self-supply O_2 by catalyzing hydrogen peroxide and to convert O_2 into singlet oxygen species, $^1O_2$, under irradiation at 650 nm in significantly higher amounts compared to Au@Cu_2O nanoparticles without the PB shell. The *in vitro* and *in vivo* assays showed that the combined effect of the generated heat and the toxicity of the singlet oxygen permitted effectively to kill the cancer cells and to totally eradicated tumour when injected into HeLa tumour bearing nude mice at day 14. [205] Moreover, these nanostructures may be visible by T_1-weighted MRI and PA imaging leading to the possibility of a dual diagnostic technique.

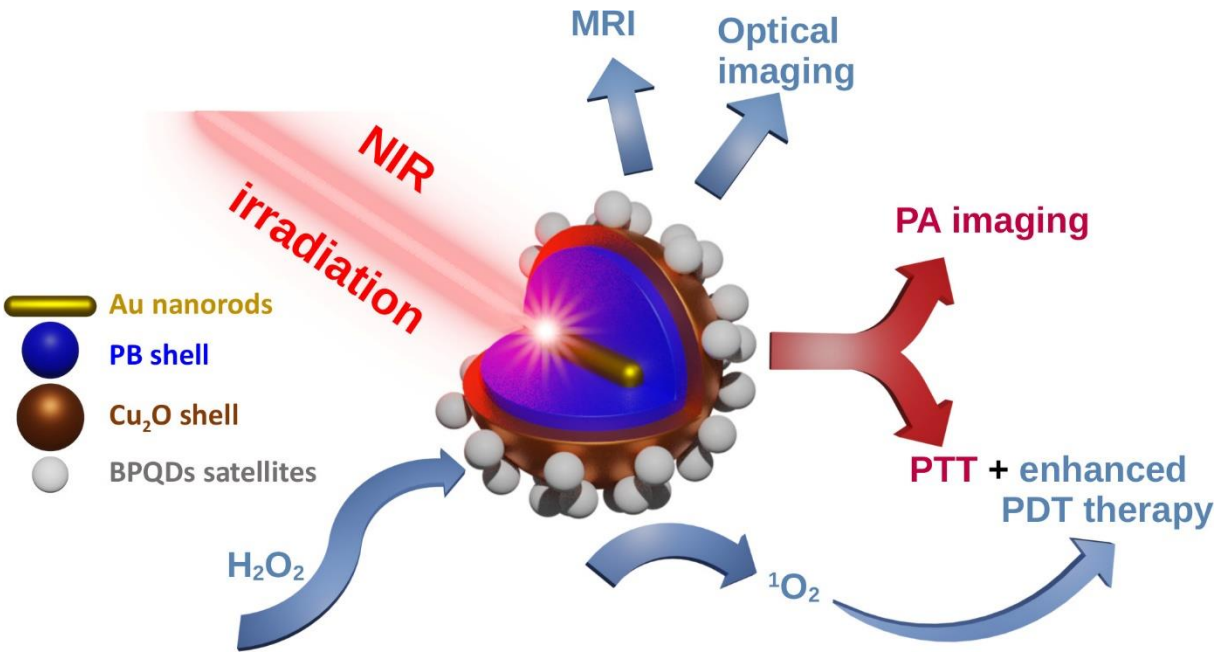

Figure 32. Schematic representation of the complex multifunctional Au@PB@Cu_2O@BPQDs nanoheterostructures showing multimodal imageries and PTT/PDT enhanced therapeutic effect involving PIRET phenomenon (BPQD = black phosphorus quantum dots).

The second example concerns the PB@UIO-66-TCCP nanoheterostructures, where UIO-66-TCPP denotes MOF networks doped with TCPP = tetrakis(4-carboxyphenyl)porphyrin. [249] In that case, a 660 nm red light can trigger the photocatalytic activity of the synthesized MOFs to generate $^1O_2$ with a higher amount in comparison with the pure MOF structures without PB. It was proposed that this phenomenon is due to the formation of a heterojunction between the outer MOF UIO-66-TCCP shell and the internal PB core, which accelerates the charge transport and separation efficiencies beneficial for the production of the active oxygen photogenerated electron−hole pairs (Figure 33).

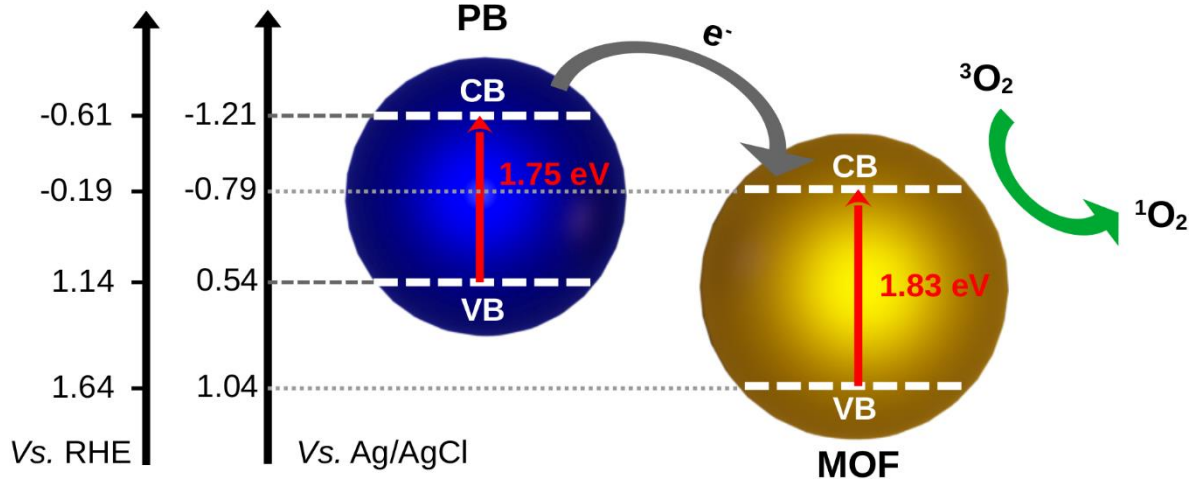

Figure 33. Schematic representation of the proposed photocatalytic mechanism of heterojunction photocatalysts in the PB@UIO-66-TCCP nanoheterostructures.

Such nanoheterostructures were used for their antibacterial and wound healing properties. The experimental results showed that PB@UIO-66-TCCP demonstrated an excellent antibacterial

efficiency in the eradication of *S. aureus* and *E. coli* bacteria (*ca*. 99 %) under dual irradiation at 660 nm for PDT and at 808 nm for PTT, proving indeed the synergistic PTT/PDT action. The efficiency of antibacterial treatment under irradiation at 660 nm involving PB@UIO-66 nano-objects without porphyrin doping was only 53.87 % and 51.9 %, respectively, for the two bacteria (Table 8). The last example showing multimodal image-guided combined PTT/PDT therapy is related to PB@zirconium phosphine core@shell nano-objects. [249] Interestingly, such a combination allows H_2O_2 conversion to O_2 thanks to the catalase activity of PB, which, in turn, enhanced PDT performed by the zirconium phosphine shell. This PDT/PTT tandem through the dual 600/808 nm irradiation on CT26 cell lines showed to be highly efficient *in vivo* with a TGI of *ca*. 100 % on CT26 bearing nude mice. Moreover, the possibility of MRI, PA, IR and fluorescence imaging has also been tested on these nano-objects.

A synergistic effect between PTT and radiotherapy was demonstrated in two works using different systems, PB@Au stabilized by PEI-PEG functionalities [200] and hollow PB@Bi_2O_3 core@satellites nanoparticles. [300] In the former, the capability of the nanoheterostructures to simultaneously be PTA and radiosensitizer was quantitatively evaluated by MTT assays. More than 88 % of the cancer cells treated with PB@Au without irradiation were still alive up to the concentration of 0.4 $mg.mL^{-1}$. The cell viability greatly dropped to 63 % after NIR laser exposures, and it was only 11 % after the synergistic action of these two therapies. The *in vivo* efficacy of the combined treatment was demonstrated on 4T1 tumor bearing nude mice with a near total eradication of the tumors in several days (TGI ~ 94.35 %). It has been proposed that the synergic effect is linked with different actions of two treatments: radiotherapy could kill deeply located cancer cells, and PTT makes the radio-resistant hypoxic cells more sensitive to X-rays helping, then, their eradication. On the other hand, the PB@Bi_2O_3 core@satellites nanosystems comporting hollow PB nanocubes of 120 nm with ultra-small 3–5 nm Bi_2O_3 satellites also exhibited a dual PTT-radiotherapy action enhanced by the oxidative stress effect of the nano-sized PB (Fenton reaction). The demonstrated cell mortality was 55 % as both radiotherapy and PTT treatments have been applied, and 50 % with only the PTT action for the concentration of 100 $\mu g\ mL^{-1}$ of nanoparticles. [300]

III.3.2. Multifunctional agents

In the previous subsection, we described nanoheterostructures in which several components bringing specific properties acted together, providing clearly demonstrated synergetic effects. However, in most cases, the juxtaposition of different properties is usually obtained, leading to the appearance of a simple multifunctionality where the properties act separately. The development of such multifunctional nanomaterials is therefore very important, particularly for biomedical applications with the aim to design new theragnostic agents combining therapeutic functions with different imaging or novel multimodal nanoprobes working simultaneously with different imaging techniques.

Theragnostic is a term derived from the combination of thera(py) with (dia)gnostic in a single nano-object for its employment in the next generation of nanomedicine with the ultimate goal to improve patient outcomes and safety through a personalized approach to medicine. Therefore, theragnostic nano-objects should contain both therapeutic and imaging components, allowing the disease's diagnosis, its treatment and the evaluation of the treatment efficacy

successively. In the recent years, a great effort has been made in the development of such theragnostic nanomaterials based on magnetic iron oxides, gold nano-objects, porous silica nanoplatforms, up-converting nanoparticles, [301] and numerous reviews have been devoted to this topic. [302], [303], [304], [305], [306], [307] In parallel, recent decades have seen important progress in the design of multiple nanoprobes for multimodal imaging bringing complementary information about pathologies from different imaging modalities with a single injection of a contrast agent. [308] As other inorganic theragnostic or multimodal imaging nanoplatforms, the development of PB(A)s based nanoheterostructures has been oriented in these two perspectives and numerous promising theragnostic agents and less numerous multi-imaging contrast agents with a PB(A)s component have been proposed. In most cases, PB is usually used as PTA for the PTT and as a contrast agent for the PA imaging thanks to its optical properties, and other inorganic components bring complementary functions. In the next subsections, we classified PB(A)s' nanoheterostructures in two categories: (*i*) *theragnostic agents involving PTT and different imaging tools*, and (*ii*) *nanoprobes for multimodal imaging.*

III.3.2.1. Theragnostic agents involving PTT and different imaging tools.

Among various theragnostic strategies, one obvious and probably the most explored approach relates to the association of the MRI technique for diagnosis with the PTT therapeutic tool. In the previous sections, we demonstrated that the PB nanoparticles are able to act as an efficient and stable PTA. On the other hand, their performance as the MRI contrast agent is relatively limited because they exhibit only a modest longitudinal relaxivity (r_1) value in comparison with commercial T_1-weighted contrast agents. [79], [78] Two different strategies have been developed with the aim to improve the MRI performance of the nano-sized PB and combine this technique with the PTT. The first consists in increasing the longitudinal relaxivity of PB nano-objects through their doping with paramagnetic high spin ions, such as Gd^{3+}(S = 7/2) or Mn^{2+} (S = 5/2), leading to rising r_1 values and then improving MR contrast of T_1-weighted images. [103], [229] Several articles report on the theragnostic PTT-MRI action of such nanoparticles. [79] Another approach comprises designing nano-heterostructures, where PB is combined with T_2-weighted nanoprobes, such as, for instance, Fe_3O_4, lanthanide ions doped, MnO_2 or FePt nano-components. But in some articles, PB nanoparticles themselves were used as positive MRI CAs even with a relatively low r_1 values. [184] Remarkably, one work reported on core@shell nanoheterostructures of PB@SiO_2 with highly porous PB core, which present exceptionally high longitudinal and transverse relaxivities. [258] Examples of various nanoheterostructures promoting the combination of the PTT properties with the MRI imaging investigated *in vitro* and *in vivo* are summarized in Table 9.

Table 9. Reported data for imaging and PTT performances for theragnostic nanoheterostructures. The r_1 and r_2 values are given relative to the nanoparticle's concentration with a 3.0 T field except when specified. [a][Fe], [b][Dy], [c]0.5 T, [d]7 T. PLL = poly-L-lysine, PDA = polydopamin, BSA = bovine serum albumin, PEG = polyethyleneglycol, DOX = doxorubicin, AlPc = aluminium phtalocyanin, HA = hyaluronic acid, PEI = polyethylenimine, PAH = poly(allylamine), BPQDs = black phosphorus quantum dots, PCN = zinc phosphine, MEM = tumor cell membrane extract, PMO = periodic mesoporous organosilica, CQDs = carbon quantum dots. GNR = gold nanorods, Anti HER2 = human epidermal growth factor receptor 2,

DOPC = 1,2-dioleoyl-sn-glycero-3-phosphocholine, DSPE-mPEG(2000) = 1,2-distearoyl-*sn*-*glycero*-3-phosphoethanolamine-N-[methoxy(polyethylene glycol)-2000]; g-PEG = NH_2-PEG (5 kDa).

Ref.	Nanoheterostructures	Stabilizing agent	Imaging	Therapy	Theragnostic action
[200]	PB@Au core@sattelites 87 nm/13.2 nm	PEI-PEG	MRI (relaxivity r_1=7.48 $mM^{-1}.s^{-1}$ [a], r_2=8.02 $mM^{-1}.s^{-1}$ [a]), CT	PTT (λ_{ir}=808 nm, η=n.d.), radiosensive therapy	Therapy: synergy in PTT and radiosensitive therapy, Dual MRI, CT imaging
[184]	Au@PB core@shell 55 nm/ 11 nm	hyaluronic acid	MRI, (relaxivity r_1=0.86 $mM^{-1}.s^{-1}$ [a], r_2=5.4 $mM^{-1}.s^{-1}$ [a]), SERS	PTT, PDT (λ_{ir}=808 nm, η=44 %)	Therapy: PTT/PDT synergy demonstrated Dual SERS, MRI imaging:
[205]	Au nanorods@PB@Cu_2O @BPQDs core@shell@shell@satellites multicomponent nano-objects Au nanorods 110 nm/ PB shell 10 nm	poly-(allylamine)	MRI (relaxivity r_1=5.578 $mM^{-1}.s^{-1}$ [a] r_2=n.d.), PA	PTT/PDT (λ_{ir}=650 nm, η =25.73)	Therapy: plasmon-induced resonance energy transfer (PIRET) - mediated nanoplatform for PDT/ PTT Imaging: MRI and PA
[241]	$NaDyF_4$:50%Lu@PB core@shell 25-38 nm core/2.5 nm shell		MRI (relaxivity r_1=0.11 $mM^{-1}.s^{-1}$ [b, c] r_2=2.19 $mM^{-1}.s^{-1}$, [b, c] 337 $mM^{-1}.s^{-1}$ [b]), CT	PTT (λ_{ir}=808 nm, η =50.7 %, λ_{ir}=785 nm, η=60.6 %)	-
[240]	$NaErF_4$@$NaYF_4$@ $NaNdF_4$@PB core@shell@shell@shell Size: 14.9/27.7/51.1 nm	Phosphlipid -PEG	Optical imaging λ_{exc}=980 nm, λ_{em}=1525 nm (Er^{3+}) or λ_{exc}=808 nm, λ_{em}=1064 nm (Nd^{3+})	PTT (λ_{ir}=808 nm, η=50.5 %)	Therapy: enhanced PTT through cross relaxation (synergy) Imaging: NIR Er^{3+} fluorescence (exc. at 980 nm) (window II)
[242]	$CaMoO_4$:Eu@SiO_2@ Au nanorods satellites/PB Multicomponent nano-objects	Anti HER2	Optical imaging λ_{exc}=464 nm, λ_{em}=615 nm, SERS	PTT (λ_{ir}=808 nm, η=30.6)	-
[209]	Fe_3O_4@PB well definite core@shell 15-20 nm/3 – 6 nm	-	MRI (relaxivity r_1=n.d. r_2=58.9 $mM^{-1}.s^{-1}$)	PTT (λ_{ir}=808 nm, η=n.d.	-

[212]	Fe_3O_4@PB@$CuInS_2$-ZnS core@shell@satellites 40.1 nm /5 nm	PEI/BSAhyaluronic acid	MRI (relaxivity r_1=n.d. r_2=1.92 $mM^{-1}.s^{-1}$ [a]), NIR fluorescnece	PTT (λ_{ir}=808 nm, η=n.d.)	Therapy: PTT improved with magnetic targeting
[214]	Fe_3O_4@PB Core@shell not well define 12–15 nm core/3-5 nm shell	PDA, BSA aluminum phthalocyanine (AlPc) as PDT photo-sentisizer	Trimodal imaging: MRI (relaxivity r_1=n.d. r_2=61.45 $mM^{-1}.s^{-1}$ [d]), NIR fluorescence, PA	PTT/PDT (λ_{ir}=660 nm, η=22.3 %)	Therapy: combined PDT/PTT with magnetic guidance
[211]	Fe_3O_4@Gd^{3+} doped PB core@shell 8nm core/10 nm shell	-	MRI (relaxivity r_1=5.5 $mM^{-1}.s^{-1}$ r_2=126 $mM^{-1}.s^{-1}$)	PTT (λ_{ir}=808 nm, η=16.1 %)	-
[250]	PB@zirconium phosphinecore@shell 110 nm core/15 nm shell	MEM	MRI (relaxivity n.d.), fluorescence, PA, IR	PTT/PDT (λ_{ir}=808 nm, η=n.d.)	Therapy: PDT/PTT synergy demonstrated Imaging: multimodal MRI, fluorescence, PA, IR
[221]	PB@MnO_2 core@shell 50 nm core /5-39 nm shell	-	MRI (relaxivity r_1=4.9 $mM^{-1}.s^{-1}$ r_2=15.4 $mM^{-1}.s^{-1}$), PA	PTT (λ_{ir}=808 nm, η=n.d.)	Therapy: PTT, oxygen regulation of the exografted breast cancer
[149]	PB@SiO_2 core@shell 82 nm core/34 nm shell	PEG/DOX	MRI (relaxivity n.d.), PA	PTT/drug release (λ_{ir}=808 nm, η=n.d.)	Therapy: PTT assisted pH responsive drug release, Imaging: MRI, PA in vivo
[258]	Porous PB@SiO_2 core@shell dendrimer-like silica shell	PEG IBU included in the PB, DOX in the silica shell	MRI (relaxivity r_1=17.2 $mM^{-1}.s^{-1}$ r_2=193.3 $mM^{-1}.s^{-1}$), fluorescence	PTT assisted dual drug release (λ_{ir}=808 nm, η=n.d.)	Therapy: PTT assisted dual drug release (IBU and DOX), synergic therapeutic effect Imaging: T_2 weighted MRI in vivo,
[271]	PB@CQDs core@shell 50 nm core	-	Optical imaging λ_{exc}=400 nm, λ_{em}=460 nm, 540 nm	PTT (λ_{ir}=808, η=30 %)	-
[224]	PB/MnO_2	Polydopamine linked with chlorine e6	MRI (relaxivity n.d.)	PTT/PDT (λ_{ir}=660 nm, η=n.d.)	Therapy: dual PTT/PDT synergy claimed (but not proved) High therapeutic effect PTT, ROS

					generation, oxygen production from H_2O_2 Imaging T_1 weighted MRI Complete eradication of cells/tumour
[197]	PB@FePt core@satellites	Hyaluronic acid, g-PEG	MRI, (r_2 = 15.58 $mM^{-1}.s^{-1}$), CT, PA	PTT (λ_{ir}=808 nm, η=28.14 %) chemodynamic therapy	Dual therapy: chemodynamic and PTT, but synergy is not demonstrated Imaging: MRI, CT, PA
[300]	Hollow PB@Bi2S3 satellites 120 nm core, 3 – 5 nm satellites	-	CT	PTT/radio-therapy (λ_{ir}=808 nm, η=29.26 %)	Dual PTT-radiotherapy enhanced by oxidative stress (Fenton reaction) Cell mortality: PTT/RT 55 % for 100 μg ml^{-1} Imaging : CT

Among those, several reports are related to the combination of Fe_3O_4 core with the PB shell (see section III.2.1), the magnetic iron oxide part being exploited as T_2- weighted (negative) MRI contrast agents and also for magnetic targeting and the PB component as the NIR-driven PTA. [209], [212], [214] Generally, such nanoheterostructures were covered with biocompatible molecules or species, such as PDA (polydopamine), AlPc (aluminium phthalocyanine), BSA (bovine serum albumin), [212] and hyaluronic acid (HA) [214] in order to render them biocompatible, well dispersible and stable in physiological media at physiological pH. The reported transverse relaxivity values, r_2, comprised in the range 58 – 62 $s^{-1}mM^{-1}$ are relatively modest in comparison with those of the commercial negative contrast agent Endorem (93 $mM^{-1}s^{-1}$ at 3 T), [309] usually used as a benchmark for iron oxide nanoprobes, with the exception of Fe_3O_4@Gd^{3+}- doped PB nano-objects showing r_2 = 126 $s^{-1}.mM^{-1}$. However, the reported works demonstrated that these nanoheterostructures can easily be followed by the MRI technique. All these nanoheterostructures demonstrated a good PTT performance providing an efficient temperature elevation under irradiation between 600 and 808 nm. It depends on several parameters, including the type of the nano-system, the nanoparticle concentration, laser power, surface of irradiation, type of irradiation (single or two photons), molar extinction value, wavelength of irradiation and others, and it is not possible to qualitatively compare their PTT activity based on only these results. We can only state that in all cases, the temperature elevation permitted the cancer cells eradication. However, some

works (see Table 9), report on the light-to-heat conversion efficiency allowing the direct comparison of their PTT performance between them and also with conventual PTT agents. For the Fe_3O_4@PB nano-systems, these values are comprised in the range 16–22.3 %. In comparison, the conventional PTA Au nanorods present a conversion efficiency of 22.1%. [310] Those nanoheterostructures were also tested *in vivo* with prior MTT assays with HUVEC, [209], [212] or 4T1[214] cells lines demonstrating their biocompatibility. *In vivo* MRI experiments were performed in reported cases and showed the accumulation of the nanoheterostructures in tumours using U87MG, [209] HeLa[212] or 4T1[214] tumour-bearing nude mouse model with *i.v.* injection. Remarkable TGI of 87.2 %, [209] 61.85 %[212] and *ca.* 100 %[214] at day 18 were obtained by applying NIR-driven PTT when magnetic targeting was applied. [212], [214] In relation to the investigation of the PTT efficiency *in vivo*, Figure 34 shows the local temperature increase in tumour under a NIR laser irradiation in the presence of Fe_3O_4@PB nanoheterostructures and under magnetic guidance. [212]

Magnetic FePt alloy nanoparticles were also associated with PB in PB@FePt core@satellites nanostructures exhibiting dual chemodynamic-PTT therapy and presenting triple-modal MRI/CT/PA imaging possibility. [197] In these nano-systems, FePt nanoparticles brought the negative MRI contrast with the transverse relaxivity value of 15.58 $mM^{-1}s^{-1}$ thanks to their magnetic properties and CT imaging due to the presence of Pt. On the other hand, PB ensures PTT and PA imaging. Note that the PTT efficiency of these nanoheterostructures has been determined as 28.14 % and a relatively good cancer cell mortality of 75 % has been observed for a concentration of 90 μg ml^{-1}.

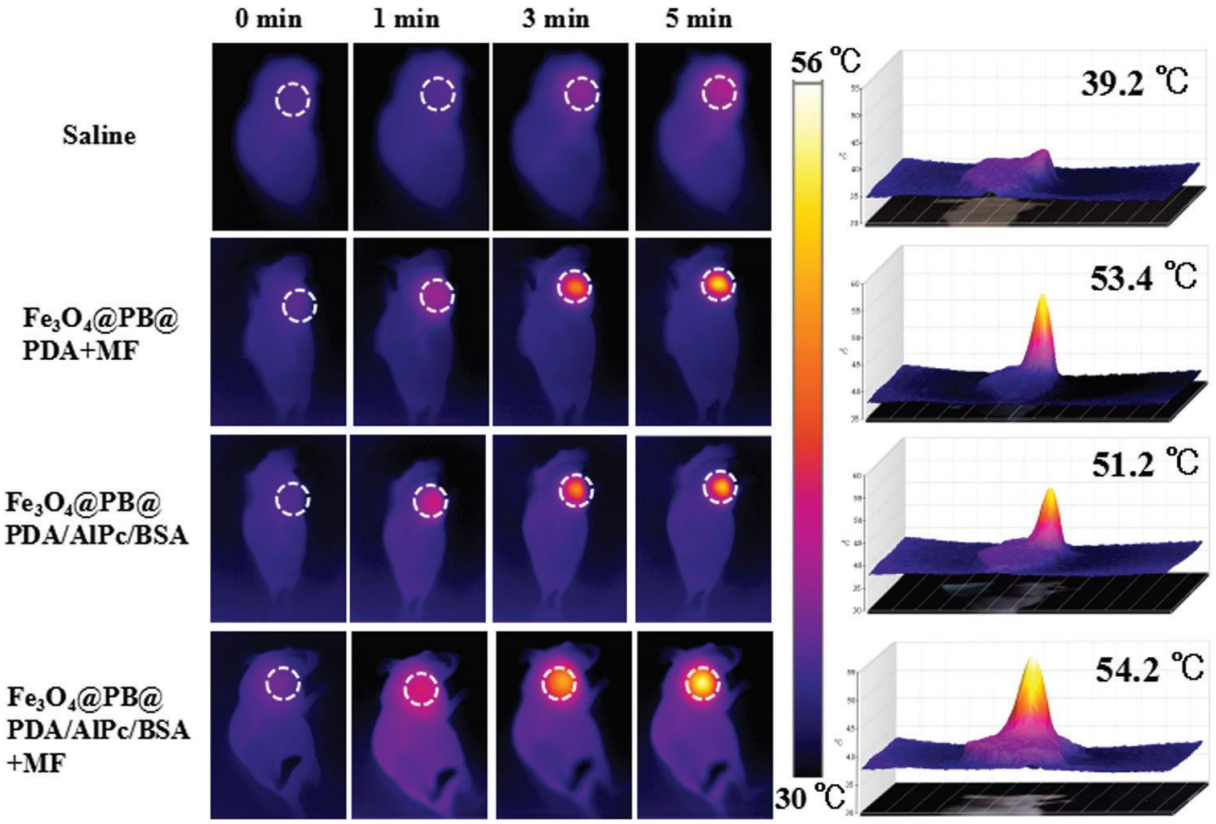

Figure 34. Thermographic images of mice 12h post *i.v.* injection of saline Fe_3O_4@PB functionalized with PDA and PDA/AlPc/BSA under a 660 nm laser (1 $W.cm^{-2}$) irradiation

during 5 min. (PDA= polydopamine, AlPc = aluminum phthalocyanine). Reproduced from Ref.[214] with permission from the Royal Society of Chemistry.

Other nanoheterostructures designed as MRI/PTT theragnostic agents consist in the combination of Au and PB (see section III.1), where PB is used as both, the T_1 relaxing MRI CA and the NIR driven PTA. The Au core or shell brought the PTT action or the combination between PTT and PDT treatments improving the ability of the cancer cell killing and offering the possibility to follow them with PA or CT imaging techniques. In the case of Au@PB core@shell nano-objects, a very high light-to-heat conversion coefficient of 44 % (at 808 nm irradiation) has been reported, but the synergic PTT effect between the two components has not been clearly demonstrated. The MTT assays were performed using 4T1[200], [184] and HeLa cells lines[205] to establish the cytotoxicity aspects related to these nanoheterostructures. *In vivo* studies were performed to investigate their TGI performances on 4T1 and HeLa tumor-bearing nude mice showing interesting synergy of radiotherapy and PTT with 94.35 % TGI at day 14[200] or PDT/PTT with significant improvement of TGI compared to the PTT alone (See section IV-3-2-3). [184], [205] However, concerning the activity of these nano-objects as MRI CAs, the reported r_1 values are not coherent from one work to another, probably due to the different modes of measurement and calculations and it is difficult to compare them..

Two examples of nanoheterostructures involving PB as the NIR-driven PTA were also developed by its coupling with $NaDyF_4$:x%Lu[241] or MnO_2. [221] The use of $NaDyF_4$:x%Lu as one of the components allows considering the obtained nanoheterostructures (see section II-3) both, as a T_2 MRI CA and as nanoprobe for CT. The very high conversion efficiency of *ca*. 60 % at 785 nm irradiation has been reported for these nanoheterostructures. [241] They were also tested *in vivo* on HCT116 tumor-bearing nude mice and followed by MRI and CT imaging. The irradiation at 785 nm at 0.67 $W.cm^{-2}$ for 5 min allowed the almost total eradication of the tumour at day 14. When using MnO_2, the obtained nanoheterostructure could be used as CAs for MRI and for PA imaging. The last example of MRI/PTT combination with an additional multimodal PA and fluorescence imaging was demonstrated with the PB@zirconium phosphine nanostructures further covered with a CT26 tumour cell membrane (see sections II.4 and III.3.2.1). [250]

Finally, a recent example of PB@silica shell nanoheterostructures containing porous PB core and porous silica shell able to be loaded by two different drugs, ibuprofen and DOX and designed as MRI guided PTT assisted dual drug delivery nanomedicine should be cited. Interestingly, these nanostructures present exceptionally high values of both relaxivities, r_1 = 17.2 and r_2 = 193.3 $mM^{-1}\,s^{-1}$, visibly due to the important porosity of the PB network. However, the mechanism of those has not been fully understood. The *in vitro* and *in-vivo* results indicate an almost total eradication of cancer cells or tumour in studied conditions. [258]

Another category of theragnostic agents is based on nanoheterostructures combining PTT with optical imaging. The fluorescence is brought to these nanoheterostructures through carbon quantum dots[271] (see section III.3.2.1) or phosphors that could be either $CaMoO_4$:Eu[34] or $NaEr_4$@$NaYF_4$@$NaNdF_4$ (see section III.3). [240] *In vivo* experiments performed under irradiation were shown to limit tumour growth or lead to a TGI of *ca*. 50 %, respectively, when treating C6 or HeLa tumour-bearing mice with PB@CQDs[271] or

$CaMoO_4$:Eu@PB@GNR@Anti HER2 by *i.p.* or *i.v.* injection. [240] A last example shows the combination of PA and CT imaging techniques with PTT using an Au@PB nanoheterostructure that shows a TGI of 100 % at day 6 on HT29 tumor-bearing nude mice with *i.v.* injection using the PTT alone. [179]

III.3.2.2. Nanoprobes for multimodal imaging

Current commercial contrast agents can usually be imaged by one imaging method bringing only impart uniparametric information. The concept of multimodal imaging nanoprobes refers to the design of smart multifunctional nanomaterials able to simultaneously provide signals for more than one imaging technique. Multimodal systems, in general, allow for utilizing the strengths of each imaging system while overcoming their limitations. [311], [312] Numerous inorganic nanostructures of different compositions, sizes, morphologies have been developed for this purpose. [312]

Among those, several examples of nanoheterostructures involve PB as one of the components. Some of them focus on nanoheterostructures including PB as an element of imaging probes for surface-enhanced resonance raman scattering (SERRS), [164] SPECT [167] or dual imaging associating fluorescence and MRI [269], [254] or SERS and MRI. [186] Indeed, PB was shown to be an ideal Raman reporter exhibiting a single sharp peak at 2156 cm^{-1} related to the cyanide stretching vibration. [164] Such a particularity was exploited using Au@PB nanoheterostructures functionalized with poly-L-lysine (PLL) and anti-IgG antibodies, [164] hyaluronic acid, [184] vancomycin, [187] aptamers, [185] or ovalbumin. [186] With the help of the plasmonic enhancement of the gold core, the cyanide groups exhibited a specific, strong and stable SERS emission in the Raman-silent region (2000 – 2200 cm^{-1}) that allows considering them as new probes for the SERRS technique. In two former cases, the potential of the SERRS imaging was validated *in vitro* by using specific cells, able to be recognized by the functional groups situated on the surface of the nanoheterostructures. These nanotags were further used for the development of a high-sensitivity immunoassay for detection cancer cells, bacteria or for *in-vivo* imaging at the single or even subcellular level. Au@PB nanoheterostructures also provided a visible brightness on the T_1/T_2 scanned MR images even if the longitudinal relaxivity value was found modest (0.86 $mM^{-1}.s^{-1}$). In order to improve it, Gd^{3+}- doped PB has been used as a shell. [186] In that case, a high longitudinal relaxivity of 24 $mM^{-1}.s^{-1}$ and an excellent contrast in the T_1-weighted *in-vivo* MR images have been obtained. These works demonstrated a new potential of Au@PB nanoheterostructures as bimodal nanoprobes for zero-background SERS signal imaging coupled with MRI. [184], [186]

A similar type of Au@PB structures (see section II.1.1) was used with further sorption of radioactive $^{201}Tl^+$ ions to use them as a nanoradiotracers for SPECT imaging. [167] In that case, the nanoheterostructures were functionalized with dextran or a lipid bilayer, and SPECT was employed to investigate the nanoheterostructure biodistribution to determine the influence of the surface coverage and evaluate the kinetic of biodistribution in mice.

Finally, two examples related to the design of multimodal imaging nanoprobes where MRI was combined with optical imaging consist in carbon spheres@PB functionalized with samarium ion through tricarboxylic acid [269] (See section II.6.1) or $Mn_3[Co(CN)_6]_2$@SiO_2 nanoheterostructures. [254] The former system was used as both the MRI contrast agent and a

fluorescent marker showing transient localization of the nanoheterostructures in the brain, but both properties mainly come from the presence of paramagnetic and fluorescent Sm^{3+} attached on the surface of the nano-objects. In the latter, MRI was associated with two-photon excited fluorescence microscopy. Both properties come from the $Mn_3[Co(CN)_6]_2$ core, but the longitudinal relaxivity enhancement (r_1 = 10.52 $mM^{-1}s^{-1}$) is clearly observed due to the presence of a silica shell while the mechanism of this effect was not clarified. Most of these studies demonstrate the low toxicity of such nanoheterostructures and their long circulation time that makes them interesting agents for various imaging techniques in biological systems. Table 10 summarizes the main characteristics of these nanoheterostructures.

Table 10. Main characteristics of nanoheterostructures proposed as dual imaging nanoprobes.

Ref.	Nanoheterostructure	Coating	Imaging
[184]	Au@PB	hyaluronic acid	SERRS emission in the Raman silent region MRI (r_1=0.86 $mM^{-1}s^{-1}$)
[164]	Au@PB	polylysine/AntiIgG antibody	SERRS
[186]	Au@PB	ovalbumin	SERRS emission MRI (r_1=24 $mM^{-1}s^{-1}$)
[168]	Au@PB/$^{206}Tl^+$	Dextran, lipidic bilayer	SPECT
[269]	$C_{spheres}$@PB core@shell	Benzene tricarboxylate/Sm^{3+}	MRI (r_2=12.93 $mM^{-1}s^{-1}$) Fluorescence Sm^{3+} based (emission 563 nm, 599 nm/excitation 680 nm 2 photons)
[254]	$Mn_3[Co(CN)_6]_2$@SiO_2	-	MRI (r_1=10.52 $mM^{-1}.s^{-1}$) 2 photons fluorescence Imaging (excitation 720 nm)

III.4. Other applications

III.4.1. Catalysis

Few examples of discrete nanoheterostructures comprising PB(A)s combined with a metallic component, such as Pt, [192] Pd, [194], AgAu [198], or PdCo [191], were studied for their catalytic properties. Their elaboration is based either on the synthesis of the PB(A)s nanoparticles followed by subsequent addition of the same cyanometallate and the metal salt that will be reduced spontaneously in the reaction conditions to afford the metallic component[192], [194] or by the simultaneous formation of the PBA and the metallic component also obtained from a spontaneous reduction of the metal salt [191] or the post-synthetic adsorptionof the organometallic precursor $[Au^{I}_2Ag^{I}_2(C_6F_5)_4(OEt_2)_2]_n$ followed by its spontaneous reduction[198] (see section II.1.1). The as-obtained discrete nanoheterostructures PB@Pt, [192] core@shell CoCo-PBA@Pd[194], NiCr-PBA@AgAu [198] and nanoflowers PdCo-PBA@PdCo [191] show in all cases tiny metallic or metallic alloy nanoparticles situated in the PB(A)s porosity or on the surface interesting for catalytic applications. Such intricate structures usually allow the observation of synergetic effects, which were demonstrated, for

instance, in the Suzuki coupling of aryl chlorides using CoCo-PBA@Pd [194] or in the case of the plasmon assisted reduction of 4-nitrophenol with enhanced catalytic effect in the presence of core@satellites NiCr-PBA@AuAg nano-objects. [198] In the former case, the enhanced catalytic activity has been explained thanks to : (*i*) the presence of Pd nanoparticles of almost 3 nm without surface organic groups; (*ii*) the amounts of cavities and channels of the PBA supports, which benefit to reagent adsorption, (*iii*) the occurrence of metal nodes of the PBA usually having unique catalytic coordination environments, and (*iv*) the occurrence of two valent states of Pd including Pd(0) and Pd(II) in the catalyst. Further, in the $Co_3[Co(CN)_6]_2$ core, Co^{2+} ions may provide an extra electron to Pd maintaining then the charge balance. Thus, it is reasonable to expect that the Pd sites with the energetic electrons will exhibit superior catalytic activity in comparison with the pure Pd nanoparticles for the Suzuki reaction. Further experiments comparing this catalyst with others confirmed that the channels and cavities of the PBA, Pd(II) and Pd(0) contributed to the reaction, even when the PBA supports was not able to catalyze the reaction demonstrating the synergetic effect.
In the latter case, the synthetic approach consists in the adsorption of the bimetallic precuror $[Au^{I}_2Ag^{I}_2(C_6F_5)_4(OEt_2)_2]_n$ onto preformed NiCr-PBA nanocubes followed by its spontaneaous reduction. This concerted adsorption/reduction mechanism afford NiCr-PBA@AuAg nano-objects having the ultrasmall AuAg alloy satellites on the surface of the PBA cubes. Such nanoheterostructure presents improved catalytic activity for the reaction of the 4-nitrophenol reduction in comparison with the pristine NiCr-PBA. Moreover, these performances have been heightened upon light irradiation due to a plasmon-assisted catalytic effect originating from the bimetallic AuAg satellites. Note that the satellites keep their position on the PBA surface event after several catalytic cycles. [198]

III.4.2. Caesium adsorption

Certain radioactive isotopes (such as ^{137}Cs with a long half-life of 30.2 years) are produced in the normal function of nuclear plants and are dangerous for the environment and for living organisms. As stated in Section I, bulk PB(A)s and their nanocomposites are widely used for removal of radioactive Cs^+ in nuclear plants, and PB is well known under its trade name Radiogardase® approved by FDA for decontamination of the human being. Recent developments in this field of research were orientated towards the use of supported PB(A)s nanoparticles demonstrating the capture of Cs^+ in higher amounts with faster kinetics. [313] Two reports mentioned the use of discrete nanoheterostructures based on PB [49] or CuFe-PBA [267] combined with MWCNTs for electrochemically assisted adsorption [267] or Cs^+ sorption associated by magnetic separation with the employment of iron oxide nanoparticles (see section II.6.1).[219] In particular, MWCNTs@CuFe-PBA show a large Cs^+ sorption capacity of 171 mgg^{-1} with 95 % of the Cs^+ removal in 1 ppm Cs^+ solution, far above in comparison with the only CuFe-PBA materials (105 $mgg^{-1}$and 60 % of the Cs^+ removal). Further, for MWCNT@CuFe-PBA hybrids, the maximum sorption capacity value can reach up to 310 mgg^{-1} when considering electrochemical adsorption. In the latter case, the distribution coefficient reaches up to 568 Lg^{-1}, while chemical adsorption system gives a smaller K_d value of 389 Lg^{-1}. In addition to the remarkable Cs^+ selectivity and removal performance, MWCNTs@CuFe-PBA hybrids can be recycled and show a high stability during Cs^+ disposal.

This example clearly demonstrates the interest of such discrete nanoheterostructures allowing higher cesium ion removal performances compared to the PBA component alone and recyclability of the nanomaterial.

III.4.3. Microwave absorption

An ideal microwave-absorbing material should present a low density, a tiny thickness, a high efficiency, wide absorption frequency ranges, and a low cost. It should be noted that if PB(A)s were used as precursors through calcination to afford materials for such application, [314], [315], [316], [317] they have never been used alone as is. A recent paper demonstrates the interest of PB@MoS_2 discrete nanoheterostructures for such application combining the high electrical conductivity and polarization effect of MoS_2 with PB that is a porous semiconductor with room-temperature conductivity values ranging from 10^{-11} to 10^{-5} Scm^{-1}. [235] The PB@MoS_2 nanoheterostructures were homogeneously mixed with a paraffin wax with different amounts of product, and toroidal shaped samples were prepared for measurements. The results showed the hybrid PB@MoS_2 core@shell structure has excellent microwave absorbing properties with minimum reflection loss values of −42.83 dB with a thickness of 2.1 mm at 16.46 GHz and −42.06 dB at the frequency of 11.44 GHz with a thickness of 2.5 mm with a 40 wt% loading of PB@MoS_2/wax. The effective absorbing bandwidth could reach 7.31 GHz at 2.4 mm, 7.44 GHz at a thickness of 2.5 mm, and 7.17 GHz at a thickness of 2.6 mm. Comparison with PB nanocubes alone showed that the introduction of MoS_2 layers resulted in a significant improvement in the microwave absorption property in both, relaxation and conduction losses. Such an observation was explained by the fact that in addition to how much defects and dipoles can enhance dielectric loss, and the wrapping of the PB nanocubes with several MoS_2 stacked layers, the interfaces between MoS_2 and PB cubes can also introduce more interfacial polarization to improve the absorbing properties demonstrating the interest of such combinations at the nanoscale. More recently, Fe_3O_4@PB core@shell nanoheterostructure was integrated in a composite in association with short carbon fibers and epoxy resin affording a butterfly-scale metamaterial absorber. [318]

Outlook & perspectives

In this Review, we have surveyed recent advancements in the design, properties and applications of nanoheterostructures involving nano-sized PB(A)s as a component associated with other inorganic materials. Indeed, these intricate nano-systems have attracted a great deal of interest in the two recent decades in several applicative domains due to their intrinsic multifunctionality allowing the appearance of synergic effects or separate actions of multiple physical and chemical properties. This type of nanomaterials emerged relatively recently in comparison with other inorganic nanoheterostructures, but they rapidly become active and competitive in the field of energy, biology and health, sensors, catalysis, decontamination etc.
Even though Prussian blue (PB) has been discovered in the early 18th century, this material and its analogues (PBAs) are still a topic of intense contemporary research activities. From its initial discovery and its first application as a blue pigment, it has been the subject of renewed particular interest in the field of research twice since then. First, in the 20th century for the remarkable

magnetic and photomagnetic properties of some of its analogues and for their remarkable sorption properties of caesium ion in the disposal of nuclear waste, then around twenty years ago with the development of studies devoted to PB(A)s at the nanometric scale. Notably, what is known as bulk PB synthesized more than three centuries ago is actually a more or less dispersible aggregate of nanoparticles, referred to as the so-called “soluble” or “insoluble” forms. But what marked the revival of interest in this compound and its analogues at the nanoscale resides in the possibility to finely control the size, the morphology, the surface and the aggregation state and eventually the nanoparticle organization, and indeed their physico-chemical properties. This, in turn, it gives a wide field of opportunities not only in the enhancement of performances for already identified applications but also open a door in new application fields. Indeed, PB at the nanoscale possesses remarkable sorption, catalytic, redox properties, efficient conversion of light into heat, stability, biocompatibility and others. Benefiting from decades of research on the development of inorganic nanoparticles, the synthesis and study of nano-sized PB(A)s has grown at a rapid pace. Thus, since 2000, research efforts have led to the development of PB(A) nanoparticle design from a few to several hundreds of nanometres stabilized by an electrostatic and/or a steric route in different media (aqueous, organic, liquid ionic etc.). A wide variety of stabilizing agents ranging from simple molecules and biomolecules (including numerous biomolecules of interest) to polymers, , have been used for this purpose.

These advancements have paved the way for a finding to associate this material with other inorganic materials at the nanoscale, an activity that has accelerated considerably over the last decade. Indeed, modify or improve the properties of PB(A)s at the nanometric scale by playing on expected parameters, such as size, surface state, interface, and organization constitute a notable breakthrough, both in the understanding of the fundamental properties of these objects and in the development of their applicative potentials. However, the current needs in many application fields require considering a higher level of complexity involving the provision of different functionalities within the same nano-object, in particular *via* the development of nanoheterostructures, where each component provides one or more functions. This strategy constitutes a fascinating playground for the fundamental study of multifunctional materials with, in certain cases, the appearance of a functional synergy. Indeed, various inorganic materials, including nano-sized metals, metal oxides, silica, carbon materials, QDots, Ln^{3+} based materials, MOFs and POMs, have been associated with PB(A)s at the nanoscale. This type of association requires a good understanding of the phenomena occurring at the interface, which can be of various forms and geometries. Most of the obtained nanoheterostructures can be described as a core@shell morphology, including a simple core@shell, onion-like, yolk@shell geometries with, in some cases, multicore or multishell components. Although it appears to obtain clear evidence of a well-defined heterostructures, in such constructions, the components share large bonding heterointerfaces that may lead to chemical-physical properties distinct from those inherent to the individual components or synergic effects. Depending on the lattice matching between the core and the shell, the association may lead to nanoheterostructures with minimization of misfit strand or to nanoheterostructures presenting polycrystalline or even partially amorphous shell that may even lead in extreme situations to a discontinuous interface between the components called here core@satellites morphology. Note also that the satellites may take different shapes, including spheres, flowers or hairs. Obviously,

the quality features of the different components, as well as the structure of the connecting interfaces, have a profound impact on the ultimate properties. Thus, colloidal strategies to afford such nanoheterostructures reached a high level of synthetic ingenuity.

Among the inorganic components associated at the nanoscale with PB(A)s, noble metals are one of the largest investigated families, the most frequently occurring in the literature being the combination with gold. The latter possesses at the nanoscale exciting properties that can be complementary to PB(A)s, such as SPR, conductivity, redox properties, fluorescence, high electronic density, efficient conversion of light-to-heat, stability and biocompatibility. Apart from gold, PB(A)s were also combined with platinum, palladium, silver or FePt alloy, mainly for the development of their catalytic properties. The richest morphological diversity (Figure 1) can be noted in this group of nanoheterostructures with core@shell (including yolk@shell), core@onion-like multishell, core@satellites and even Janus morphologies. Important progress should be noted in the design resulting in the synthesis of nice nano-objects with well definite components and clearly identified interface.

On the other hand, the investigations of the interface were not yet deeply developed. Only a few works have report on the Au/PB(A)s interface studies by the XPS method and mention the presence of $Au(CN)_n$ species formed on the metallic gold surface, helping the formation of the PBA and assuring the covalent linkage between components. Such studies appear particularly relevant to provide a clear-cut picture of the growth mechanism and interaction between the components to ultimately understand the resulting proprerties.

Another well-represented inorganic component of such nanoheterostructures are metal oxides. Among them, many examples dealt with magnetic metal oxides, such Fe_3O_4, γ-Fe_2O_3, and Co_3O_4, their magnetic properties being highly complementary to PB(A)s' ones. But, few examples of non-magnetic metal oxides and also metal sulfides were also considered, including CeO_2, MnO_2, α-$Co(OH)_2$, CuS, MoS_2 or CoS_2. They bring catalytic or photocatalytic properties, suitable energetic bandgap as quantum dot, or intercalation properties. Of peculiar interest are nanomaterials involving lanthanide ions that are known for displaying remarkable optical properties. Up-conversion nanoparticles and phosphors, such as $NaNdF_4$ or $NaErF_4$@$NaYF_4$@$NaNdF_4$, $NaDyF_4$:*x*%Lu, or $CaMoO_4$:Eu were combined with great success to nanoheterostructures possessing highly interesting optical properties conducting to a great enhancement of PTT and development of theragnostic agents or multifunctional nanoprobes. Molecular nanomaterials, including porphyrins doped MOFs bringing photosensitizing properties or ZIF67 as precursors of metal sulfides and POMs for their photocatalytic properties, were also used as complementary components in nanoheterostructures with PB(A)s. Several examples in the literature also described nice examples of nanoheterostructures, where PB(A)s were combined with silica or PMO in order to benefit from the porosity, stability and easy surface functionalization of these latter. Finally, carbon nanomaterials were other candidates of choice to afford nanoheterostructures as they bring electronic conductivity for Carbon Nanotubes (CNTs) or luminescence properties for Quantum Carbon Dots (QCD).

All those possible chemical combinations at the nanoscale associating PB(A)s with other inorganic components led to nanomaterials with a high degree of multifunctionality that can be exploited in many different applications. PB itself, but also many of its analogues, have been considered as materials in the energy field because of their redox and monocation insertion-disinsertion properties. They, however, suffer from several drawbacks that may be partly

overcome when combining with other inorganic nanoparticles, a strategy that has been explored to develop nanomaterials for supercapacitors, water splitting or batteries. In the field of biosensors, due to their redox and catalytic properties, PB(A)s nanoheterostructures are materials of choice to develop the reactive chemical part constituting the core of the sensitive device in immune- and aptasensors, or H_2O_2 and small molecule detections. At last, the development of the controlled chemistry of PB(A)s at the nanoscale and their combinations with other inorganic nanomaterials have opened a new front of research considering these compounds in the biomedical field. Indeed, Prussian blue itself has been approved by the FDA for the removal of radioactive caesium or thallium from the living body, including human beings, for several decades. But only with its recent developments at the nanometric scale and its integration as a component in nanoheterostructures, these materials have seen a huge development as contrast agents in mono and multimodal imaging, as a therapeutic agent in therapy or as multifunctional agents for theragnostic. The association of complementary properties *via* a sophisticated chemical construction set associating different inorganic components at the nanometric scale, including PB(A)s, allows designing multifunctional nanoheterostructures possessing complementary skills optimizing their efficiency for applicative purposes.

One of the most exciting issues of multifunctionality, interesting not only from the fundamental point of view but also for biomedical applications, is linked with a functional synergy of physical and chemical properties. Very nice examples of a synergic effect achieved through the PTT cross-relaxation mechanism allowing the PTT efficiency enhancement have been demonstrated on core@shell nanoheterostructures combined the PB shell with the lanthanide-doped nanocore. A synergetic effect was also evidenced by designing of PTT/PDT multitherapy agents through the enhancement of photocatalytic properties of porphyrin-MOF based nanomaterial combined with PB by suppressing recombination of electrons and holes, or in tandem, catalysts associating PB in a complex nanoheterostructure with gold and copper oxide to convert H_2O_2 to O_2 and then to $^1O_2$. Moreover, PTT assisted drug delivery was largely developed with the nanoheterostructures associating gold or silica with PB leading to a spectacular increase of therapeutic efficiency and in the tumour growth inhibition effects compared to the ones from separated components.

On the other hand, the simple superposition of the constitutive properties, in the sense where the properties act separately, gives the possibility to associate various types of imaging in the single nanoprobes or combine therapeutic treatment with imaging function, is of key importance in the biomedical area. In this line of thought, an important emphasis has been made to the development of PB(A)s based nanoheterostructures as theragnostic agents combined PTT with different imaging techniques.

The association of PB(A) s with magnetic oxide nanoparticles, for example, allows designing theragnostic nanoparticles combined PTT with MRI, but also to concentrate these nano-objects *via* magnetic targeting within tumours and got a tumour growth inhibition effect close to 100 % for small tumours. Furthermore, other nanoheterostructures involving Au, $NaDyF_4$:x%Lu or MnO_2 components allow a high degree of multifunctionality, sometimes involving an association of PTT/PDT therapeutic function with MRI, PA and CT imaging. The association of phosphors or quantum dots with PB(A)s also afford theragnostic agents with PTT and optical imaging.

After having summarized the recent advancement in the design of PB(A)s based nanoheterostructures, we would like to highlight some future directions in the design of nanoheterostructures. The search for synergistic effects undoubtedly constitutes an extremely attractive and rich field of research where PB(A)s have an important role to play, which is true in many different application fields. In fact, the synergic effect between the PTT properties of Au nano-objects and PB has been announced but totally unexplored, and mechanisms of such a collective action are completely ununderstood. The combined use of the NIR driving the photothermal effect of PB when the latter is associated with noble metals are known for their catalytic properties remains, for example, totally under-exploited. On the other hand, taking advantage of the strong NIR absorption of PB to provide an excitation for NIR emissive Ln^{3+} (Nd^{3+}, Yb^{3+}, Er^{3+}), particularly relavant for optical imaging, have not been exploited yet. This requires understanding the electronic structure levels to provide efficient sensitize paths. In the field of sensors, PB, due to its redox properties, was shown at the nanoscale to mimic enzymes. Thus, its association with magnetic components in nanoheterostructures could give access to the building of devices for immunosensors, for which the enzymatic activity could be assured by PB itself. It could be also emphasized that some PB(A) analogues exhibit various temperature or ligh-induced phase transition or electron transfer. Their combination with others materials to study the mutual interaction and develop advanced synergestic devices have been rarely explored.

More generally, the development of nanoheterostructures, including PB(A)s as a sensitive layer for developing small molecule sensors using their electrochromic properties with chemical selectivity by taking advantage of the porosity of these materials, also remains largely unexploited. And these are just a few examples of the potential of nanoheterostructures, including Prussian blue, which, although already the subject of numerous studies, will continue to be the subject of intensive contemporary research.

Acknowledgements

The authors thank the University of Montpellier and CNRS. This work has been supported by the French National Research Agency (ANR) with grant number ANR-18-CE09-0012-01 in the frame of the NANOBLUE project.

References

[1] L. Jing, S.V. Kershaw, Y. Li, X. Huang, Y. Li, A.L. Rogach, M. Gao, Chemical Reviews, 116 (2016) 10623-10730.
[2] A. Teitelboim, N. Meir, M. Kazes, D. Oron, Accounts of Chemical Research, 49 (2016) 902-910.
[3] D. Vasudevan, R.R. Gaddam, A. Trinchi, I. Cole, Journal of Alloys and Compounds, 636 (2015) 395-404.
[4] M. Volokh, T. Mokari, Nanoscale Advances, 2 (2020) 930-961.
[5] Y. Lv, S. Duan, R. Wang, Progress in Natural Science: Materials International, 30 (2020) 1-12.
[6] R. Jiang, B. Li, C. Fang, J. Wang, Advanced Materials, 26 (2014) 5274-5309.
[7] K. Loza, M. Heggen, M. Epple, Advanced Functional Materials, 30 (2020) 1909260.
[8] H. Zhang, S. Duan, P.M. Radjenovic, Z.-Q. Tian, J.-F. Li, Accounts of Chemical Research, 53 (2020) 729-739.
[9] M. Ha, J.-H. Kim, M. You, Q. Li, C. Fan, J.-M. Nam, Chemical Reviews, 119 (2019) 12208-12278.
[10] Z.-c. Zhang, B. Xu, X. Wang, Chemical Society Reviews, 43 (2014) 7870-7886.
[11] C. Hanske, M.N. Sanz-Ortiz, L.M. Liz-Marzán, Advanced Materials, 30 (2018) 1707003.

[12] E. Bagheri, L. Ansari, K. Abnous, S.M. Taghdisi, P. Ramezani, M. Ramezani, M. Alibolandi, Critical Reviews in Analytical Chemistry, (2020) 1-22.
[13] S.P. Moulik, G.C. De, A.K. Panda, B.B. Bhowmik, A.R. Das, Langmuir, 15 (1999) 8361-8367.
[14] S. Vaucher, M. Li, S. Mann, Angewandte Chemie International Edition, 39 (2000) 1793-1796.
[15] Prussian Blue-Type Nanoparticles and Nanocomposites: Synthesis, Devices, and Applications, Jenny Stanford Publishing, New York, 2019.
[16] J.-D. Qiu, H.-Z. Peng, R.-P. Liang, J. Li, X.-H. Xia, Langmuir, 23 (2007) 2133-2137.
[17] G. Fornasieri, A. Bordage, A. Bleuzen, European Journal of Inorganic Chemistry, 2018 (2018) 259-271.
[18] T. Vincent, C. Vincent, E. Guibal, Molecules, 20 (2015) 20582-20613.
[19] V.D. Ivanov, Ionics, 26 (2020) 531-547.
[20] C. Maerten, L. Jierry, P. Schaaf, F. Boulmedais, ACS Applied Materials & Interfaces, 9 (2017) 28117-28138.
[21] A. Kraft, The history of Prussian blue, in: Y. Guari, J. Larionova (Eds.) Prussian Blue-Type Nanoparticles and Nanocomposites: Synthesis, Devices, and Applications, Jenny Stanford Publishing, New York, 2019, pp. 1-26.
[22] A. Simonov, T. De Baerdemaeker, H.L.B. Boström, M.L. Ríos Gómez, H.J. Gray, D. Chernyshov, A. Bosak, H.-B. Bürgi, A.L. Goodwin, Nature, 578 (2020) 256-260.
[23] B. Singh, A. Indra, Materials Today Energy, 16 (2020) 100404.
[24] M.J. Piernas Muñoz, E. Castillo Martínez, Prussian Blue and Its Analogues. Structure, Characterization and Applications, in: Prussian Blue Based Batteries, Springer International Publishing, Cham, 2018, pp. 9-22.
[25] B. Kong, C. Selomulya, G. Zheng, D. Zhao, Chemical Society Reviews, 44 (2015) 7997-8018.
[26] D.R. Melo, J.L. Lipsztein, R. Leggett, L. Bertelli, R. Guilmette, Health Physics, 106 (2014) 592-597.
[27] Electrochromic Materials Based on Prussian Blue and Other Metal Metallohexacyanates, in: Electrochromic Materials and Devices, 2013, pp. 41-56.
[28] S. Wang, X.-H. Ding, Y.-H. Li, W. Huang, Coordination Chemistry Reviews, 256 (2012) 439-464.
[29] S.-i. Ohkoshi, H. Tokoro, Accounts of Chemical Research, 45 (2012) 1749-1758.
[30] D.R. Talham, M.W. Meisel, Chemical Society Reviews, 40 (2011) 3356-3365.
[31] Y. Lin, L. Zhang, Y. Xiong, T. Wei, Z. Fan, ENERGY & ENVIRONMENTAL MATERIALS, n/a.
[32] R. Zboril, L. Machala, M. Mashlan, V. Sharma, Crystal Growth & Design, 4 (2004) 1317-1325.
[33] L. Boudjema, E. Mamontova, J. Long, J. Larionova, Y. Guari, P. Trens, Inorganic Chemistry, 56 (2017) 7598-7601.
[34] https://base-donnees-publique.medicaments.gouv.fr/affichageDoc.php?specid=65903335&typedoc=N.
[35] S. Vaucher, J. Fielden, M. Li, E. Dujardin, S. Mann, Nano Letters, 2 (2002) 225-229.
[36] L. Catala, T. Gacoin, J.-P. Boilot, É. Rivière, C. Paulsen, E. Lhotel, T. Mallah, Advanced Materials, 15 (2003) 826-829.
[37] M.F. Dumont, O.N. Risset, E.S. Knowles, T. Yamamoto, D.M. Pajerowski, M.W. Meisel, D.R. Talham, Inorganic Chemistry, 52 (2013) 4494-4501.
[38] D.H.M. Buchold, C. Feldmann, Chemistry of Materials, 19 (2007) 3376-3380.
[39] A. Kraft, Ionics, 27 (2021) 2289-2305.
[40] X. Wang, L. Cheng, Coordination Chemistry Reviews, 419 (2020) 213393.
[41] P. Rauwel, E. Rauwel, Nanomaterials, 9 (2019) 682.
[42] Y. Li, J. Hu, K. Yang, B. Cao, Z. Li, L. Yang, F. Pan, Materials Today Energy, 14 (2019) 100332.
[43] A. Azhar, Y. Li, Z. Cai, M.B. Zakaria, M.K. Masud, M.S.A. Hossain, J. Kim, W. Zhang, J. Na, Y. Yamauchi, M. Hu, Bulletin of the Chemical Society of Japan, 92 (2019) 875-904.
[44] Y. Zhao, W. Zhang, M. Hu, ChemNanoMat, 3 (2017) 780-789.
[45] M.B. Zakaria, T. Chikyow, Coordination Chemistry Reviews, 352 (2017) 328-345.
[46] L. Catala, T. Mallah, Coordination Chemistry Reviews, 346 (2017) 32-61.
[47] J. Larionova, Y. Guari, C. Sangregorio, C. Guérin, New Journal of Chemistry, 33 (2009) 1177-1190.

[48] A. Gotoh, H. Uchida, M. Ishizaki, T. Satoh, S. Kaga, S. Okamoto, M. Ohta, M. Sakamoto, T. Kawamoto, H. Tanaka, M. Tokumoto, S. Hara, H. Shiozaki, M. Yamada, M. Miyake, M. Kurihara, Nanotechnology, 18 (2007) 345609.
[49] G. Clavel, J. Larionova, Y. Guari, C. Guérin, Chemistry – A European Journal, 12 (2006) 3798-3804.
[50] J. Larionova, Y. Guari, A. Tokarev, E. Chelebaeva, C. Luna, C. Sangregorio, A. Caneschi, C. Guérin, Inorganica Chimica Acta, 361 (2008) 3988-3996.
[51] J. Larionova, Y. Guari, C. Blanc, P. Dieudonné, A. Tokarev, C. Guérin, Langmuir, 25 (2009) 1138-1147.
[52] Q. Wang, N. Wang, S. He, J. Zhao, J. Fang, W. Shen, Dalton Transactions, 44 (2015) 12878-12883.
[53] T. Uemura, S. Kitagawa, Journal of the American Chemical Society, 125 (2003) 7814-7815.
[54] F. Frye, A., D. Pajerowski, M., N. Anderson, E., J. Long, J.-H. Park, M. Meisel, W., D. Talham, R., Polyhedron, 26 (2007) 2273.
[55] L. Catala, A. Gloter, O. Stephan, G. Rogez, T. Mallah, Chemical Communications, (2006) 1018-1020.
[56] G.-Z. Deng, L.-X. Zhong, Y.-Q. Sun, Z.-Y. Liu, Q. Wang, D.-Z. Gao, G.-Y. Zhang, Y.-Y. Xu, Journal of Solid State Chemistry, 268 (2018) 175-181.
[57] S. Mukherjee, R. Kotcherlakota, S. Haque, S. Das, S. Nuthi, D. Bhattacharya, K. Madhusudana, S. Chakravarty, R. Sistla, C.R. Patra, ACS Biomaterials Science & Engineering, 6 (2020) 690-704.
[58] D. Brinzei, L. Catala, C. Mathonière, W. Wernsdorfer, A. Gloter, O. Stephan, T. Mallah, Journal of the American Chemical Society, 129 (2007) 3778-3779.
[59] T. Uemura, M. Ohba, S. Kitagawa, Inorganic Chemistry, 43 (2004) 7339-7345.
[60] M. Perrier, S. Kenouche, J. Long, K. Thangavel, J. Larionova, C. Goze-Bac, A. Lascialfari, M. Mariani, N. Baril, C. Guérin, B. Donnadieu, A. Trifonov, Y. Guari, Inorganic Chemistry, 52 (2013) 13402-13414.
[61] V.S. Perera, G. Chen, Q. Cai, S.D. Huang, Analyst, 141 (2016) 2016-2022.
[62] A. Sahu, J.H. Lee, H.G. Lee, Y.Y. Jeong, G. Tae, Journal of Controlled Release, 236 (2016) 90-99.
[63] M. Hu, S. Ishihara, K. Ariga, M. Imura, Y. Yamauchi, Chemistry – A European Journal, 19 (2013) 1882-1885.
[64] M. Shokouhimehr, E.S. Soehnlen, A. Khitrin, S. Basu, S.D. Huang, Inorganic Chemistry Communications, 13 (2010) 58-61.
[65] M. Shokouhimehr, E.S. Soehnlen, J. Hao, M. Griswold, C. Flask, X. Fan, J.P. Basilion, S. Basu, S.D. Huang, Journal of Materials Chemistry, 20 (2010) 5251-5259.
[66] L. Cheng, H. Gong, W. Zhu, J. Liu, X. Wang, G. Liu, Z. Liu, Biomaterials, 35 (2014) 9844-9852.
[67] Z. Li, Y. Zeng, D. Zhang, M. Wu, L. Wu, A. Huang, H. Yang, X. Liu, J. Liu, Journal of Materials Chemistry B, 2 (2014) 3686-3696.
[68] Z. Farka, V. Čunderlová, V. Horáčková, M. Pastucha, Z. Mikušová, A. Hlaváček, P. Skládal, Analytical Chemistry, 90 (2018) 2348-2354.
[69] D. Brinzei, L. Catala, G. Rogez, A. Gloter, T. Mallah, Inorganica Chimica Acta, 361 (2008) 3931-3936.
[70] D. Dedovets, P. Bauduin, J. Causse, L. Girard, O. Diat, Physical Chemistry Chemical Physics, 18 (2016) 3188-3196.
[71] J. Liang, C.H. Li, D.R. Talham, Crystal Growth & Design, 20 (2020) 2713-2720.
[72] H. Ming, N.L.K. Torad, Y.-D. Chiang, K.C.W. Wu, Y. Yamauchi, CrystEngComm, 14 (2012) 3387-3396.
[73] W.-P. Li, C.-H. Su, L.-C. Tsao, C.-T. Chang, Y.-P. Hsu, C.-S. Yeh, ACS Nano, 10 (2016) 11027-11036.
[74] J. Li, X. Liu, L. Tan, Z. Cui, X. Yang, Y. Liang, Z. Li, S. Zhu, Y. Zheng, K.W.K. Yeung, X. Wang, S. Wu, Nature Communications, 10 (2019) 4490.
[75] X.-J. Zheng, Q. Kuang, T. Xu, Z.-Y. Jiang, S.-H. Zhang, Z.-X. Xie, R.-B. Huang, L.-S. Zheng, The Journal of Physical Chemistry C, 111 (2007) 4499-4502.
[76] S. Xu, X. Qian, G. Li, Materials Research Bulletin, 43 (2008) 135-140.
[77] M. Hu, S. Furukawa, R. Ohtani, H. Sukegawa, Y. Nemoto, J. Reboul, S. Kitagawa, Y. Yamauchi, Angewandte Chemie International Edition, 51 (2012) 984-988.

[78] J. Long, Y. Guari, C. Guérin, J. Larionova, Dalton Transactions, 45 (2016) 17581-17587.
[79] Y. Guari, & Larionova, J. (Eds.). Jenny Stanford Publishing. , (2019).
[80] Z. Qin, Y. Li, N. Gu, Advanced Healthcare Materials, 7 (2018) 1800347.
[81] M. Gautam, K. Poudel, C.S. Yong, J.O. Kim, International Journal of Pharmaceutics, 549 (2018) 31-49.
[82] L. Zou, H. Wang, B. He, L. Zeng, T. Tan, H. Cao, X. He, Z. Zhang, S. Guo, Y. Li, Theranostics, 6 (2016) 762-772.
[83] V. Shanmugam, S. Selvakumar, C.-S. Yeh, Chemical Society Reviews, 43 (2014) 6254-6287.
[84] A.M. Alkilany, L.B. Thompson, S.P. Boulos, P.N. Sisco, C.J. Murphy, Advanced Drug Delivery Reviews, 64 (2012) 190-199.
[85] H. Kim, K. Chung, S. Lee, D.H. Kim, H. Lee, WIREs Nanomedicine and Nanobiotechnology, 8 (2016) 23-45.
[86] H.A. Hoffman, L. Chakrabarti, M.F. Dumont, A.D. Sandler, R. Fernandes, RSC Advances, 4 (2014) 29729-29734.
[87] L.M.A. Ali, E. Mathlouthi, M. Cahu, S. Sene, M. Daurat, J. Long, Y. Guari, F. Salles, J. Chopineau, J.-M. Devoisselle, J. Larionova, M. Gary-Bobo, RSC Advances, 10 (2020) 2646-2649.
[88] L.M.A. Ali, E. Mathlouthi, M. Kajdan, M. Daurat, J. Long, R. Sidi-Boulenouar, M. Cardoso, C. Goze-Bac, N. Amdouni, Y. Guari, J. Larionova, M. Gary-Bobo, Photodiagnosis and Photodynamic Therapy, 22 (2018) 65-69.
[89] E.E. Sweeney, J. Cano-Mejia, R. Fernandes, Small, 14 (2018) 1800678.
[90] M.A. Busquets, J. Estelrich, Drug Discovery Today, 25 (2020) 1431-1443.
[91] P. Shou, Z. Yu, Y. Wu, Q. Feng, B. Zhou, J. Xing, C. Liu, J. Tu, O.U. Akakuru, Z. Ye, X. Zhang, Z. Lu, L. Zhang, A. Wu, Advanced Healthcare Materials, 9 (2020) 1900948.
[92] X. Chen, G. Wu, J. Tang, L. Zhou, S. Wei, Inorganic Chemistry Communications, 114 (2020) 107821.
[93] J. Cano-Mejia, R.A. Burga, E.E. Sweeney, J.P. Fisher, C.M. Bollard, A.D. Sandler, C.R.Y. Cruz, R. Fernandes, Nanomedicine: Nanotechnology, Biology and Medicine, 13 (2017) 771-781.
[94] P. Xue, K.K.Y. Cheong, Y. Wu, Y. Kang, Colloids and Surfaces B: Biointerfaces, 125 (2015) 277-283.
[95] M. Wu, Q. Wang, X. Liu, J. Liu, RSC Advances, 5 (2015) 30970-30980.
[96] X. Cai, X. Jia, W. Gao, K. Zhang, M. Ma, S. Wang, Y. Zheng, J. Shi, H. Chen, Advanced Functional Materials, 25 (2015) 2520-2529.
[97] L. Jing, s. shao, Y. Wang, Y. Yang, X. Yue, Z. Dai, Theranostics, 6 (2016) 40-53.
[98] X.-D. Li, X.-L. Liang, F. Ma, L.-J. Jing, L. Lin, Y.-B. Yang, S.-S. Feng, G.-L. Fu, X.-L. Yue, Z.-F. Dai, Colloids and Surfaces B: Biointerfaces, 123 (2014) 629-638.
[99] X. Liang, Z. Deng, L. Jing, X. Li, Z. Dai, C. Li, M. Huang, Chemical Communications, 49 (2013) 11029-11031.
[100] C.P.L.A. (Eds), Springer Milan, (2019).
[101] A.H.L. Merbach, Toth, E. (Eds), A John Wiley & Sons, Ltd., Publication, (2013).
[102] P. Caravan, J.J. Ellison, T.J. McMurry, R.B. Lauffer, Chemical Reviews, 99 (1999) 2293-2352.
[103] M.F. Dumont, S. Yadavilli, R.W. Sze, J. Nazarian, R. Fernandes, Int J Nanomedicine, 9 (2014) 2581-2595.
[104] W. Zhu, K. Liu, X. Sun, X. Wang, Y. Li, L. Cheng, Z. Liu, ACS Applied Materials & Interfaces, 7 (2015) 11575-11582.
[105] G. Paul, Y. Prado, N. Dia, E. Rivière, S. Laurent, M. Roch, L.V. Elst, R.N. Muller, L. Sancey, P. Perriat, O. Tillement, T. Mallah, L. Catala, Chemical Communications, 50 (2014) 6740-6743.
[106] Y. Li, C.H. Li, D.R. Talham, Nanoscale, 7 (2015) 5209-5216.
[107] N.L. Torad, M. Hu, M. Imura, M. Naito, Y. Yamauchi, Journal of Materials Chemistry, 22 (2012) 18261-18267.
[108] J.-Y. Hong, W.-K. Oh, K.-Y. Shin, O.S. Kwon, S. Son, J. Jang, Biomaterials, 33 (2012) 5056-5066.
[109] C. Timchalk, J.A. Creim, V. Sukwarotwat, R. Wiacek, R.S. Addleman, G.E. Fryxell, W. Yantasee, Health physics, 99 (2010) 420-429.

[110] C. Lavaud, M. Kajdan, E. Compte, J.-C. Maurel, J. Lai Kee Him, P. Bron, E. Oliviero, J. Long, J. Larionova, Y. Guari, New Journal of Chemistry, 41 (2017) 2887-2890.
[111] S. Ferlay, T. Mallah, R. Ouahès, P. Veillet, M. Verdaguer, Nature, 378 (1995) 701-703.
[112] S.M. Holmes, G.S. Girolami, Journal of the American Chemical Society, 121 (1999) 5593-5594.
[113] M. Verdaguer, G.S. Girolami, Magnetic Prussian Blue Analogs, in: Magnetism: Molecules to Materials V, 2004, pp. 283-346.
[114] O.E. Khan, VCH Publishers, Inc., (1993).
[115] A. Weiss, Berichte der Bunsengesellschaft für physikalische Chemie, 68 (1964) 996-996.
[116] R. Koncki, Critical Reviews in Analytical Chemistry, 32 (2002) 79-96.
[117] D.J. Schmidt, F.Ç. Cebeci, Z.I. Kalcioglu, S.G. Wyman, C. Ortiz, K.J. Van Vliet, P.T. Hammond, ACS Nano, 3 (2009) 2207-2216.
[118] F. Scholz, A. Doménech-Carbó, Angewandte Chemie International Edition, 58 (2019) 3279-3284.
[119] Y. Matos-Peralta, M. Antuch, Journal of The Electrochemical Society, 167 (2019) 037510.
[120] A.A. Karyakin, Electroanalysis, 13 (2001) 813-819.
[121] K. Hurlbutt, S. Wheeler, I. Capone, M. Pasta, Joule, 2 (2018) 1950-1960.
[122] J. Qian, C. Wu, Y. Cao, Z. Ma, Y. Huang, X. Ai, H. Yang, Advanced Energy Materials, 8 (2018) 1702619.
[123] M. Okubo, J. Long, D.R. Talham, R. Lescouëzec, Comptes Rendus Chimie, 22 (2019) 483-489.
[124] J. Qian, C. Wu, Y. Cao, Z. Ma, Y. Huang, X. Ai, H. Yang, Advanced Energy Materials, 8 (2018) 1870079.
[125] A. Firouzi, R. Qiao, S. Motallebi, C.W. Valencia, H.S. Israel, M. Fujimoto, L.A. Wray, Y.-D. Chuang, W. Yang, C.D. Wessells, Nature Communications, 9 (2018) 861.
[126] B. Wang, Y. Han, X. Wang, N. Bahlawane, H. Pan, M. Yan, Y. Jiang, iScience, 3 (2018) 110-133.
[127] A. Mauger, C.M. Julien, Materials, 13 (2020) 3453.
[128] W. Zhang, S. Hu, J.-J. Yin, W. He, W. Lu, M. Ma, N. Gu, Y. Zhang, Journal of the American Chemical Society, 138 (2016) 5860-5865.
[129] P. Lu, S. Liu, G. Dai, Y. Lei, Y. Liang, Australian Journal of Chemistry, 66 (2013) 983-988.
[130] Z. Hassanvand, F. JALALI, ANALYTICAL AND BIOANALYTICAL CHEMISTRY RESEARCH, 5 (2018) -.
[131] J.C. Kemmegne-Mbouguen, L. Angnes, E. Mouafo-Tchinda, E. Ngameni, Electroanalysis, 27 (2015) 2387-2398.
[132] N. Vishnu, A.S. Kumar, S. Badhulika, Journal of Electroanalytical Chemistry, 837 (2019) 60-66.
[133] X. Wang, W. Tan, H. Ji, F. Liu, D. Wu, J. Ma, Y. Kong, Sensors and Actuators B: Chemical, 264 (2018) 240-248.
[134] Y. Yang, Y. Yan, X. Chen, W. Zhai, Y. Xu, Y. Liu, Electrocatalysis, 5 (2014) 344-353.
[135] J. Zhao, J. Liu, S. Tricard, L. Wang, Y. Liang, L. Cao, J. Fang, W. Shen, Electrochimica Acta, 171 (2015) 121-127.
[136] W. Guo, J. Ma, X. Cao, X. Tong, F. Liu, Y. Liu, Z. Zhang, S. Liu, Microchimica Acta, 184 (2017) 3163-3170.
[137] R.A.A. Munoz, D. Lu, A. Cagan, J. Wang, Analyst, 132 (2007) 560-565.
[138] D. Lu, A. Cagan, R.A.A. Munoz, T. Tangkuaram, J. Wang, Analyst, 131 (2006) 1279-1281.
[139] X. Luo, J. Pan, K. Pan, Y. Yu, A. Zhong, S. Wei, J. Li, J. Shi, X. Li, Journal of Electroanalytical Chemistry, 745 (2015) 80-87.
[140] D.R. Do Carmo, P.F.P. Barbosa, L.R. Cumba, Silicon, 12 (2020) 1111-1123.
[141] W.-R. Cai, G.-Y. Zhang, T. Song, X.-J. Zhang, D. Shan, Electrochimica Acta, 198 (2016) 32-39.
[142] É.N. Oiye, N.B.d. Figueiredo, J.F.d. Andrade, H.M. Tristão, M.F.d. Oliveira, Forensic Science International, 192 (2009) 94-97.
[143] L. Lü, Analytical sciences : the international journal of the Japan Society for Analytical Chemistry, 36 (2020) 127-133.
[144] P.R.d. Oliveira, M.M. Oliveira, A.J.G. Zarbin, L.H. Marcolino-Junior, M.F. Bergamini, Sensors and Actuators B: Chemical, 171-172 (2012) 795-802.

[145] Y. Li, Q. Dang, W. Chen, L. Tang, M. Hu, Journal of Inorganic and Organometallic Polymers and Materials, 31 (2021) 1877-1893.
[146] Y. Wang, S. Chen, J. Zhang, Advanced Functional Materials, 29 (2019) 1904955.
[147] Z. Chu, Y. Liu, W. Jin, Biosensors and Bioelectronics, 96 (2017) 17-25.
[148] E. Y. Jomma, N. Bao, S.-N. Ding, Current Analytical Chemistry, 12 (2016) 512-522.
[149] O.N. Risset, D.R. Talham, Chemistry of Materials, 27 (2015) 3838-3843.
[150] P. Bhatt, S. Banerjee, S. Anwar, M.D. Mukadam, S.S. Meena, S.M. Yusuf, ACS Applied Materials & Interfaces, 6 (2014) 17579-17588.
[151] M. Okubo, C.H. Li, D.R. Talham, Chemical Communications, 50 (2014) 1353-1355.
[152] X. Cai, W. Gao, M. Ma, M. Wu, L. Zhang, Y. Zheng, H. Chen, J. Shi, Advanced Materials, 27 (2015) 6382-6389.
[153] S.P.S. Shaikh, P. Bhatt, S.M. Yusuf, S.N. Bhange, S. Bansod, A.M. Abdalla, International Journal of Hydrogen Energy, 45 (2020) 15317-15326.
[154] L. Catala, D. Brinzei, Y. Prado, A. Gloter, O. Stéphan, G. Rogez, T. Mallah, Angewandte Chemie International Edition, 48 (2009) 183-187.
[155] F. Li, W. Zhang, A. Carné-Sánchez, Y. Tsujimoto, S. Kitagawa, S. Furukawa, M. Hu, Inorganic Chemistry, 57 (2018) 8701-8704.
[156] M.K. Peprah, D. VanGennep, P.A. Quintero, O.N. Risset, T.V. Brinzari, C.H. Li, M.F. Dumont, J.-s. Xia, J.J. Hamlin, D.R. Talham, M.W. Meisel, Polyhedron, 123 (2017) 323-327.
[157] M.F. Dumont, E.S. Knowles, A. Guiet, D.M. Pajerowski, A. Gomez, S.W. Kycia, M.W. Meisel, D.R. Talham, Inorganic Chemistry, 50 (2011) 4295-4300.
[158] A.C. Felts, A. Slimani, J.M. Cain, M.J. Andrus, A.R. Ahir, K.A. Abboud, M.W. Meisel, K. Boukheddaden, D.R. Talham, Journal of the American Chemical Society, 140 (2018) 5814-5824.
[159] A. Bordage, R. Moulin, E. Fonda, G. Fornasieri, E. Rivière, A. Bleuzen, Journal of the American Chemical Society, 140 (2018) 10332-10343.
[160] M. Presle, J. Lemainque, J.M. Guigner, E. Larquet, I. Maurin, J.P. Boilot, T. Gacoin, New Journal of Chemistry, 35 (2011) 1296-1301.
[161] D. Asakura, C.H. Li, Y. Mizuno, M. Okubo, H. Zhou, D.R. Talham, Journal of the American Chemical Society, 135 (2013) 2793-2799.
[162] C.-H. Lee, C.-M. Wu, E. Batsaikhan, H.-C. Li, C.H. Li, M.K. Peprah, D.R. Talham, M.W. Meisel, W.-H. Li, The Journal of Physical Chemistry C, 119 (2015) 29138-29147.
[163] O.N. Risset, E.S. Knowles, S. Ma, M.W. Meisel, D.R. Talham, Chemistry of Materials, 25 (2013) 42-47.
[164] Y. Yin, Q. Li, S. Ma, H. Liu, B. Dong, J. Yang, D. Liu, Analytical Chemistry, 89 (2017) 1551-1557.
[165] G. Maurin-Pasturel, J. Long, Y. Guari, F. Godiard, M.-G. Willinger, C. Guerin, J. Larionova, Angewandte Chemie International Edition, 53 (2014) 3872-3876.
[166] G. Maurin-Pasturel, J. Long, M.A. Palacios, C. Guérin, C. Charnay, M.-G. Willinger, A.A. Trifonov, J. Larionova, Y. Guari, Chemistry – A European Journal, 23 (2017) 7483-7496.
[167] G. Maurin-Pasturel, E. Rascol, M. Busson, S. Sevestre, J. Lai-Kee-Him, P. Bron, J. Long, J. Chopineau, J.-M. Devoisselle, Y. Guari, J. Larionova, Inorganic Chemistry Frontiers, 4 (2017) 1737-1741.
[168] G. Maurin-Pasturel, E. Mamontova, M.A. Palacios, J. Long, J. Allouche, J.-C. Dupin, Y. Guari, J. Larionova, Dalton Transactions, 48 (2019) 6205-6216.
[169] M. Zhang, W. Zhang, C. Engelbrekt, C. Hou, N. Zhu, Q. Chi, ChemElectroChem, 7 (2020) 3818-3823.
[170] F.E. Wagner, S. Haslbeck, L. Stievano, S. Calogero, Q.A. Pankhurst, K.P. Martinek, Nature, 407 (2000) 691-692.
[171] M. Faraday, Philosophical Transactions of the Royal Society of London, 147 (1857) 145-181.
[172] B. Zhu, S. Gong, W. Cheng, Chemical Society Reviews, 48 (2019) 1668-1711.
[173] M. Stratakis, H. Garcia, Chemical Reviews, 112 (2012) 4469-4506.
[174] K. Sztandera, M. Gorzkiewicz, B. Klajnert-Maculewicz, Molecular Pharmaceutics, 16 (2019) 1-23.

[175] L. Qin, G. Zeng, C. Lai, D. Huang, P. Xu, C. Zhang, M. Cheng, X. Liu, S. Liu, B. Li, H. Yi, Coordination Chemistry Reviews, 359 (2018) 1-31.
[176] J.K. Stolarczyk, S. Bhattacharyya, L. Polavarapu, J. Feldmann, ACS Catalysis, 8 (2018) 3602-3635.
[177] N.C. Bigall, W.J. Parak, D. Dorfs, Nano Today, 7 (2012) 282-296.
[178] F. Ricci, G. Palleschi, Biosensors and Bioelectronics, 21 (2005) 389-407.
[179] L. Jing, X. Liang, Z. Deng, S. Feng, X. Li, M. Huang, C. Li, Z. Dai, Biomaterials, 35 (2014) 5814-5821.
[180] M. Zhang, A. Halder, C. Hou, J. Ulstrup, Q. Chi, Bioelectrochemistry, 109 (2016) 87-94.
[181] P.C. Pandey, D. Panday, G. Pandey, RSC Advances, 4 (2014) 60563-60572.
[182] J. Zhang, W. Yang, H. Zhu, J. Li, F. Yang, B. Zhang, X. Yang, Journal of Colloid and Interface Science, 338 (2009) 319-324.
[183] J. Zhang, J. Li, F. Yang, B. Zhang, X. Yang, Sensors and Actuators B: Chemical, 143 (2009) 373-380.
[184] W. Zhu, M.-Y. Gao, Q. Zhu, B. Chi, L.-W. Zeng, J.-M. Hu, A.-G. Shen, Nanoscale, 12 (2020) 3292-3301.
[185] Y.-M. Shen, M.-Y. Gao, X. Chen, A.-G. Shen, J.-M. Hu, Spectrochimica Acta Part A: Molecular and Biomolecular Spectroscopy, 252 (2021) 119566.
[186] C. Zhang, Z. Xu, H. Di, E. Zeng, Y. Jiang, D. Liu, Theranostics, 10 (2020) 6061-6071.
[187] X. Gao, Y. Yin, H. Wu, Z. Hao, J. Li, S. Wang, Y. Liu, Analytical Chemistry, 93 (2021) 1569-1577.
[188] R. Purbia, S. Paria, Nanoscale, 7 (2015) 19789-19873.
[189] L. Hang, H. Li, T. Zhang, D. Men, C. Zhang, P. Gao, Q. Zhang, ACS Applied Materials & Interfaces, 11 (2019) 39493-39502.
[190] P. Yang, J. Peng, Z. Chu, D. Jiang, W. Jin, Biosensors and Bioelectronics, 92 (2017) 709-717.
[191] Z.-Y. Liu, G.-T. Fu, L. Zhang, X.-Y. Yang, Z.-Q. Liu, D.-M. Sun, L. Xu, Y.-W. Tang, Scientific Reports, 6 (2016) 32402.
[192] Y. Miao, J. Chen, X. Wu, J. Miao, Colloids and Surfaces A: Physicochemical and Engineering Aspects, 295 (2007) 135-138.
[193] C. Ou, S. Chen, R. Yuan, Y. Chai, X. Zhong, Journal of Electroanalytical Chemistry, 624 (2008) 287-292.
[194] R. Li, R. Li, C. Wang, L. Gao, Q. Chen, Dalton Transactions, 45 (2016) 539-544.
[195] J. Guo, X. Zhang, Y. Sun, L. Tang, Q. Liu, X. Zhang, ACS Sustainable Chemistry & Engineering, 5 (2017) 11577-11583.
[196] X. Zhang, P. Liu, Y. Sun, T. Zhan, Q. Liu, L. Tang, J. Guo, Y. Xia, Inorganic Chemistry Frontiers, 5 (2018) 1683-1689.
[197] Z. Hu, S. Wang, Z. Dai, H. Zhang, X. Zheng, Journal of Materials Chemistry B, 8 (2020) 5351-5360.
[198] E. Mamontova, M. Rodríguez-Castillo, E. Oliviero, Y. Guari, J. Larionova, M. Monge, J. Long, Inorganic Chemistry Frontiers, 8 (2021) 2248-2260.
[199] R. Sanchis-Gual, I. Susic, R. Torres-Cavanillas, D. Arenas-Esteban, S. Bals, T. Mallah, M. Coronado-Puchau, E. Coronado, Chemical Communications, 57 (2021) 1903-1906.
[200] Y. Dou, X. Li, W. Yang, Y. Guo, M. Wu, Y. Liu, X. Li, X. Zhang, J. Chang, ACS Applied Materials & Interfaces, 9 (2017) 1263-1272.
[201] J. Han, Y. Zhuo, Y. Chai, R. Yuan, W. Zhang, Q. Zhu, Analytica Chimica Acta, 746 (2012) 70-76.
[202] J. Han, Y. Zhuo, Y. Chai, R. Yuan, Y. Xiang, Q. Zhu, N. Liao, Biosensors and Bioelectronics, 46 (2013) 74-79.
[203] Z. Hu, Z. Dai, X. Hu, K. Chen, C. Gao, X. Zheng, Y. Yu, Analytical Methods, 11 (2019) 677-683.
[204] D. Li, A. Bao, X. Chen, S. Li, T. Wang, L. Zhang, J. Ji, Q. Li, C. Wang, Y. Gao, Y. Yang, X. Dong, Advanced Therapeutics, 3 (2020) 2000091.
[205] T. Zheng, T. Zhou, X. Feng, J. Shen, M. Zhang, Y. Sun, ACS Applied Materials & Interfaces, 11 (2019) 31615-31626.
[206] R. Massart, IEEE Transactions on Magnetics, 17 (1981) 1247-1248.
[207] Y. Zhuo, P.-X. Yuan, R. Yuan, Y.-Q. Chai, C.-L. Hong, Biomaterials, 30 (2009) 2284-2290.

[208] C.L. C. Carvalho, A.T. B. Silva, R.A.S. Luz, G.M.B. Castro, C. da Luz Lima, V.R. Mastelaro, R.R. da Silva, O.N. Oliveira, W. Cantanhêde, ACS Applied Nano Materials, 1 (2018) 4283-4293.
[209] G. Fu, W. Liu, Y. Li, Y. Jin, L. Jiang, X. Liang, S. Feng, Z. Dai, Bioconjugate Chemistry, 25 (2014) 1655-1663.
[210] P. Xue, J. Bao, Y. Wu, Y. Zhang, Y. Kang, RSC Advances, 5 (2015) 28401-28409.
[211] S.S. Kale, R.A. Burga, E.E. Sweeney, Z. Zun, R.W. Sze, A. Tuesca, J.A. Subramony, R. Fernandes, in: Int J Nanomedicine, 2017, pp. 6413-6424.
[212] Y. Yang, L. Jing, X. Li, L. Lin, X. Yue, Z. Dai, Theranostics, 7 (2017) 466-481.
[213] P. Xue, L. Sun, Q. Li, L. Zhang, Z. Xu, C.M. Li, Y. Kang, Journal of Colloid and Interface Science, 509 (2018) 384-394.
[214] Y. Wang, X. Pang, J. Wang, Y. Cheng, Y. Song, Q. Sun, Q. You, F. Tan, J. Li, N. Li, Journal of Materials Chemistry B, 6 (2018) 2460-2473.
[215] X.-Q. Zhang, S.-W. Gong, Y. Zhang, T. Yang, C.-Y. Wang, N. Gu, Journal of Materials Chemistry, 20 (2010) 5110-5116.
[216] M. Magro, D. Baratella, G. Salviulo, K. Polakova, G. Zoppellaro, J. Tucek, J. Kaslik, R. Zboril, F. Vianello, Biosensors and Bioelectronics, 52 (2014) 159-165.
[217] W. Yang, J. Hao, Z. Zhang, B. Zhang, New Journal of Chemistry, 39 (2015) 8802-8806.
[218] J. Ezzaldeen Younes, B. Ning, D. Shou-Nian, Current Analytical Chemistry, 14 (2018) 49-57.
[219] H.-M. Yang, S.-C. Jang, S.B. Hong, K.-W. Lee, C. Roh, Y.S. Huh, B.-K. Seo, Journal of Alloys and Compounds, 657 (2016) 387-393.
[220] K.-F. Peng, H.-W. Zhao, X.-F. Wu, RSC Advances, 5 (2015) 1812-1817.
[221] J. Peng, M. Dong, B. Ran, W. Li, Y. Hao, Q. Yang, L. Tan, K. Shi, Z. Qian, ACS Applied Materials & Interfaces, 9 (2017) 13875-13886.
[222] A.K. Das, R. Bera, A. Maitra, S.K. Karan, S. Paria, L. Halder, S.K. Si, A. Bera, B.B. Khatua, Journal of Materials Chemistry A, 5 (2017) 22242-22254.
[223] X. Sun, S. Li, R. Liu, X. Sun, X. Liu, A. Li, W. Li, Journal of Nanoparticle Research, 22 (2020) 37.
[224] A.H. Odda, H. Li, N. Kumar, N. Ullah, M.I. Khan, G. Wang, K. Liang, T. Liu, Y.-Y. Pan, A.-W. Xu, Bioconjugate Chemistry, 31 (2020) 1474-1485.
[225] E. Tronc, J.-P. Jolivet, J. Lefebvre, R. Massart, Journal of the Chemical Society, Faraday Transactions 1: Physical Chemistry in Condensed Phases, 80 (1984) 2619-2629.
[226] C. Thammawong, P. Opaprakasit, P. Tangboriboonrat, P. Sreearunothai, Journal of Nanoparticle Research, 15 (2013) 1689.
[227] M. Magro, G. Sinigaglia, L. Nodari, J. Tucek, K. Polakova, Z. Marusak, S. Cardillo, G. Salviulo, U. Russo, R. Stevanato, R. Zboril, F. Vianello, Acta Biomaterialia, 8 (2012) 2068-2076.
[228] M. Magro, A. Faralli, D. Baratella, I. Bertipaglia, S. Giannetti, G. Salviulo, R. Zboril, F. Vianello, Langmuir, 28 (2012) 15392-15401.
[229] M.F. Dumont, H.A. Hoffman, P.R.S. Yoon, L.S. Conklin, S.R. Saha, J. Paglione, R.W. Sze, R. Fernandes, Bioconjugate Chemistry, 25 (2014) 129-137.
[230] J.M. Au - Vojtech, J. Au - Cano-Mejia, M.F. Au - Dumont, R.W. Au - Sze, R. Au - Fernandes, JoVE, (2015) e52621.
[231] X. Li, D. Liu, S. Song, H. Zhang, Crystal Growth & Design, 14 (2014) 5506-5511.
[232] C.L.C. Carvalho, A.T.B. Silva, L.J.A. Macedo, R.A.S. Luz, J.M.M. Neto, U.P.R. Filho, W. Cantanhêde, International Journal of Molecular Sciences, 16 (2015) 14594-14607.
[233] L. Hu, P. Zhang, Q.-w. Chen, J.-y. Mei, N. Yan, RSC Advances, 1 (2011) 1574-1578.
[234] L. Li, P. Zhang, Z. Li, D. Li, B. Han, L. Tu, B. Li, Y. Wang, L. Ren, P. Yang, S. Ke, S. Ye, W. Shi, Nanotechnology, 30 (2019) 325501.
[235] Z. Zhao, S. Xu, Z. Du, C. Jiang, X. Huang, ACS Sustainable Chemistry & Engineering, 7 (2019) 7183-7192.
[236] H. Xu, H. Shang, L. Jin, C. Chen, C. Wang, Y. Du, Journal of Materials Chemistry A, 7 (2019) 26905-26910.
[237] M. Zhou, R. Zhang, M. Huang, W. Lu, S. Song, M.P. Melancon, M. Tian, D. Liang, C. Li, Journal of the American Chemical Society, 132 (2010) 15351-15358.

[238] H. Hu, Bu Y. Guan, Xiong W. Lou, Chem, 1 (2016) 102-113.
[239] Z. Yu, W. Hu, H. Zhao, X. Miao, Y. Guan, W. Cai, Z. Zeng, Q. Fan, T.T.Y. Tan, Angewandte Chemie International Edition, 58 (2019) 8536-8540.
[240] X. Wang, H. Li, F. Li, X. Han, G. Chen, Nanoscale, 11 (2019) 22079-22088.
[241] Y. Liu, Q. Guo, X. Zhu, W. Feng, L. Wang, L. Ma, G. Zhang, J. Zhou, F. Li, Advanced Functional Materials, 26 (2016) 5120-5130.
[242] A.K. Parchur, Q. Li, A. Zhou, Biomaterials Science, 4 (2016) 1781-1791.
[243] Q. Liang, J. Chen, F. Wang, Y. Li, Coordination Chemistry Reviews, 424 (2020) 213488.
[244] T. Wang, E. Lin, Y.-L. Peng, Y. Chen, P. Cheng, Z. Zhang, Coordination Chemistry Reviews, 423 (2020) 213485.
[245] F. Boorboor Ajdari, E. Kowsari, M. Niknam Shahrak, A. Ehsani, Z. Kiaei, H. Torkzaban, M. Ershadi, S. Kholghi Eshkalak, V. Haddadi-Asl, A. Chinnappan, S. Ramakrishna, Coordination Chemistry Reviews, 422 (2020) 213441.
[246] J.-X. Liu, X.-B. Zhang, Y.-L. Li, S.-L. Huang, G.-Y. Yang, Coordination Chemistry Reviews, 414 (2020) 213260.
[247] V. Das, R. Kaushik, F. Hussain, Coordination Chemistry Reviews, 413 (2020) 213271.
[248] A.V. Anyushin, A. Kondinski, T.N. Parac-Vogt, Chemical Society Reviews, 49 (2020) 382-432.
[249] Y. Luo, J. Li, X. Liu, L. Tan, Z. Cui, X. Feng, X. Yang, Y. Liang, Z. Li, S. Zhu, Y. Zheng, K.W.K. Yeung, C. Yang, X. Wang, S. Wu, ACS Central Science, 5 (2019) 1591-1601.
[250] Q. Cheng, Z.-H. Li, Y.-X. Sun, X.-Z. Zhang, NPG Asia Materials, 11 (2019) 63.
[251] Y. Wang, Y. Wang, L. Zhang, C.-S. Liu, H. Pang, Chemistry – An Asian Journal, 14 (2019) 2790-2795.
[252] H. Kang, J.T. Buchman, R.S. Rodriguez, H.L. Ring, J. He, K.C. Bantz, C.L. Haynes, Chemical Reviews, 119 (2019) 664-699.
[253] Q. Yue, J. Sun, Y. Kang, Y. Deng, Angewandte Chemie International Edition, 59 (2020) 15804-15817.
[254] Y. Huang, L. Hu, T. Zhang, H. Zhong, J. Zhou, Z. Liu, H. Wang, Z. Guo, Q. Chen, Scientific Reports, 3 (2013) 2647.
[255] Y.Y. Su, Z. Teng, H. Yao, S.J. Wang, Y. Tian, Y.L. Zhang, W.F. Liu, W. Tian, L.J. Zheng, N. Lu, Q.Q. Ni, X.D. Su, Y.X. Tang, J. Sun, Y. Liu, J. Wu, G.F. Yang, G.M. Lu, L.J. Zhang, ACS Applied Materials & Interfaces, 8 (2016) 17038-17046.
[256] W. Tian, Y. Su, Y. Tian, S. Wang, X. Su, Y. Liu, Y. Zhang, Y. Tang, Q. Ni, W. Liu, M. Dang, C. Wang, J. Zhang, Z. Teng, G. Lu, Advanced Science, 4 (2017) 1600356.
[257] W. Li, Z. Liu, B. Zhao, J. Liu, Langmuir, 36 (2020) 4194-4200.
[258] F. Tian, B. Chi, C. Xu, C. Lin, Z. Xu, A.K. Whittaker, C. Zhang, L. Li, J. Wang, Biomaterials Science, 8 (2020) 6212-6224.
[259] A. Cabrera-García, E. Checa-Chavarria, J. Pacheco-Torres, Á. Bernabeu-Sanz, A. Vidal-Moya, E. Rivero-Buceta, G. Sastre, E. Fernández, P. Botella, Nanoscale, 10 (2018) 6349-6360.
[260] E. Chelebaeva, L. Raehm, J.-O. Durand, Y. Guari, J. Larionova, C. Guérin, A. Trifonov, M. Willinger, K. Thangavel, A. Lascialfari, O. Mongin, Y. Mir, M. Blanchard-Desce, Journal of Materials Chemistry, 20 (2010) 1877-1884.
[261] M. Santha Moorthy, G. Hoang, B. Subramanian, N.Q. Bui, M. Panchanathan, S. Mondal, V.P. Thi Tuong, H. Kim, J. Oh, Journal of Materials Chemistry B, 6 (2018) 5220-5233.
[262] K.J. Stine, Applied Sciences, 9 (2019) 797.
[263] J. Zhai, Y. Zhai, D. Wen, S. Dong, Electroanalysis, 21 (2009) 2207-2212.
[264] S. Chen, L. Ma, R. Yuan, Y. Chai, Y. Xiang, C. Wang, European Food Research and Technology, 232 (2011) 87-95.
[265] M. Skunik-Nuckowska, P. Bacal, P.J. Kulesza, Journal of Solid State Electrochemistry, 19 (2015) 2753-2762.
[266] Y. You, H.-R. Yao, S. Xin, Y.-X. Yin, T.-T. Zuo, C.-P. Yang, Y.-G. Guo, Y. Cui, L.-J. Wan, J.B. Goodenough, Advanced Materials, 28 (2016) 7243-7248.
[267] Y. Zheng, J. Qiao, J. Yuan, J. Shen, A.-j. Wang, L. Niu, Electrochimica Acta, 257 (2017) 172-180.

[268] F. Song, D. Huo, J. Hu, H. Huang, J. Yuan, J. Shen, A.-J. Wang, Nanotechnology, 30 (2019) 505401.
[269] P. Chaturbedy, S. Chatterjee, R.B. Selvi, A. Bhat, M.K. Kavitha, V. Tiwari, A.B. Patel, T.K. Kundu, T.K. Maji, M. Eswaramoothy, Journal of Materials Chemistry B, 1 (2013) 939-945.
[270] L. Wang, S. Tricard, P. Yue, J. Zhao, J. Fang, W. Shen, Biosensors and Bioelectronics, 77 (2016) 1112-1118.
[271] X. Peng, R. Wang, T. Wang, W. Yang, H. Wang, W. Gu, L. Ye, ACS Applied Materials & Interfaces, 10 (2018) 1084-1092.
[272] N. Gong, H. Wang, S. Li, Y. Deng, X.a. Chen, L. Ye, W. Gu, Langmuir, 30 (2014) 10933-10939.
[273] P.J. Kulesza, B. Grzybowska, M.A. Malik, M. Chojak, K. Miecznikowski, Journal of Electroanalytical Chemistry, 512 (2001) 110-118.
[274] P.J. Kulesza, M. Bandoch, Journal of Electroanalytical Chemistry, 323 (1992) 131-147.
[275] Y. Wang, Q. Chen, ACS Applied Materials & Interfaces, 6 (2014) 6196-6201.
[276] C. Wei, R.R. Rao, J. Peng, B. Huang, I.E.L. Stephens, M. Risch, Z.J. Xu, Y. Shao-Horn, Advanced Materials, 31 (2019) 1806296.
[277] D. Zhao, Y. Lu, D. Ma, Molecules, 25 (2020) 2304.
[278] Y. Sui, X. Ji, Chemical Reviews, 121 (2021) 6654-6695.
[279] C. Xuan, J. Zhang, J. Wang, D. Wang, Chemistry – An Asian Journal, 15 (2020) 958-972.
[280] L.-M. Cao, D. Lu, D.-C. Zhong, T.-B. Lu, Coordination Chemistry Reviews, 407 (2020) 213156.
[281] R. Sanchis-Gual, T.F. Otero, M. Coronado-Puchau, E. Coronado, Nanoscale, 13 (2021) 12676-12686.
[282] M. Morant-Giner, R. Sanchis-Gual, J. Romero, A. Alberola, L. García-Cruz, S. Agouram, M. Galbiati, N.M. Padial, J.C. Waerenborgh, C. Martí-Gastaldo, S. Tatay, A. Forment-Aliaga, E. Coronado, Advanced Functional Materials, 28 (2018) 1706125.
[283] Y. Jiang, S. Yu, B. Wang, Y. Li, W. Sun, Y. Lu, M. Yan, B. Song, S. Dou, Advanced Functional Materials, 26 (2016) 5315-5321.
[284] Y. Liu, D. He, Y. Cheng, L. Li, Z. Lu, R. Liang, Y. Fan, Y. Qiao, S. Chou, Small, 16 (2020) 1906946.
[285] D.R. Thévenot, K. Toth, R.A. Durst, G.S. Wilson, Biosensors and Bioelectronics, 16 (2001) 121-131.
[286] F. Di Pietrantonio, D. Cannatà, M. Benetti, Chapter 8 - Biosensor technologies based on nanomaterials, in: V. Dinca, M.P. Suchea (Eds.) Functional Nanostructured Interfaces for Environmental and Biomedical Applications, Elsevier, 2019, pp. 181-242.
[287] T. Xu, H. Zhang, X. Li, Z. Xie, X. Li, Biosensors and Bioelectronics, 73 (2015) 167-173.
[288] T.-S. Xu, Biochemical Engineering Journal, 105 (2016) 36-43.
[289] L. Cui, J. Hu, C.-c. Li, C.-m. Wang, C.-y. Zhang, Biosensors and Bioelectronics, 122 (2018) 168-174.
[290] Y. Wang, Y. Li, H. Ma, A. Guo, B. Du, T. Yan, Q. Wei, Analyst, 140 (2015) 3557-3564.
[291] Y. Wang, Y. Wang, X. Pang, B. Du, H. Li, D. Wu, Q. Wei, Sensors and Actuators B: Chemical, 214 (2015) 124-131.
[292] D. Zhou, K. Zeng, M. Yang, Microchimica Acta, 186 (2019) 121.
[293] D. Kim, K. Shin, S.G. Kwon, T. Hyeon, Advanced Materials, 30 (2018) 1802309.
[294] C. Fang, M. Zhang, Journal of Controlled Release, 146 (2010) 2-5.
[295] F. Pene, E. Courtine, A. Cariou, J.P. Mira, Critical care medicine, 37 (2009) S50-58.
[296] V.F. Cardoso, A. Francesko, C. Ribeiro, M. Bañobre-López, P. Martins, S. Lanceros-Mendez, Advanced Healthcare Materials, 7 (2018) 1700845.
[297] X. Cai, W. Gao, L. Zhang, M. Ma, T. Liu, W. Du, Y. Zheng, H. Chen, J. Shi, ACS Nano, 10 (2016) 11115-11126.
[298] G. Fu, W. Liu, S. Feng, X. Yue, Chemical Communications, 48 (2012) 11567-11569.
[299] B. Yu, C. Wang, ChemistrySelect, 5 (2020) 10841-10847.
[300] C. Ren, Y. Cheng, W. Li, P. Liu, L. Yang, Q. Lu, M. Xu, F. Tan, J. Li, N. Li, Biomaterials Science, 8 (2020) 1981-1995.
[301] G. Chen, H. Qiu, P.N. Prasad, X. Chen, Chemical Reviews, 114 (2014) 5161-5214.

[302] C. Tassa, S.Y. Shaw, R. Weissleder, Accounts of Chemical Research, 44 (2011) 842-852.
[303] D. Yoo, J.-H. Lee, T.-H. Shin, J. Cheon, Accounts of Chemical Research, 44 (2011) 863-874.
[304] D. Ho, X. Sun, S. Sun, Accounts of Chemical Research, 44 (2011) 875-882.
[305] J. Xie, G. Liu, H.S. Eden, H. Ai, X. Chen, Accounts of Chemical Research, 44 (2011) 883-892.
[306] J.E. Lee, N. Lee, T. Kim, J. Kim, T. Hyeon, Accounts of Chemical Research, 44 (2011) 893-902.
[307] M.P. Melancon, M. Zhou, C. Li, Accounts of Chemical Research, 44 (2011) 947-956.
[308] D.-E. Lee, H. Koo, I.-C. Sun, J.H. Ryu, K. Kim, I.C. Kwon, Chemical Society Reviews, 41 (2012) 2656-2672.
[309] M. Rohrer, H. Bauer, J. Mintorovitch, M. Requardt, H.-J. Weinmann, Investigative Radiology, 40 (2005) 715-724.
[310] J. Zeng, D. Goldfeld, Y. Xia, Angewandte Chemie International Edition, 52 (2013) 4169-4173.
[311] H. Kobayashi, Y. Koyama, T. Barrett, Y. Hama, C.A.S. Regino, I.S. Shin, B.-S. Jang, N. Le, C.H. Paik, P.L. Choyke, Y. Urano, ACS Nano, 1 (2007) 258-264.
[312] P.A. Jarzyna, A. Gianella, T. Skajaa, G. Knudsen, L.H. Deddens, D.P. Cormode, Z.A. Fayad, W.J.M. Mulder, WIREs Nanomedicine and Nanobiotechnology, 2 (2010) 138-150.
[313] C. Delchet, A. Tokarev, X. Dumail, G. Toquer, Y. Barré, Y. Guari, C. Guerin, J. Larionova, A. Grandjean, RSC Advances, 2 (2012) 5707-5716.
[314] W. Liu, P. Duan, H. Xiong, H. Su, X. Zhang, J. Wang, F. Yang, Z. Zou, Journal of Materials Chemistry C, 9 (2021) 5505-5514.
[315] W. Liu, J. Liu, Z. Yang, G. Ji, ACS Applied Materials & Interfaces, 10 (2018) 28887-28897.
[316] X. Zeng, B. Yang, L. Zhu, H. Yang, R. Yu, RSC Advances, 6 (2016) 105644-105652.
[317] R. Qiang, Y. Du, H. Zhao, Y. Wang, C. Tian, Z. Li, X. Han, P. Xu, Journal of Materials Chemistry A, 3 (2015) 13426-13434.
[318] Y. Li, Y. Duan, X. Kang, Journal of Materials Chemistry C, 9 (2021) 6316-6323.

List of figures

core@shell@shell nanoparticles. Insert: Magnification of the TEM image showing one nanoparticle; e) STEM-HAADF image of Au@KNi[$Fe^{II}(CN)_6$]@KNi[$Cr^{III}(CN)_6$] core@shell@shell with the EDS mapping showing the gold (red), the nickel (light blue), and the iron (dark blue) and the chromium (green) atoms. Adapted from Ref. [165, 166] with permission from John Wiley and Sons.

Figure 8. a) Schematic illustration of the Au@PB core@shell nanoparticle synthesis; b) TEM image of the Au@PB core@shell nanoparticles; c) HAADF-STEM images of Au@PB nanoparticles and EDX elemental mapping of Au core (blue), PB shell (yellow), and the merged image; d) UV−vis spectra of Au NPs (black), Au@CN NPs (red), PB NPs (blue), and Au@PB NPs (purple) showing the change in the SPR band with PB coating; e) The Raman spectra of Au@PB nanoparticles and HepG2 cells. Reprinted with permission from Y. Yin, Q. Li, S. Ma, H. Liu, B. Dong, J. Yang, D. Liu, Analytical Chemistry, 89 (2017) 1551-1557. Copyright 2021 American Chemical Society. [164]

Figure 9. TEM images of Au NSs (A); Au@Ag NCs (B); Au@PB NCs (C); inset of (B): HAADF-STEM image of Au@Ag NCs; inset of (C): high-magnification TEM image of Au@PB NCs. (D−H) Mapping image of Au@PB NCs. Adapted with permission from L. Hang, H. Li, T. Zhang, D. Men, C. Zhang, P. Gao, Q. Zhang, ACS Applied Materials & Interfaces, 11 (2019) 39493-39502. Copyright 2021 American Chemical Society. [189]

Figure 10. TEM images of $Co_3[Fe(CN)_6]$@Pd nanoheterostructures showing: a) the cubic PBA core and Pd satellites most likely situated in the surface porosity of the PBA, the atomic distribution for b) Pd, c) Co, and d) N; and e), f) TEM images PB@FePt nanoheterostructure showing the PB cubic core and the FePt satellite nanoparticles. Reproduced from Ref. [194] [203] with permission from the Royal Society of Chemistry.

Figure 11. TEM images of $Ni^{II}Cr^{III}$-PBA@Au core@satellites nanoheterostructures with spherical (a), nano-rods (c) and nanostars (e) Au satellites and their corresponding electronic spectra showing the plasmon band. Reproduced from Ref. [199] with permission from the Royal Society of Chemistry.

Figure 12. SEM images of: A) PB nanoparticles, inset: the corresponding TEM image of a single PB nanoparticle; B) PB@PAA Janus nanoparticles, inset: the corresponding TEM image of a single PB@PAA Janus nanoparticles; C) PB@PAA/Au Janus nanoparticles. D) TEM image of a single PB@PAA/Au Janus nanoparticles. E) Magnified HR-TEM image of the dashed boxmarked area of PAA/Au. F) Magnified HR-TEM image of the dashed box-marked area of small Au nanoparticles. Adapted from Ref. [204] with permission from John Wiley and Sons.

Figure 13. Schematic representation of two-step design of C_{60}@PBA/Au nanoheterostructures and their post-synthetic functionalization with alkaline phosphatase (AP) for further detection of aptamers (APT II). Adapted from Ref. [202] with permission from Elsevier.

Figure 14. (a) TEM image of the Fe_3O_4@PB nanoheterostructures; b) Fe_3O_4@PB nanoparticles. Adapted with permission from G. Fu, W. Liu, Y. Li, Y. Jin, L. Jiang, X. Liang, S. Feng, Z. Dai, Bioconjugate Chemistry, 25 (2014) 1655-1663. Copyright 2021 American Chemical Society. [209] Reproduced from Ref.[214] with permission from the Royal Society of Chemistry.

Figure 15. TEM images of multicore Fe_3O_4@PB shell/satellites nanoheterostructures prepared by the polyol method following the single source cyanoferrate precursor strategy from

$K_4[Fe(CN)_6]$ with TEM images for sizes of a) 293.8 ± 7.7 nm, b) 331.7 ± 3.9 nm, and c) 429.5 ± 17.1 nmm. Reprinted from Ref.[219] with permission from Elsevier.

Figure 16. TEM images of nanoheterostructures: a) PB@Co_3O_4, (b) PB@MnO_2; SEM images of c) PB@Co_3O_4, d) PB@MnO_2. Reproduced from Ref. [217] [222] with permission from the Royal Society of Chemistry.

Figure 17. TEM images of (a), (b) PB@MoS_2 and (c), (d) CoS_2@PB. The insets are the HR-TEM images. Adapted with permission from L. Li, P. Zhang, Z. Li, D. Li, B. Han, L. Tu, B. Li, Y. Wang, L. Ren, P. Yang, S. Ke, S. Ye, W. Shi, Nanotechnology, 30 (2019) 325501. [235] Copyright 2021 American Chemical Society. Reproduced from Ref. [236] with permission from the Royal Society of Chemistry.

Figure 18. TEM images of a) the $NaNdF_4$ nanoparticles, b) $NaNdF_4$@PB core@shell nanostructures and c) HRTEM image of $NaNdF_4$@PB core@shell nanostructures. Adapted from Ref. [239] with permission from John Wiley and Sons.

Figure 19. Schematic illustration of the PB@UIO66-TCPP MOF core@shell nano-objects (a); TEM pictures of the pristine PB nanoparticles (b) and PB@UIO66-TCPP MOF core@shell nano-objects (c), scale bar = 50 nm; TEM-EDX of PB@UIO66-TCPP MOF core@shell nano-objects (d); EDX elemental mapping images of PB@UIO66-TCPP MOF core@shell nano-objects (e). Reprinted with permission from Y. Luo, J. Li, X. Liu, L. Tan, Z. Cui, X. Feng, X. Yang, Y. Liang, Z. Li, S. Zhu, Y. Zheng, K.W.K. Yeung, C. Yang, X. Wang, S. Wu, ACS Central Science, 5 (2019) 1591-1601. Copyright 2021 American Chemical Society. [249]

Figure 20. SEM images of pristine $Mn_3[Fe(CN)_6]_2$ PBA (a) and related $Mn_3[Fe(CN)_6]_2$@POM hollow cubes (b); (c) TEM image and (d) elemental mappings of $Mn_3[Fe(CN)_6]_2$@POM prooving the homogeneous distribution of the different elements in the nanoparticles. Reproduced from Ref. [236] with permission from the Royal Society of Chemistry.

Figure 21. Main morphologies of PB(A)s@Silica nanoheterostructures and their advantages.

Figure 22. Four synthetic approaches used for the synthesis of PB(A)s core@silica shell nano-objects.

Figure 23. TEM images for: PB core@PMO silica shell nanocubes (A); $Gd[Fe(CN)_6].4H_2O$@SiO_2 shell nanorods (B); PB core@SiO_2/EuW_{10} shell (C) PB core@SiO_2 shell (D); SiO_2 core@$Ni_3[Fe(CN)_6]_2$ satellite nano-rices (E), porous PB core@ dendritic SiO_2 shell (F). Reproduced from Ref. [258] [259] [260] [261] with permission from the Royal Society of Chemistry. Reprinted with permission from W. Li, Z. Liu, B. Zhao, J. Liu, Langmuir, 36 (2020) 4194-4200. Copyright 2021 American Chemical Society. [257]

Figure 24. a–c) SEM, d–e) TEM images of the MWCNT@PB nanoheterostructures. f) Schematic illustration showing the mixed conducting necklace like network. Reprinted from Ref. [266] with permission from John Wiley and Sons.

Figure 25. a) Schematic of a two-electrode fuel cell or water electrolyser. b) Schematic representation of a three-electrode electrochemical cell with working electrode, reference electrode, counter electrode, and gas inlet.

Figure 26. Schematic diagram of HER at the active interface of ultrafine Pt and a $Ni_3[Fe(CN)_6]_2$ nanocube, including the Volmer step of water dissociation on the Ni^{2+} species and the formation of Pt–H_{ad} intermediates at the boundary between the Ni and Pt domains, the Heyrovsky reaction of Pt–H_{ad} with another water molecule, as well as the Tafel recombination reaction of two H_{ad} atoms.

Figure 27. Schematic illustration of enzyme-triggered tyramine-HRP repeats on PB@Au nanostructures for highly sensitive electrochemical immunoassay of tissue polypeptide antigen (TPA) on mAb1-functionalized screen-printed carbon electrode with a sandwich-type detection mode. Reproduced from Ref.[287] with permission from Elsevier.

Figure 28. Schematic drawing of the immunosensor fabrication process. (a) Dropping of chitosan–nanoAu hydrogel membrane; (b) immobilizing of anti-CEA; (c) the immunoreaction of CEA and anti-CEA; (d) incubation of the solution containing multi-labelled Fe_3O_4@PB@Au composite magnetic conjugate resulting in an amplified signal-generating detection; (e) separation of the immunocomplex using an external magnetic field permits the regeneration of the immunosensor. Reproduced from Ref. [207] with permission from Elsevier.

Figure 29. Schematic illustration of the preparation of γ-Fe_2O_3@PB and immunoassays based on γ-Fe_2O_3@PB conjugated with SPA. Reproduced from Ref.[215] with permission from the Royal Society of Chemistry.

Figure 30. Simplified diagrams of: a) the radiative and nonradiative processes in a single Nd^{3+} ion; b) the cross-relaxation between Nd^{3+} ions in the $NaNdF_4$ core; c) the generation of new cross-relaxation pathways (CR2) between Nd^{3+} ions in the $NaNdF_4$ core and the PB shell.

Figure 31. (a) Monitoring the tumour treatment outcome through NIR (window II) imaging, which was recorded at 0, 7, and 14 days post photothermal treatment. (b and d) The average tumour volume and weight in three groups of BALB/c mice, including two control groups (intratumorally injected with saline or a $NaErF_4$@$NaYF_4$@$NaNdF_4$@PB encapsulated in a phospholipid PEG micelle (PEG-CSS) and the PTT-treated group (both with the $NaErF_4$@$NaYF_4$@$NaNdF_4$@PB nano-objects and 808 nm laser irradiation). All of the PTT treatment groups utilized an 808 nm light dose of 1 Wcm^{-2} for 10 min. Reproduced from Ref.[240] with permission from the Royal Society of Chemistry.

Figure 32. Schematic representation of the complex multifunctional Au@PB@Cu_2O@BPQDs nanoheterostructures showing multimodal imageries and PTT/PDT enhanced therapeutic effect involving PIRET phenomenon (BPQD = black phosphorus quantum dots).

Figure 33. Schematic representation of the proposed photocatalytic mechanism of heterojunction photocatalysts in the PB@UIO-66-TCCP nanoheterostructures.

Figure 34. Thermographic images of mice 12h post *i.v.* injection of saline Fe_3O_4@PB functionalized with PDA and PDA/AlPc/BSA under a 660 nm laser (1 $W.cm^{-2}$) irradiation during 5 min. (PDA= polydopamine, AlPc = aluminum phthalocyanine). Reproduced from Ref.[214] with permission from the Royal Society of Chemistry.

List of schemes

List of tables